Study of materials interactions and electrochemical mechanisms at the interfaces of electrodes of a memory stack based on metal oxides

Aurélie Marty

To cite this version:

Aurélie Marty. Study of materials interactions and electrochemical mechanisms at the interfaces of electrodes of a memory stack based on metal oxides. Micro and nanotechnologies/Microelectronics. Université Grenoble Alpes, 2018. English. NNT : 2018GREAT038 . tel-01891068

HAL Id: tel-01891068
https://theses.hal.science/tel-01891068
Submitted on 9 Oct 2018

Communauté
UNIVERSITÉ Grenoble Alpes

THÈSE

Pour obtenir le grade de

DOCTEUR DE LA COMMUNAUTE UNIVERSITE GRENOBLE ALPES

Spécialité : NANO ELECTRONIQUE ET NANO TECHNOLOGIES

Arrêté ministériel : 25 mai 2016

Présentée par

Aurélie MARTY

Thèse dirigée par **Patrice GONON**, Maître de Conférences, UGA

préparée au sein du **Laboratoire des Technologies de la Microélectronique**
dans **l'École Doctorale Electronique, Electrotechnique, Automatique, Traitement du Signal (EEATS)**

Etude des interactions matériaux et des mécanismes électrochimiques aux interfaces des électrodes d'un empilement mémoire à base d'oxydes métalliques

Thèse soutenue publiquement le **: 30 mai 2018**
devant le jury composé de :

Marie-Paule Besland
IMN Université de Nantes, Rapporteur
Abdelkader Souifi
INL INSA Lyon, Rapporteur
Elisabeth Blanquet
SIMAP Université Grenoble Alpes, Président
Patrice Gonon
LTM Université Grenoble Alpes, Directeur de thèse
Rémy Gassilloud
CEA Leti, Grenoble, Co-encadrant, Invité
Christophe Vallée
LTM Université Grenoble Alpes, Co-encadrant, Invité

Remerciements

Je tiens avant tout à remercier mon directeur de thèse Patrice Gonon, ainsi que mes encadrants, Rémy Gassilloud et Christophe Vallée. Merci de m'avoir donné l'opportunité de réaliser ce travail de thèse et merci beaucoup pour votre disponibilité et vos précieux conseils. Travailler à vos côtés a été particulièrement enrichissant et épanouissant.

J'aimerai également remercier Madame Marie-Paule Besland et Monsieur Abdelkader Souifi pour avoir accepté de lire cette thèse et d'en être les rapporteurs. Je tiens également à remercier Madame Elisabeth Blanquet pour avoir tenu à la fois le rôle de présidente du jury et d'examinatrice.

Je remercie également Thierry Baron, directeur du LTM et Laurent Vendroux, directeur du SDEP au CEA, pour m'avoir accueilli dans leurs laboratoires respectifs. Je voudrais aussi remercier l'équipe de la BM25 de l'ESRF, et plus particulièrement Germán R. Castro et Juan Rubio-Zuazo qui nous ont permis d'accéder à leur beamline afin d'effectuer les analyses d'HAXPES.

De plus, ce travail n'aurait pas été aussi enrichissant sans le concours de nombreuses personnes. Il m'est difficile de citer tout le monde, mais je tiens à tous vous remercier pour votre temps et votre expertise. Je tiens à remercier plus particulièrement Eugénie Martinez, Bernard Pelissier, Marc Veillerot, Mathieu Bernard et Gabriel Molas. Merci à vous pour votre investissement dans mes recherches et pour les discussions très intéressantes que nous avons pu avoir et qui m'ont permis de faire avancer ma réflexion.

Enfin, je souhaiterai remercier mon mari pour son soutien indéfectible même si je l'ai quelque peu délaissé durant ces années de thèse, mes parents sans qui je ne serais pas là et qui n'ont jamais cessé de m'encourager et mes frères pour leur optimisme sans faille et leur bonne humeur.

Table of contents

Chapter 1: Introduction

1.1. Context

Nowadays, microelectronics devices are more and more numerous and the need in retaining information increases drastically, since they become increasingly connected in networks, in particular through the internet. Non-volatile memories are a memory class whose data are kept when the electrical power is turned off. They are used in devices such as USB keys, solid state hard drives, servers,… and are based on the Flash concept. The Flash memory has become a standard due to its inherent compatibility with the silicon technology and has consequently followed the device size shrinkage. However, it approaches the limit of downscaling and is no longer able to maintain Moore's law. This law is the affirmation that the number of transistors in integrated circuits double approximately every two years. These observations were first made by Gordon Moore in 1965 and the predicted tendency has become the roadmap to follow. As Flash memories are no longer able to maintain Moore's law, other non-volatile memory types should be proposed.

1.2. Non-volatile memories currently used and their limitations

The principle of Flash memories is to store electrons in a floating gate of a silicon transistor thanks to the tunnel effect [1]. As seen in Figure 1 a), a transistor is composed of a source and a drain separated by a substrate, and a gate separated from the rest of the structure by a dielectric layer. In Figure 1 b) the electrical schematic of a Flash memory is presented. We can see that the device is composed of a drain and a source as in a standard transistor, but it has two gates separated by an oxide layer, approximated here by capacitor. The first gate can trap charges and is called the floating gate and the second corresponds to the control gate.

When applying a voltage between the source and the drain, current flows between the two electrodes. If a positive potential is also applied on the control gate, some of the electrons flow in the floating gate by diffusion through the gate oxide thanks to the tunnel effect. These electrons are thus stored in the floating gate: it represents the 0 bit logical state. To store the 1 bit, a reversed potential is applied on the control gate, which allows trapped charges to return into the channel.

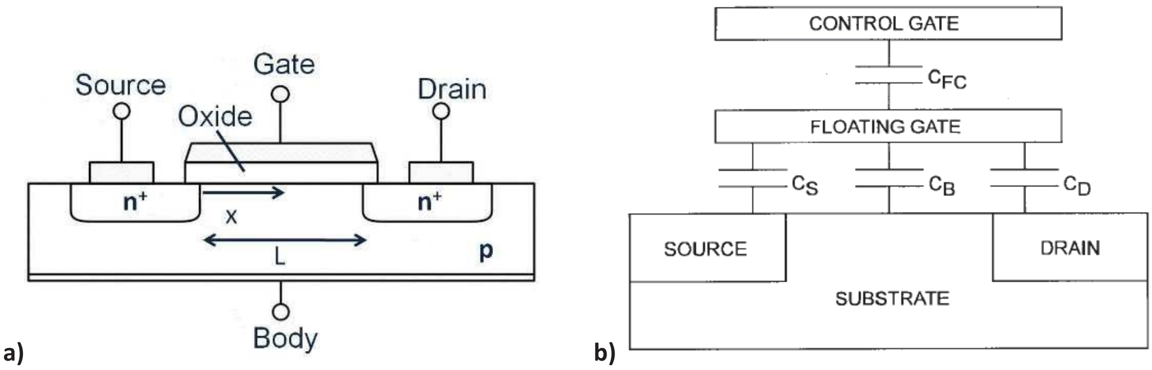

Figure 1: a) Schematic transistor structure ; b) Schematic Flash memory structure [1]

To retain charges in the floating gate, the oxide thickness between the substrate and the floating gate is of first importance. It must be relatively thick enough in order to prevent unwanted leakages under zero potential [2]. If current leaks take place without electrical field, the electrons stored in the floating gate will move back into the substrate and thus the information cannot be retained. This is one of the major reason why Flash memories currently approach their physical downscaling limit. Several ways are currently followed to improve the integration density. In particular, new types of non-volatile memories are studied to replace the Flash memories and extend the limits of downscaling, which is the subject we are interesting in this work.

1.3. New non-volatile memories concepts

Plenty of new memories concepts are currently studied; they are based on several physical principles to store information, using magnetism, electrostatics, crystallography transition, chemical diffusion etc… We propose here to briefly introduce the most advanced concepts, such as first the ferroelectric random access memory or FeRAM, which is based on ferro-electricity [3]. Ferro-electric materials shows a spontaneous electrical polarization. This polarization can be reversed by applying an electrical field E as presented in Figure 2, where the evolution of the polarization according to the electrical field applied is presented. The memory states are based on these two different polarization states obtained by varying the electrical field.

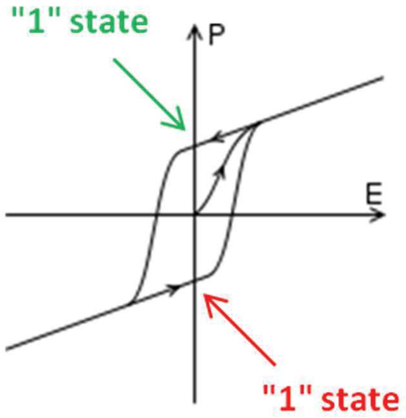

Figure 2: Typical electrical polarization-electrical field hysteresis curve for a ferroelectric material

Another non-volatile memory type is the magnetic random access memory or MRAM [4], which is based on the properties of tunnel magnetoresistance. This effect appears in a stack of two ferromagnetic layers separated by a thin dielectric. One of the ferromagnetic layers is a permanent magnet, whereas the other one has a magnetization which can be modified by applying a magnetic field. When the two ferromagnets have their magnetic moments with parallel orientation (see Figure 3, left stack), a tunnel effect can take place and thus current can pass through the dielectric. Therefore, the memory stack is in a low resistance state. When the moments have antiparallel orientation (Figure 3, right stack) the tunnel effect does not appear and the memory stack is in a high resistance state.

Figure 3: The two states of MRAM stack: left the low resistive state and right the high resisitive state [4]

Phase change random access memory or PCRAM is another concept of non-volatile memories. They are based on the crystalline properties of phase-change materials [5]. Indeed, when heating a phase change material at a temperature slightly above its crystallization temperature, the material passes from an amorphous phase to a crystalline phase. To get back to the amorphous state a temperature pulse must be applied, at a temperature higher than the melting temperature of the material. The two crystalline states imply different resistivity: crystalline phase implies a low resistivity and amorphous phase implies a high resistivity. In PCRAM cells the temperature can be modified by a heater, as presented in Figure 4. This picture is a schematic cross-section of a PCRAM cell, where we can see that the phase change material and an insulator layer containing the heater are stacked between two electrodes.

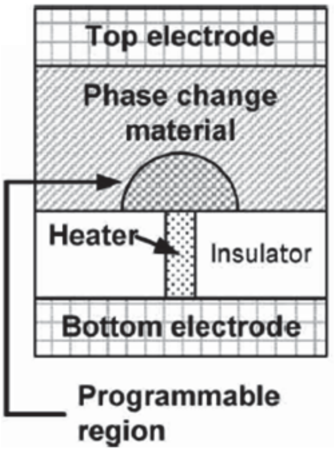

Figure 4: Schematic cross-section of a PCRAM cell [6]

Finally, we introduce the resistive random access memories ReRAM, based on the resistivity change of a dielectric. Their principles are detailed in the next paragraph.

1.4. Memories studied in this thesis: ReRAM

1.4.1. Electrical switching description

Resistive memories are basically composed of a MIM stack, with two conductive electrodes (M) separated by an insulator (I). Two types of ReRAM must be noticed here: the Conductive Bridge Random Access memories (CBRAM), also called ElectroChemical Metallization Memories (ECM), that are expected to be based on the formation and dissolution of a metallic conductive filament and the second type, the Oxygen-based Random Access Memories (OXRAM), which can be explained by the movements of oxygen atoms and subsequent vacancies formation.

To write and erase a ReRAM memory a suitable voltage is applied on the electrodes, which consequently splits the stack resistivity into a high resistive state, called HRS, and a low resistive state, called LRS ([7]-[10]). These two resistive states represent the logical 0 or 1 bits and can be read using a low voltage to insure no modifications of the resistive states. Written or erased states are visible in Figure 5, in a typical current-voltage curve of a resistive memory [8]. In this example, the memory cell is at rest in the HRS state. Then voltage is increased progressively. At a certain voltage value the current increases suddenly: it corresponds to the set. The memory is thus written and has switch to the LRS. The current is limited to the compliance current purposely fixed to prevent the memory from irreversible breakdown. When reversing the voltage the current drops suddenly, which corresponds to the reset. The memory is back in the HRS state, it has been erased.

In Figure 5 the reset requires an opposite polarity that the one required for the set, thus this memory is considered as bipolar. However, some memory cells can switch on the same polarity direction, but at a different voltage levels. In that case, such memories are considered as unipolar. Finally, when the switching can be performed either in negative or positive direction, the memory is considered as nonpolar ([7]-[10]).

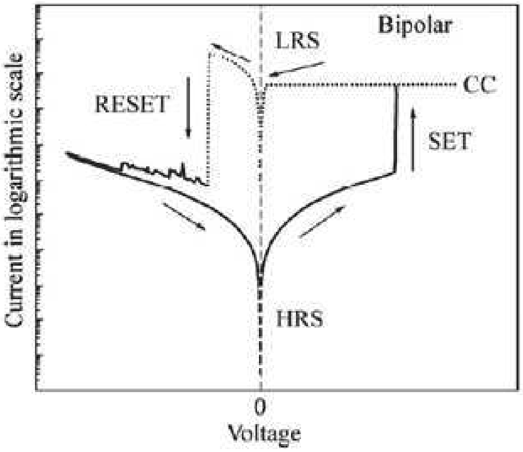

Figure 5: Typical current-voltage curve of bipolar memory [8]

In literature, the fundamental understanding of the switching mechanisms thanks to physical modeling and simulations has been suggested. The main accepted model is based on the growth or dissolution of a conductive filament formed in an oxide between two electrodes [11]. More precisely, it could rely on the size of a constriction area in a conductive path which evolves under the applied field. As presented in Figure 6 a), in the low resistive state the conductive filament shows a diameter which is not constant along its length. The thinnest part is considered as the constriction and has an area named S_C, whereas the largest part area, at the electrode, is called S_0. As observed in b), during the reset the area of the constriction in the filament is reduced, thanks to electro-migration force and Joule heating. Inversely, when reversing the potential during the set, the constriction area increases through potential assisted diffusion (c). In ReRAM, the filament is supposed to be either composed of vacancies in the case of OxRAM or metallic atoms such as copper in CBRAM. Even if this model seems simple, it has been successfully used to explain the I-V characteristics in Figure 5, but movements of atoms (which are largely supposed and accepted) are still ununderstood. In particular, in addition to simulations people tried also to directly see the filament formation and disruption under in-operando transmission electronic microscopy experiments [12]. However, such experiments are complexes, far away from real device operation and generally very difficult to achieve due to the filament nanoscale size which render its localization very difficult. Moreover, the filament assumption is still largely under debate.

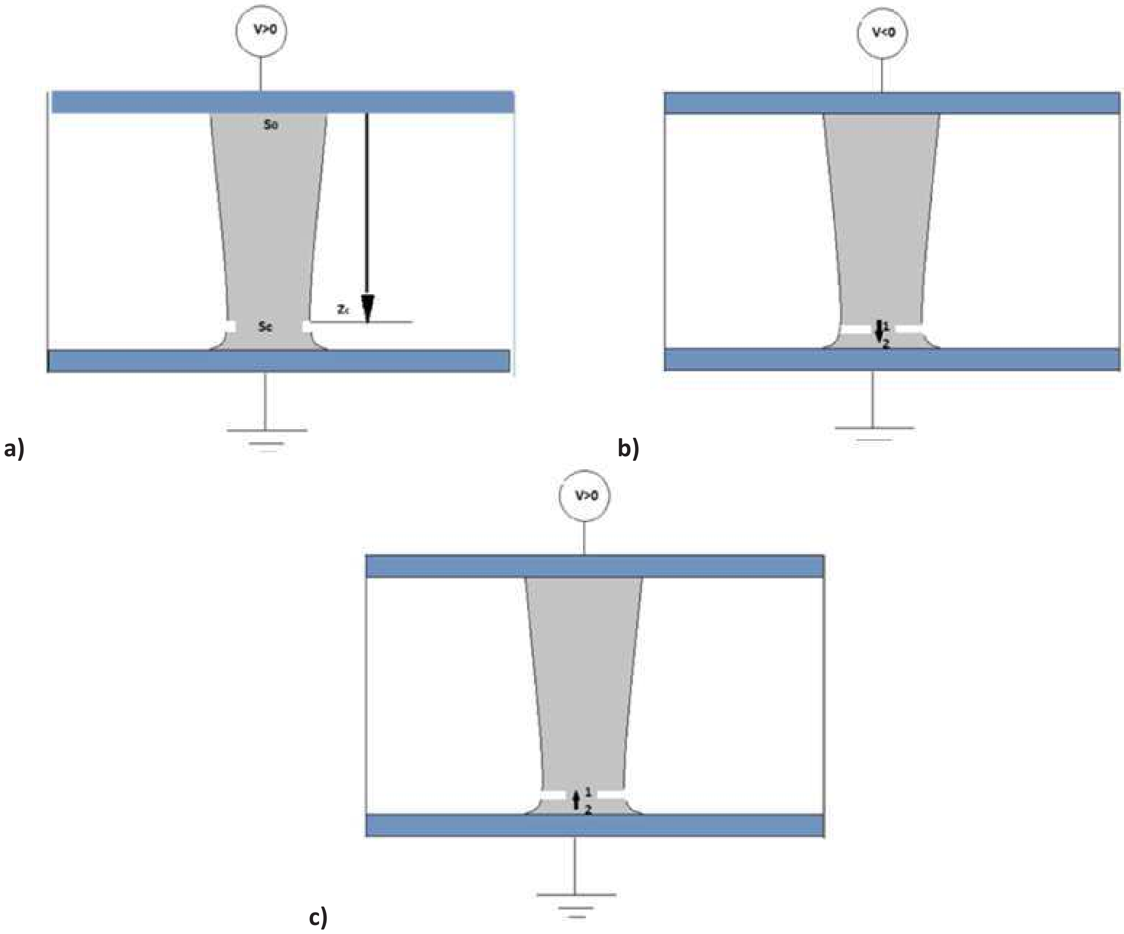

Figure 6:Filament schematic description according to [11] with a) the LRS, b) the reset and c) the set.

To make it more complicated, it is important to notice that for some RRAM stacks the first filament formation requires a higher voltage than during write and erase cycles. This first formation is called forming or electro-forming, whereas the other filament formations are called sets. Such situation is illustrated in Figure 7, where the current-voltage curve of a Cu/SiO_2/Pt CBRAM stack is displayed [10]. When applying for the first time an electrical voltage to the memory stack, thus during the forming cycle represented by the blue line in the graph, the current shows a sudden increase around 4V (the voltage called $V_{SET,form}$), and reaches 10nA, which corresponds to the applied compliance. This increase is believed to correspond to the formation of the first filament. Then, after the reset (below -0.5V) a second cycle is performed (subsequent cycle, in red line). An increase of the current, corresponding to a second filament formation, takes place at a lower potential at around 1.5V (V_{SET}). Therefore, as $V_{SET, form}$ is higher than V_{SET}, the forming step requires a higher voltage than the next cycles. Forming mechanisms are currently very few studied, probably because of their transient nature.

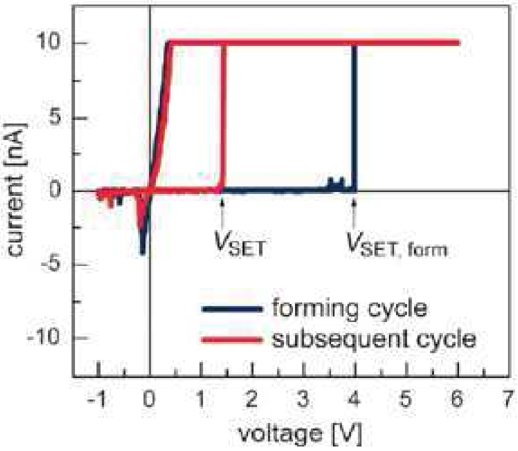

Figure 7: Typical current-voltage curve of a RRAM requiring a forming cycle [10]

1.4.2. Switching mechanisms: focus on CBRAM

Different mechanisms for the resistivity switching are suggested in literature. They seem to be divided in two categories: electrochemical mechanisms and solid state mechanisms (based on physics mainly electrostatic) ([7]-[8]). On one hand, the electrochemical mechanisms are linked to formation of a conductive filament due to half oxidation/reduction reactions and subsequent ionic diffusion ([7]-[8]). On the other hand, the solid state "bulk" and interfaces phenomena regroups several electronic mechanisms such as space-charge-limited conduction, trap charging and discharging, Schottky Emission and Poole-Frenkel emission ([7]-[8]).

In this thesis, the studied memories are mainly CBRAM. In order to simplify our study, we assume that the switching mechanisms are induced mainly by electrochemical phenomena. However, it is important to keep in mind that this assumption neglects the solid state mechanisms and thus gives a restricted point of view on the memory operation. In this work the CBRAM will be compared to an electrochemical cell. The stack corresponds to an asymmetrical M1/I/M2 stack ([13], [14]) as presented in Figure 8. The M1 metal layer plays the role of an active electrode, which means that M1 can be easily electrochemically dissolved in the dielectric. This layer corresponds to the anode and is also called ion source layer. The M2 layer corresponds to the counter electrode, or cathode or bottom electrode, and must be essentially electrochemically inert. Finally, the dielectric which separates the two electrodes could be compared to a "solid electrolyte" in an electrochemical cell.

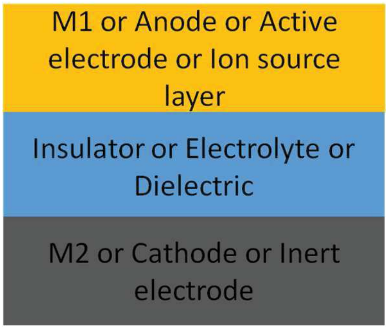

Figure 8: Schematic MIM stack

The forming and dissolution of the filament in CBRAM cells are described in Figure 9. The memory stack is composed of four layers: the ion source layer, the solid electrolyte and the bottom or inert electrode as described previously, and the top electrode. This last layer, as it will be explained in 1.4.3, protects the ion source layer from oxidation and must be as inert as possible regarding the switching mechanisms, as for the bottom electrode.

In Figure 9 a) the electro-forming is sketched. When applying the potential, the active metal M is first oxidized ([8], [13] and [14]). Thus, the reaction (1) takes place at the active electrode:

$$M \rightarrow M^{n+} + ne^- \tag{1}$$

The M^{n+} ions, following the electrical field, are attracted by the bottom electrode and diffuse through the dielectric. At the bottom electrode the ions are reduced according to the reaction (2):

$$M^{n+} + ne^- \rightarrow M \tag{2}$$

The M^{n+} ions are reduced on these new M atoms, which progressively leads to the formation of a conductive metallic filament between the two electrodes as observed in b). The memory stack is in the low resistive state.

In c) the reset of the memory is shown. The voltage is reversed and the reactions are therefore inversed. The metal M in the filament plays the role of the active electrode and the M ion source layer plays the role of the inert electrode. The metallic filament is thus dissolved in the ion source layer.

Once the filament is erased, the memory can be written and then erased again. The number of writing/erasing cycles supported by the memory before a degradation of the HRS/LRS ratio is called endurance. We can also define the data retention as the time during which the data are stored without degradation and the variability, which corresponds to the ability of the memory to show a similar electrical behavior between different cycles (cycle-to-cycle) or between different devices of a same stack (device-to-device).

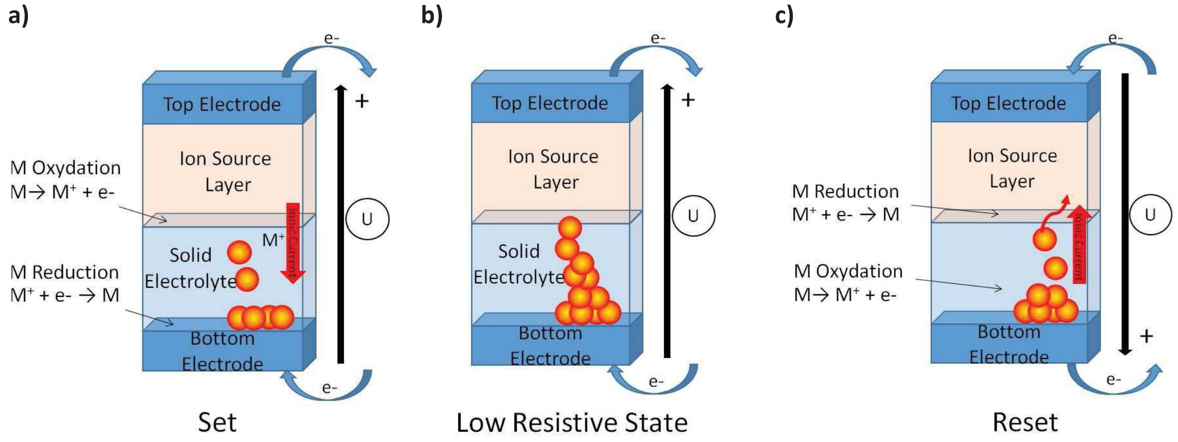

Set Low Resistive State Reset

Figure 9: Schematic diagram for the electrochemical forming, with (a) the formation of the filament or set, (b) the low resistive state with a metallic conductive filament connecting both electrodes and (c) the dissolution of the filament or reset

1.4.3. Materials often used in CBRAM

In CBRAM stack the materials often used for the dielectric layer are numerous. We can cite the oxides, the chalcogenides and the halides [13]. This thesis will focus on metal oxides. As we will see later in the state of the art in 3.2, oxygen seems to have an important role during the electro-forming. For ion source layers, the chemical elements often used in order to form the conductive filament are copper and silver, due to their high ion mobility and their capacity to be easily oxidized or reduced [13], properties which are required to obtain a working memory. In order to protect this metal from oxidation due to contact with atmosphere, a fourth layer is added to the stack: the top electrode (see Figure 10). It must be conductive, electrochemically inert to avoid chemical reactions when applying the electrical field, inert toward oxygen to protect the ion source layer and compatible with CMOS process. For this purpose materials such as TiN or Ta are often used. As the bottom electrode requires similar properties, similar materials are also generally used together with tungsten as bottom electrode.

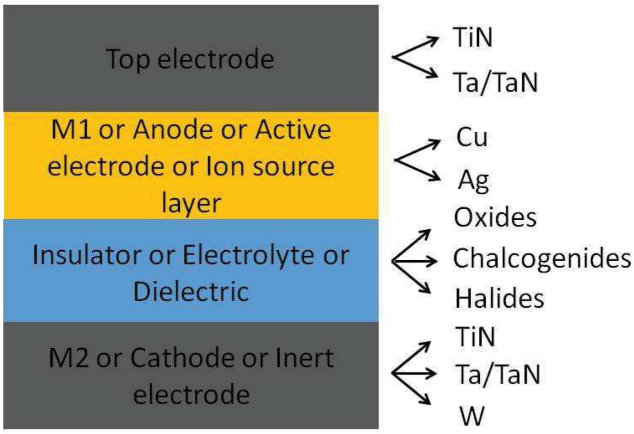

Figure 10: CBRAM memory stack

1.5. Problematic

Already at the beginning of this work, we noticed through literature survey that the ReRAM mechanisms are complexes: the main phenomena seem to be drawn on electrochemical effects, drifting ions under the applied field and resulting in the formation of a conductive path. But it also appeared possible to find several electronic explanations, such as space-charge-limited conduction, charge trapping, etc… These mechanisms, occurring in CBRAM, occur also in OXRAM. In fact, OXRAM and CBRAM are so similar that hybrid CBRAM/OXRAM memory has already been proposed in literature ([15]-[17]). It combines both conduction mechanisms, i.e. a conductive metallic filament (CBRAM) and oxygen vacancies (OXRAM). This presence of both kinds of conduction mechanisms may be explained by the fact that a metal element may require an oxidant to complete an Ox/Red reaction [18].

To go further, a ReRAM memory is a system that must retain and release information, which can be modeled in at least two stable states separated by a barrier height as visible in Figure 11 a). To allow a fast transition at the lowest possible energy, it is preferable for such bi-stable system to be near instability. Stated differently, the barrier height should be low enough to insure a low electrical consumption of the memory.

In the meantime, the stability of a bipolar ReRAM can be seen as the following reaction (3) [19], if one takes oxygen as the mobile agent:

$$\mathrm{MO_x(Red)} + \mathrm{mO^{2-}} \overset{\Delta G}{\Leftrightarrow} \mathrm{MO_y\,(Ox)} + 2\,\mathrm{me^-} \qquad (3)$$

A small standard Gibbs free energy ΔG for this reaction implies a bi-stable system (Figure 11 a)), whereas high ΔG leads to only one stable state as observed in Figure 11 b) ([19], [20]). Therefore, a small reaction ΔG is an essential condition to realize a ReRAM, but in the meantime a low barrier energy is required to reduce energy consumption and fast transition but it also impacts the data retention. We see appearing here a complex compromise and the materials, in particular the choice of the Ox/Red couples, are essential to attain a satisfying memory operation.

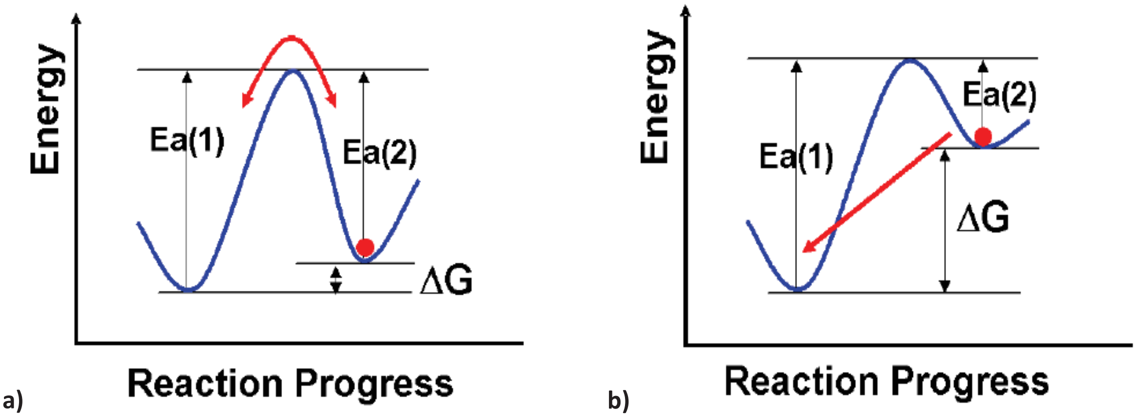

Figure 11: Energy diagrams for a) System with two stable states and an important barrier height and b) System with one stable state

Some of known couples are already working, such as Cu/SiO_2 [18] or Ti/HfO_2 [21], but the mechanisms are still remaining unclear, due to the fact that the phenomena take place at the atomic level and in dynamic conditions far away from thermodynamics equilibrium. In particular, questions around the need of an electro-forming are unanswered and understanding this very first step is mandatory to further apprehend the set and reset steps and try to solve remaining issues of ReRAM such as the retention, the endurance or more important the variability. This is the aim of this work, where we concentrated our efforts on this very first electro-forming step, using already known couples and some new proposal to assert our assumptions and improve the memory properties.

1.6. Outline

As common in a thesis manuscript, we will start to present the experimental conditions and technics used and developed to achieve our goal. Then, the third chapter is dedicated on the study of the forming mechanisms using a reference stack. It will first introduce a detailed state of the art on the forming, the choice of a CBRAM stack which will serve as reference in this work and the forming study through material characterizations. The reference stack will be composed of 20nm-$CuTe_2Ge$ ion source layer, 10nm-Ta_2O_5 electrolyte, 200nm-Ta/5nm-TiN bottom electrode and 50nm-TaN top electrode.

In chapters four and five, this reference stack will be modified layer by layer in order to assess the impact of each modification on the forming. The different behaviors observed during the forming will be studied and discussed toward the results exposed in chapter 3.

In particular the chapter 4 will focus on the role of oxygen during forming. Two modifications will be studied: one will consist in the insertion of an oxygen scavenger in the stack such as titanium or aluminum, which will reduce the dielectric. The second will be the substitution of the reference tantalum pentoxide dielectric by the gadolinium oxide, an oxide with a higher hygroscopicity and a lower standard Gibbs free energy. In other words, an oxide composed of stronger metal-oxygen bonds and a higher capacity to absorb moisture than tantalum pentoxide.

Then, in chapter 5 the modification of the ion source layer $Cu_xTe_yGe_z$ alloy will be performed in order to understand the role of each element. For this purpose, we will principally study three modifications; the first one will be a modification of the alloy composition itself, the second one the insertion of a zirconium scavenger, and the third modification will consist in removing the copper in order to study the tellurium and zirconium role. Finally, we will conclude our work and try to give some perspectives.

1.7. Bibliography

[1] P. Pavan, R. Bez, P. Olivo, and E. Zanoni, "Flash memory cells-an overview", Proceedings of the IEEE, vol. 85, no. 8, pp. 1248–1271, 1997.

[2] C. Zhao, C. Zhou Zhao, S. Taylor and P. R. Chalker, "Review on Non-Volatile Memory with High-k Dielectrics: Flash for Generation Beyond 32 nm", Materials, vol. 7, pp 5117-5145, 2014.

[3] D. Takashima, "Overview of FeRAMs: Trends and perspectives", in Non-Volatile Memory Technology Symposium (NVMTS), 2011 11th Annual, pp. 1-6, 2011.

[4] J. M. Slaughter, "Materials for Magnetoresistive Random Access Memory", Annual Review of Materials Research, vol. 39, no. 1, pp. 277–296, 2009.

[5] S. Raoux, G. W. Burr, M. J. Breitwisch, C. T. Rettner, Y.-C. Chen, R. M. Shelby, M. Salinga, D. Krebs, S.-H. Chen, H.-L. Lung and C. H. Lam, "Phase-change random access memory: A scalable technology", IBM Journal of Research and Development, vol. 52, no. 4.5, pp. 465–479, 2008.

[6] H.-S. P. Wong, S. Raoux, S.-B. Kim, J. Liang, J. P. Reifenberg, B. Rajendran, M. Asheghi and K. E. Goodson, "Phase Change Memory", Proceedings of the IEEE, vol. 98, no. 12, pp. 2201–2227, 2010.

[7] Y. Li, S. Long, Q. Liu, H. Lü, S. Liu, and M. Liu, "An overview of resistive random access memory devices", Chinese Science Bulletin, vol. 56, n° 28-29, p. 3072-3078, 2011.

[8] P. A. N. Feng, C. Chao, Z. Wang, Y. Yang, Y. Jing, et Z. Fei, "Nonvolatile resistive switching memories-characteristics, mechanisms and challenges", Progress in Natural Science: Materials International, vol. 20, p. 1–15, 2010.

[9] J. S. Meena, S. M. Sze, U. Chand, and T.-Y. Tseng, "Overview of emerging nonvolatile memory technologies", Nanoscale research letters, vol. 9, no. 1, p. 1, 2014.

[10] R. Waser, R. Dittmann, G. Staikov, and K. Szot, "Redox-Based Resistive Switching Memories - Nanoionic Mechanisms, Prospects, and Challenges", Advanced Materials, vol. 21, no. 25–26, pp. 2632–2663, 2009.

[11] S. Blonkowski and T. Cabout, "Bipolar resistive switching from liquid helium to room temperature", Journal of Physics D: Applied Physics, vol. 48, no. 34, p. 345101, 2015.

[12] G.-S. Park, Y. B. Kim, S. Y. Park, X. S. Li, S. Heo, M.-J. Lee, M. Chang, J. H. Kwon, M. Kim, U-I. Chung, R. Dittmann, R. Waser and K. Kim, "In situ observation of filamentary conducting channels in an asymmetric Ta_2O_{5-x}/TaO_{2-x} bilayer structure", Nature Communications 4, no. 2382, 2013.

[13] I. Valov and M. N. Kozicki, "Cation-based resistance change memory", Journal of Physics D: Applied Physics, vol. 46, no. 7, p. 074005, 2013.

[14] I. Valov, R. Waser, J. R. Jameson, and M. N. Kozicki, "Electrochemical metallization memories—fundamentals, applications, prospects", Nanotechnology, vol. 22, no. 28, p. 289502, 2011.

[15] L. Yang, C. Kuegeler, K. Szot, A. Ruediger, and R. Waser, "The influence of copper top electrodes on the resistive switching effect in TiO_2 thin films studied by conductive atomic force microscopy", Applied Physics Letters, vol. 95, no. 1, p. 013109, 2009.

[16] Y. Kang, M. Verma, T. Potnis, T. Liu, and M. Orlowski, “Conditions for Formation and Rupture of Multiple Conductive Cu and V_O Filaments in a Cu/TaO_x/Pt Device”, ECS Transactions, vol. 50, no. 34, pp. 19–24, 2013.

[17] H. Jeon, J. Park, W. Jang, H. Kim, H. Song, H. Kim, H. Seo and H. Jeon, “Resistive switching behaviors of Cu/TaO_x/TiN device with combined oxygen vacancy/copper conductive filaments”, Current Applied Physics, vol. 15, no. 9, pp. 1005–1009, 2015.

[18] S. Tappertzhofen, I. Valov, T. Tsuruoka, T. Hasegawa, R. Waser, and M. Aono, “Generic Relevance of Counter Charges for Cation-Based Nanoscale Resistive Switching Memories”, ACS Nano, vol. 7, no. 7, pp. 6396–6402, 2013.

[19] Z. Wei, “TaOx ReRAM Device and Array”, in 2013 IEEE 5th International Memory Workshop (IMW), 2013.

[20] Z. Wei, R. Yasuhara, K. Katayama, T. Mikawa, T. Ninomiya, and S. Muraoka, “Quantitative method for estimating characteristics of conductive filament in ReRAM”, in 2014 IEEE International Symposium on Circuits and Systems (ISCAS), pp. 842–845, 2014.

[21] K. Beckmann, J. Holt, H. Manem, J. Van Nostrand, and N. C. Cady, “Nanoscale Hafnium Oxide RRAM Devices Exhibit Pulse Dependent Behavior and Multi-level Resistance Capability”, MRS Advances, vol. 1, no. 49, pp. 3355–3360, 2016.

Chapter 2: Deposition and characterization techniques

2.1. Deposition techniques

2.1.1. Sputtering deposition

The sputtering deposition is a Physical Vapor Deposition (PVD) technique which enables the deposition of thin films, from few nanometers to hundreds of nanometers [1].

The sputtering deposition consists in sputtering a solid target composed of the material to deposit thanks to plasma. For this purpose the target and the substrate are placed into a chamber under vacuum (see Figure 12). To form the plasma an inert gas, such as argon, is injected in the chamber while a potential is applied between the chamber walls and the target, which represents the cathode. The Ar^+ ions present in the plasma are attracted by the target and sputter the target surface. Target atoms deposit on the substrate surface, forming the thin film.

A second gas can also be injected with argon, such as N_2 or O_2. In this case the argon ions sputter the metallic target and O_2 (or N_2) reacts with the sputtered atoms, forming an oxide (or nitride) which is deposited on the substrate. Such deposition is called reactive sputtering deposition. Another technique, called co-sputtering, consist in sputtering two targets at the same time. This enables to deposit alloys with different compositions.

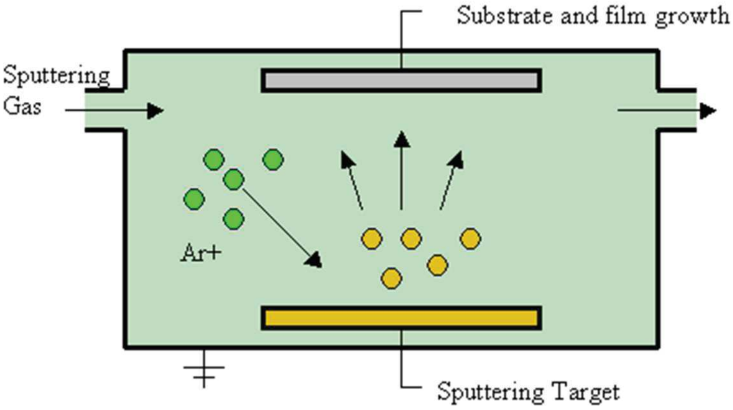

Figure 12: Sputtering deposition principle

In this thesis the equipment used for sputtering deposition is an EVATEC/OERLIKON Clusterline 200, which is an industrial equipment with five chambers as visible in Figure 13 a). The wafers are loaded under vacuum in the equipment via the load locks. The robotic arm in the center enables the manipulation of wafers between the different chambers under vacuum. Therefore, several layers can be deposited without air break, which prevents films oxidation between each layer deposition.

The platform is composed of two chambers dedicated to the wafer preparation (a preclean chamber and a degas chamber), and three chambers dedicated to deposition. The Ti/TiN PVD chamber can deposit Ti or TiN through reactive sputtering, the PVD co-sputtering chamber is principally dedicated to co-sputtering deposition of metallic oxides and chalcogenides and can contain four targets, placed as shown in Figure 13 b) and the $CuTe_2Ge$ PVD chamber, which sputters a $CuTe_2Ge$ target.

During this thesis all the chambers were used. The substrates were 200mm-Si wafers and the deposition parameters will be detailed in the next chapters for each deposited film.

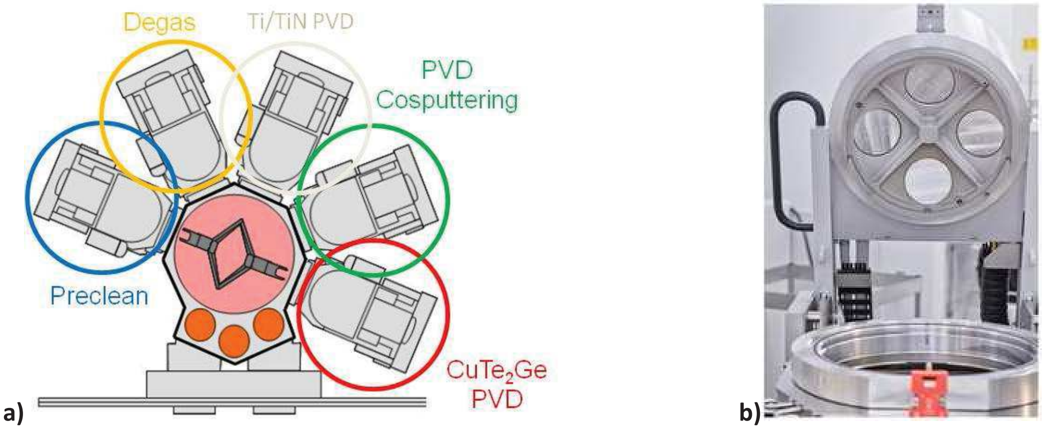

Figure 13: a) Schema of the OERLIKON Clusterline 200 ; b) Detail of the PVD Co-sputtering chamber

2.1.2. Masking technique

The shadow mask technique is a very simple method to define memory cells. It consists in a rigid mask tapped on top of the wafer prior dielectric or ion source layer deposition. In this thesis, it will be applied between the dielectric and the ion source layer in order to limit the oxidation of the bottom electrode due to air break. As described in Figure 14, after the deposition of the dielectric the mask is positioned and fixed with Kapton tape. Then the ion source layer and top electrode is deposited. When the stack is finished the mask is removed, leaving the memory cells apparent.

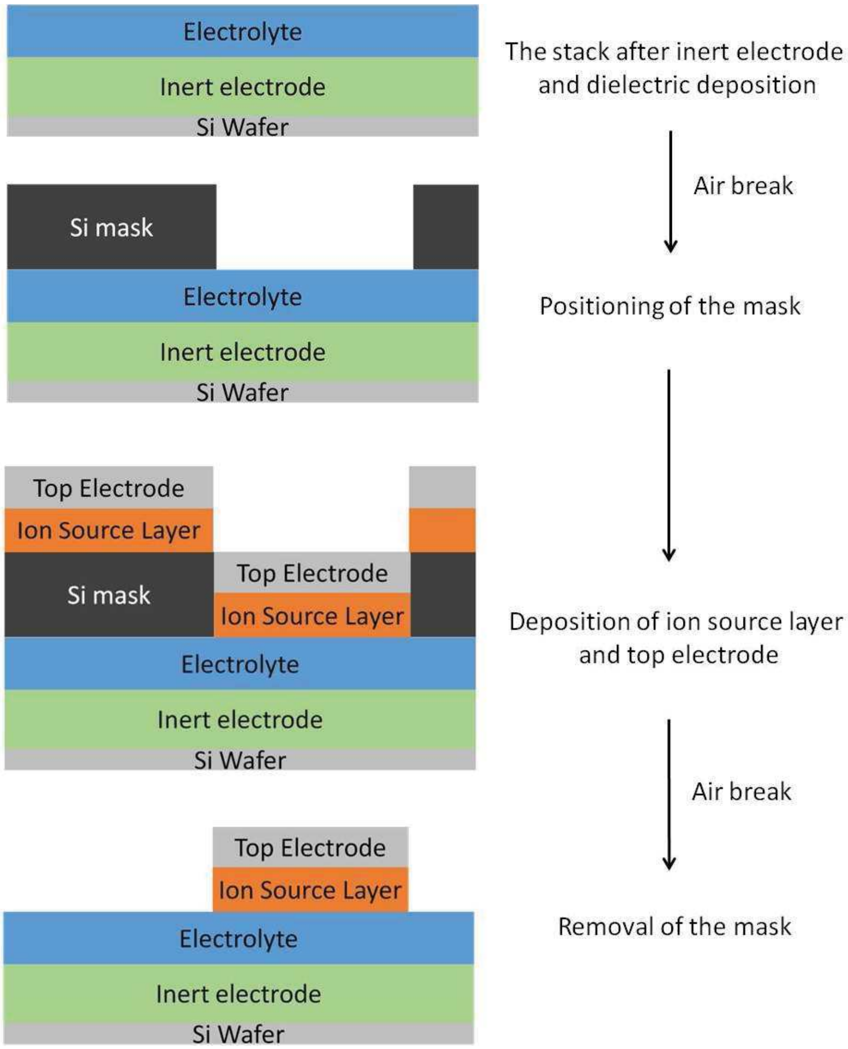

Figure 14: Deposition steps for masking technique

This technique is easy to set in place, however it brings constraints and variability for the electrical tests. All details will be given in 2.2.1.

The mask used in this thesis is presented in Figure 15. It is made of 100mm-silicon wafer, and the holes are drilled by laser with diameters of 2mm, 1mm and 0.5mm. The memory stacks studied with HAXPES and ToF-SIMS (see 2.2.2.1 and 2.2.2.2) will have a diameter of 2mm in order to ease the material characterizations.

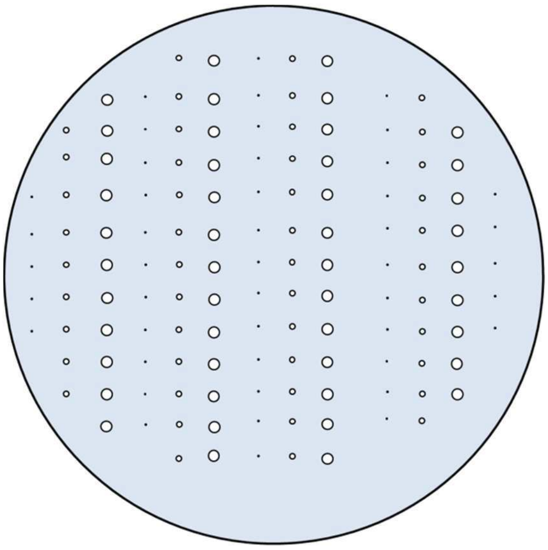

Figure 15: Silicon mask diagram

2.1.3. 1R integration

In this work some memory cells are integrated in 1R configuration (one resistive element), the schematic cross-section for an Al_2O_3/ZrTe/TaN memory stack is visible in Figure 16. We see that the integration enables a direct contact with the bottom electrode and the ion source layer is capped, contrary to cells formed thanks to shadow mask technique.

As we will see in 2.2.1.2, integrated memories cannot enable a material characterization of the stack, however they have a better reliability in electrical tests than memories deposited using the shadow mask technique.

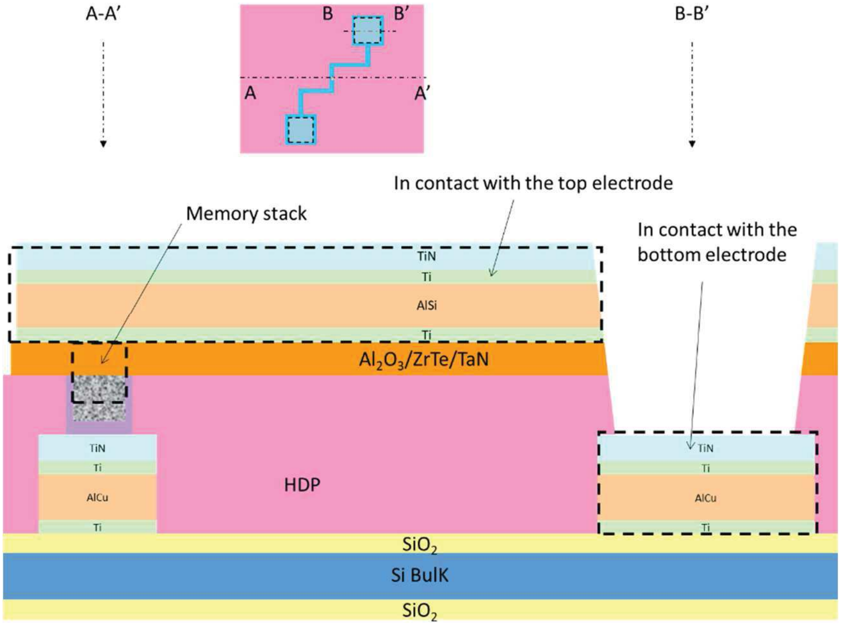

Figure 16: Schematic section of full sheet integration

2.2. Characterization techniques

2.2.1. Electrical tests

2.2.1.1. Experiment

With the memories obtained thanks to the shadow mask technique, electrical tests were performed with a generator Keithley 2635A system source meter and the contacts were made with a gold wire and a needle probe. The gold wire has a diameter of 0.5mm and is bended at its extremity to ease and ensure the top contact, as described in Figure 17. The wire vertical position is modified by hand and the contact is taken in the bended area. The bottom electrode is contacted by the needle probe. As the electrode is capped by the dielectric, one must scratch the latter with the needle probe. As the force to scratch the dielectric is not monitored, it is easy to imagine that the bottom electrode could also be easily scratched and removed. Thus, the last one must be thick enough to support scratching.

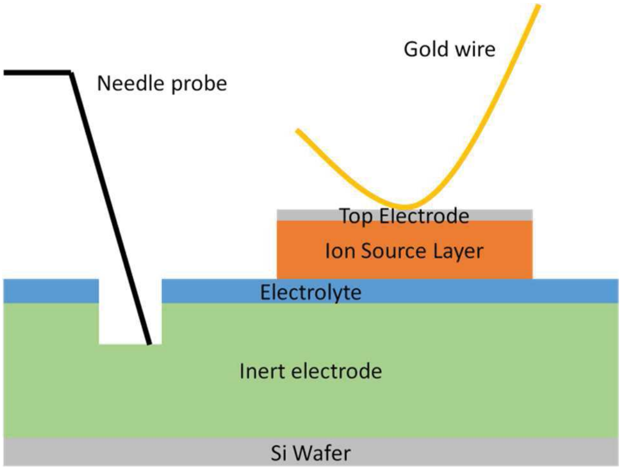

Figure 17: : Schematic section of a CBRAM with the electrical assembly

Once the contacts are taken, the potential is applied and some writing/erasing cycles performed. The voltage is increased step by step from 0V until a maximum voltage V_{max} and the current is measured at each step. Then, the voltage is reversed and the same process is performed for the reset.

For cycling, one must imposed to the generator some constraints. First, the range of voltage used V_{max} and V_{min} (see Figure 18), the step used, the compliance current CC which is the maximum current flowing in the memory stack (it protects the memory from irreversible breakdown), the number of cycles and if a reading step must be performed between the different resistivity states.

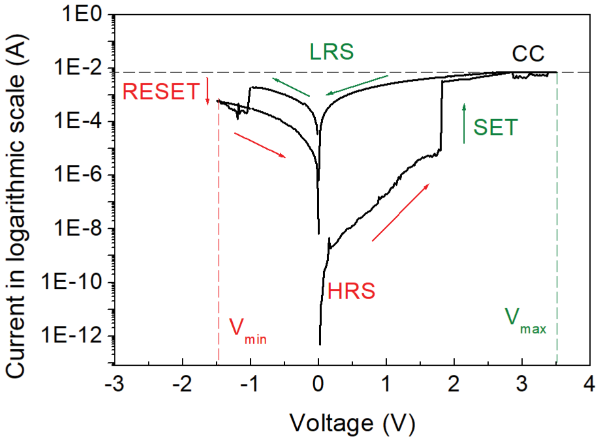

Figure 18: Typical current-voltage curve of $Ta_2O_5/Cu_{60}Te_{40}Ge$ bipolar memory

For the reading a ramp is performed from 0V to a small voltage, which is in this work around 0.1V. The current-voltage curve obtained is linear as it corresponds to the Ohm's law. The step used for all tests is 0.15V for cycling and 0.0025V for reading.

2.2.1.2. Electrical tests variability

Figure 19 shows a wafer diagram presenting the typical statistic acquired during electrical tests (here for a Ta 200nm/TiN 5nm/Ta_2O_5 10nm/$CuTe_2Ge$ 15nm/TiN 50nm memory stack). We can remark that on 28 memory cells tested, only 5 show a cycling behavior (meaning they can perform more than 1 writing/erasing cycle) and 6 cells can be formed and eventually partially erased but they cannot be written again in a second cycle. The 17 other memories do not present any forming as they are already in a low resistivity state at the beginning of the tests. To summary in this wafer 18% of the cells work and can be studied, 21% can be formed but not cycled and 61% are not useable.

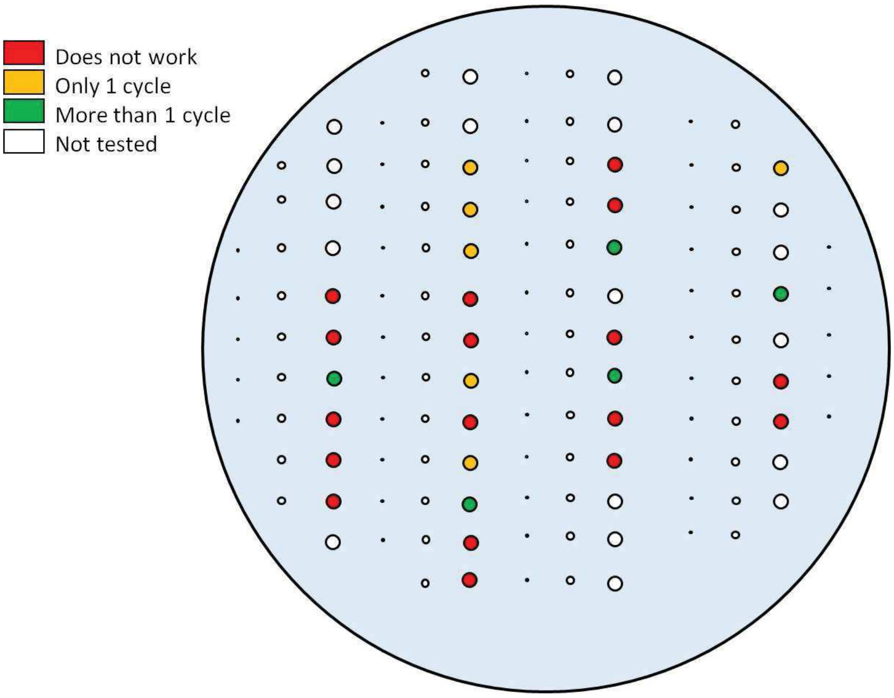

Figure 19: Wafer diagram with typical statistic for electrical tests

These statistics imply that the working cells, where a detailed electrical study can be performed, are very few on a single wafer. It also implies that electrical tests require lots of tries before finding a cell which can cycle. This can be due to several parameters. First, the experimental error induced by the difficulty to perform the contact with the gold wire. Actually such measurement bench is complex to set in place: wire position on the wafer and its height position are modified by hand, which implies a lack of precision. Moreover, devices formed with the shadow mask technique have been impacted by the air breaks between the dielectric and the ion source layer deposition, which could have brought more oxygen in the stack. Additionally, the ion source layer is not completely capped as the vertical edges are not recovered by the top electrode. Thus these edges can be a source of oxidation. Then, the large size of the devices can impact the cells reliability [3]. Finally, the reliability inherent to the chosen stack should also be taken into account.

Statistics can be improved by using integrated memories as the devices are smaller, the layers capped and the electrical tests more automated. However, such integration does not enable material characterizations such as ToF-SIMS (2.2.2.2) or HAXPES (2.2.2.1), contrary to the large devices made with the shadow mask technique.

2.2.2. Physical-Chemical characterizations

2.2.2.1. X-Ray Photoelectron spectroscopy

(i) Principle

The X-Ray Photoelectron Spectroscopy (XPS) is a non-destructive surface characterization method, which analyzes the chemical elements and their bonds present on the surface (around 10nm in depth). This technique is based on the emission of photoelectrons from the sample induced by X-rays.

For this purpose the sample is irradiated by X-rays with a known energy hν (h the Planck constant in J.s and ν the frequency, in s^{-1}) [4]. To eject electrons from their energy level and thus create photoelectrons, the energy of the incident photon must be higher than the energy of the electron which will be excited. However, to have a better efficiency, the photon energy must be just a little higher than the binding energy of the electron. X-rays can be provided by different sources, which all have a different energy. Among them one can find Al K_α and Mg K_α. The source used in this thesis for the XPS analyses is Al K_α, which has an energy of 1486.6eV.

When the sample is submitted to X-rays, the electron excited leaves its level of energy and is released (see Figure 20 a)). This photoelectron has a kinetic energy E_{kin} which is measured by the XPS analyzer. The conservation of energy gives us the following formula (4):

$$E_{bd} = h\nu - E_{kin} = E_i - E_{kin} \tag{4}$$

As the kinetic energy of the photoelectron and the incident energy of the X-ray beam are known, the binding energy E_{bd} of the electron excited can be easily calculated. Therefore the binding energy of the electron can be known. As each chemical elements have different energy levels, this E_{bd} value can be used to identify the chemical element. In the case of chemical bonds the binding energies are slightly modified as described in Figure 20 b). When the element A observed is bonded with an element B with a higher electronegativity the binding energy increases. Inversely, when the electronegativity is lower than the element A observed, the binding energy decreases. Thanks to these energy modifications the bonds can also be identified.

One can remark here that in the case of an insulator analysis charge effect can appear. Charges are formed in the layer during the analysis, which increases the energy of the photoelectrons emitted. This increase is the same for each element detected. Therefore, in order to study the correct binding energies, XPS spectra must be recalibrated. For this purpose a reference is chosen: C*1s*. In this thesis C*1s* is fixed at 284.5eV.

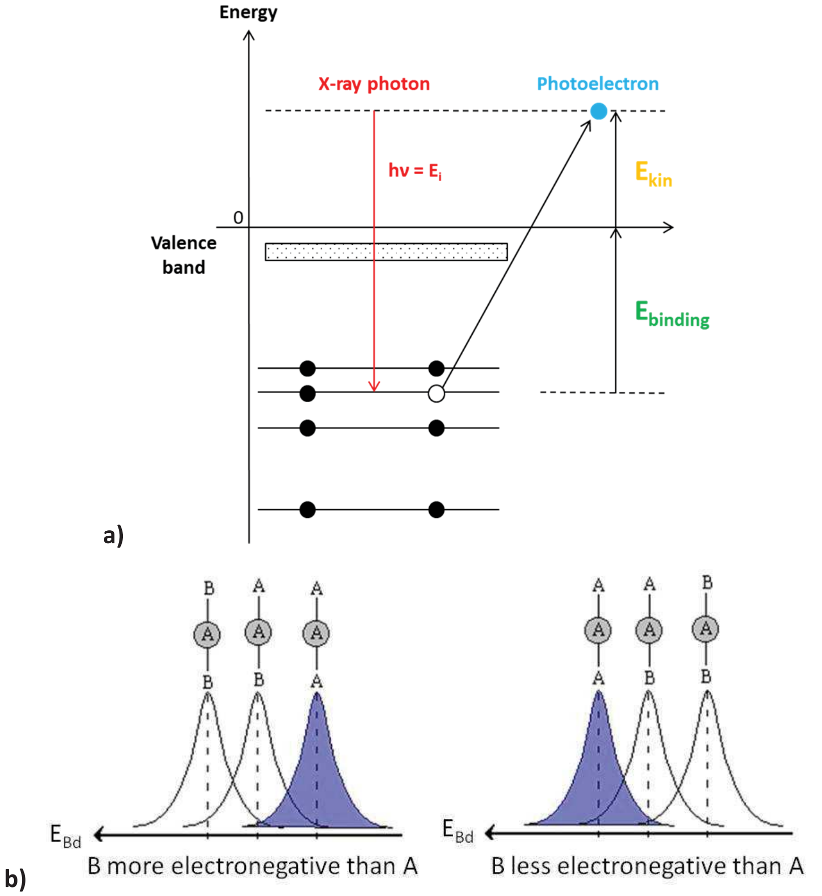

Figure 20: a) XPS principle ; b) Impact of electronegativity on XPS spectra

The depth analyzed by XPS depends of the incident angle of the X-ray beam. Therefore a depth profile can be obtained by using several incidence angles or by detecting the photoelectrons in several ranges of angles when analyzing a sample. This technique is called Angle Resolved XPS (ARXPS).

Moreover, the depth analyzed depends also of the incident energy of the X-ray beam. Therefore, X-rays with a higher energy enables a deeper analysis in matter. HArd X-rays PhotoElectron Spectroscopy (HAXPES) uses hard X-rays, which have an energy higher than 10keV. This technique is particularly useful in this thesis as it enables us to analyze an entire memory stack instead of one or two layers. However, such hard X-rays cannot be obtained in laboratory and need a synchrotron facility.

(ii) Synchrotrons for HAXPES measurements

A synchrotron is a particle accelerator, principally composed of an injector, an accelerator ring, a storage ring and beam lines.

In Figure 21 it is possible to see the injector in red. This is where the electrons are emitted and progressively accelerated by an electrical field. Then, electrons are injected in the accelerator ring, in green in Figure 21 (to give an idea of the dimensions, in ESRF this small ring measure 300m of circumference). Here the energy of electrons is increased until their final energy, of the order of the GeV, thanks to accelerating cavities. As electrons move in straight line it is necessary to bend their trajectory. For this purpose bending magnets are dispatched all around the ring. Moreover, as the energy of electrons increased at each turn, to be still efficient the field must be increased in synchronization with the increasing electron energy. This required synchronization gives the name "synchrotron" to this particle accelerator.

Once their final energy is reached, electrons are sent into the storage ring, visible in blue in Figure 21 and which measures 844m of circumference at ESRF. There, electrons can circulate during hours and their trajectory passes through bending magnets, focusing magnets and inverters. The bending magnets control their trajectory, the focusing magnets focus the electron beam and make it as thinner as possible and inverters are used to obtain a more intense photon beam than with bending magnets. Indeed, at each direction change (with inverters or bending magnets), electrons loose energy in an electromagnetic radiation form called synchrotron radiation. These beams are used in beam lines for the experiments (in yellow in Figure 21), in our case for HAXPES analyses. In this thesis the analyses were performed in two synchrotrons: ESRF in Grenoble and SPring8 in Japan.

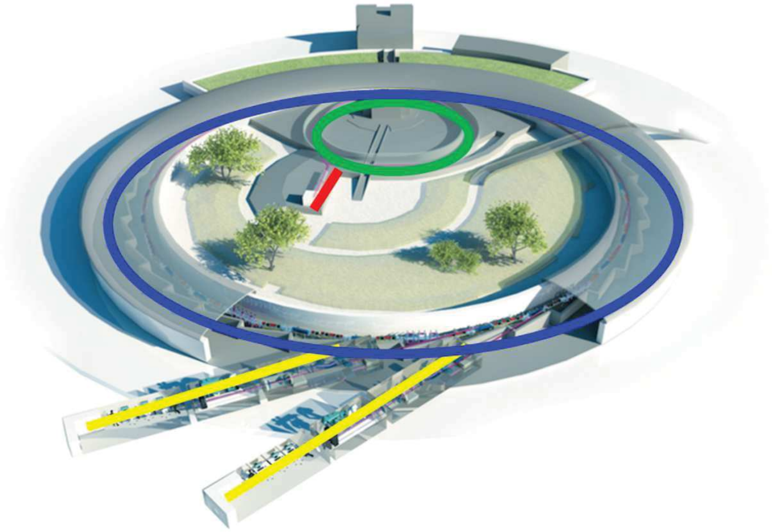

Figure 21: Principal elements of a synchrotron

The Super Photon Ring – 8GeV, called SPring-8, is located in Japan, Hyôgo prefecture. It was open in 1997 and is currently managed by the research institute RIKEN and the Japan Synchrotron Radiation Research Institute (JASRI). The electron beam has an energy of 8GeV and 47 beam lines are currently distributed around the storage ring.

The European Synchrotron Radian Facility or ESRF is located in Grenoble, France. Inaugurated in 1994, it is supported by 22 countries: 13 members (France, Germany, Italy, UK, Spain, Switzerland, Belgium, The Netherlands, Denmark, Finland, Norway, Sweden and Russia) and 9 associated countries (Austria, Portugal, Israel, Poland, Czech Republic, Hungary, Slovakia, India and South Africa). The synchrotron electron beam has an energy of 6GeV and 44 beam lines are currently distributed around the storage ring.

In ESRF the beam line which has welcomed our analyses is the Beam Line 25 (BM25) or SpLine. It is a Spanish beam line, divided into two branches. The branch A, which is dedicated to the High Resolution Powder Diffraction (HRPD) and the X-ray Absorption Spectroscopy (XAS) and the branch B, dedicated to the Surface X-Ray Diffraction (SXD) and the Hard X-Ray Photoelectron Spectroscopy (HAXPES) [5].

At the ESRF the HAXPES incident energy used is 15.0keV. At SPring8 the incident energy is 7.9keV, which is lower than in ESRF. It implies that the thickness analyzed is lower than in ESRF. However, in SPring8 the HAXPES has a better binding energy resolution than in ESRF BM25. Therefore, spectra are more resolved than at ESRF.

2.2.2.2. Time-of-Flight Secondary Ion Mass Spectroscopy

The Time-of-Flight Secondary Ion Mass Spectroscopy (ToF-SIMS) is a destructive qualitative characterization method which enables to determine the depth profile of multilayer stacks. It is based on the secondary ions emission during the sputtering of the sample surface. The SIMS is the most sensitive surface analysis technique, with an elemental detection limits range of parts per million to parts per billion [6].

For this purpose ions with an energy of few keV are focalized on the sample surface (on a squared area of some hundreds of µm by hundreds of µm). These incident ions sputter the surface, layer by layer (see Figure 22). The charged particles ejected are called secondary ions and they are collected and analyzed by the time of flight spectrometer. The ToF spectrometry is a mass spectrometry technique which identifies ions mass thanks to their velocity. Velocity is calculated thanks to the time taken by the ions to reach the detector, positioned at a known distance. As ions velocity depends on their mass-to-charge ratio, from this ratio and analysis results the ion can be identified. A depth profile is then obtained by plotting the intensity of each identified ions with the sputtering time which corresponds to the sample depth.

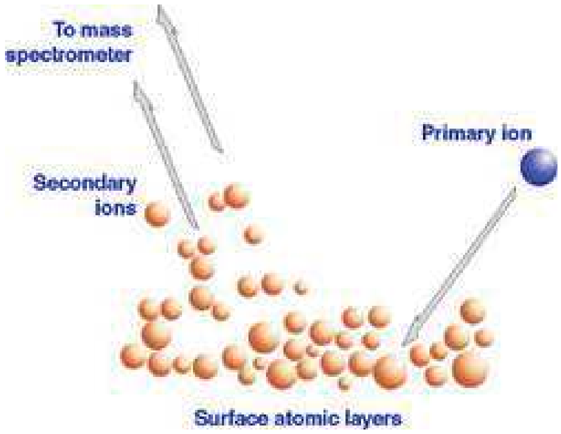

Figure 22: SIMS principle

One can highlight here that as the ionization yield depends of the atomic environment of the element, when studying a stack of several layers some matrix effects can appear at the interfaces. Moreover, during the sputtering some atoms can be repelled in the sub layers, thus in the spectra of this thesis the interfaces positions will be just roughly estimated.

2.2.2.3. X-ray reflectivity

X-Ray Reflectivity (XRR) is a non-destructive characterization method which enables to measure the thickness, the density and the roughness of a thin layer or of a multilayer stack (few nm to 1µm). It is based on the reflectivity of X-rays in the studied layers. In this thesis the thicknesses of the layers deposited were always controlled by XRR.

For this purpose the sample is irradiated by X-rays with an incident angle called angle of reflection, which is the angle enabling the reflection of X-rays in the thin film. These reflected X-rays are collected and their intensity according to the angle is plotted. The obtained curve is presented in Figure 23. The slope of the curve is related to the roughness, the critical angle depends on the density of the layer and the period of the interference fringe gives the thickness of the layer. To extract this information a model simulation is used. A reference curve is created thanks to an estimated stack and then the software try to adjust the parameters of the model curve in the order to obtain the overlapping of the two curves.

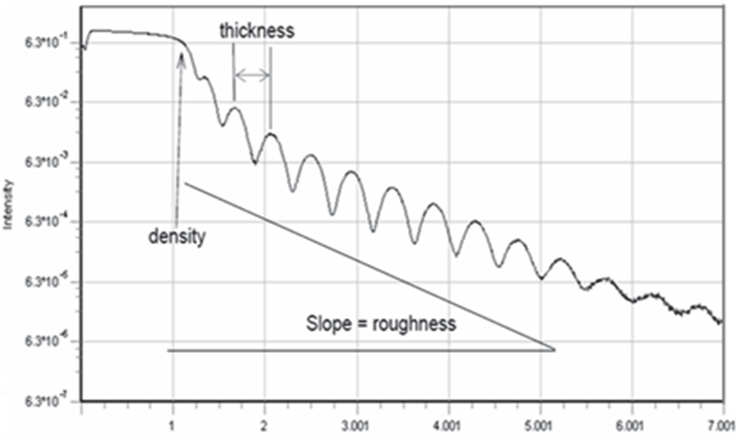

Figure 23: Typical XRR spectrum

2.2.2.4. X-ray diffraction

X-Ray Diffraction XRD is a non-destructive characterization technique which is used to study the crystallinity of a layer thanks to the diffraction of X-rays in the studied layer.

For this purpose the sample is irradiated by X-rays. If the layer is crystalline the beam will be diffracted in several directions: it is an elastic diffusion which appears when X-rays encounter an atom. The rays are diffracted in directions which depend on the size and the orientation of the crystal structure. In this thesis the source of the beam used is Cu Kα with a wavelength of 1.5nm.

2.2.2.5. Wavelength Dispersive X-Ray Fluorescence

The Wavelength-Dispersive X-Ray Fluorescence, WDXRF, enables us to know the chemical composition of a layer thanks to the fluorescence of the studied sample.

For this purpose X-rays irradiate the sample, which emits energy on the form of X-rays. This emission of X-rays is called fluorescence. Two spectrometers can be used to analyze the X-rays, the one used here is the Wavelength Dispersive Spectrometer (WDS). The WDS, used in WDXRF, separates the photons according to their energy by diffraction into a crystal before their detection. These photons are specific to the elements from which they come from, therefore the composition and the amount of atoms per cm^2 of the layer can be estimated.

2.2.2.6. Rutherford Backscattering Spectroscopy

Rutherford Backscattering Spectroscopy (RBS) is a non-destructive characterization method which enables to quantify the chemical elements present in the studied layer. It is based on the backscattering of incident ions on the atoms of the studied sample.

As presented in Figure 24, ions with an energy of the order of few MeV, are sent on the sample. These incident ions present an elastic diffusion when they enter in contact with the sample. Their energy is measured and depends on the atom encountered. In other words an energy identifies a specific atom. Finally, a simulation is required to extract the composition information from the results. In this thesis the RBS incident beam is constitute of $^4He^+$ with an energy of 2.0MeV.

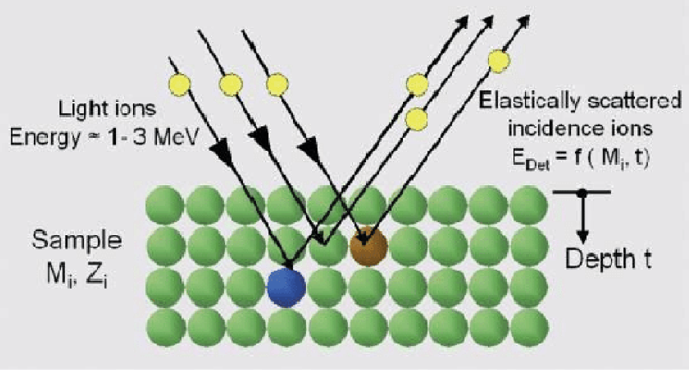

Figure 24: RBS principle

One can notice that for light elements analysis, such as oxygen and nitrogen, the Nuclear Reaction Analysis (NRA) is combined with RBS. NRA principle is based on the particles ejected during nuclear interactions between an incident beam and the atoms composing the studied layer. In this thesis the incident beam is composed of deuterons (nucleuses of deuterium, one of the stable isotopes of hydrogen) and has an energy of 930keV. A comparison with an Al_2O_3 thin film is used to determine the oxygen quantity in the sample. This value is then used as reference in the RBS simulations.

2.3. Bibliography

[1] D. M. Mattox, “Handbook of physical vapor deposition (PVD) processing: film formation, adhesion, surface preparation and contamination control”. Westwood, N.J.: Noyes Publications, 1998.

[2] P. A. N. Feng, C. Chao, Z. Wang, Y. Yang, Y. Jing, et Z. Fei, “Nonvolatile resistive switching memories-characteristics, mechanisms and challenges”, Progress in Natural Science: Materials International, vol. 20, p. 1–15, 2010.

[3] S.-J. Choi, J.-H. Lee, H.-J. Bae, W.-Y. Yang, T.-W. Kim, and K.-H. Kim, “Improvement of CBRAM Resistance Window by Scaling Down Electrode Size in Pure-GeTe Film”, IEEE Electron Device Letters, vol. 30, no. 2, pp. 120–122, 2009.

[4] T. M. Duc, “Analyse de surface par ESCA - Principe et instrumentation”, in Techniques de l’Ingénieur l’expertise technique et scientifique de référence, p. 2625, 2012.

[5] J. Rubio-Zuazo and G. R. Castro, “SpLine: Spanish BM25 CRG X-Ray beamline at the European Synchrotron Radiation Facility”, in Sociedad Española de Mineralogia, Seminar on Synchrotron Radiation in Mineralogy, vol. 6, pp. 89–108, 2009.
[6] E. Darque-Ceretti, H.-N. Migeon, and M. Aucouturier, “Émission ionique secondaire SIMS: Principes et appareillages”, Techniques de l’ingénieur. Analyse et caractérisation, vol. 12, no. P2618, pp. P2618–1, 1998.

Chapter 3: Study of forming mechanisms in a CBRAM stack

3.1. Introduction

As already explained in chapter 1, the CBRAM forming involves complex mechanisms with localized phenomena at the nanometer scale. These mechanisms are currently not well understood and they are going to be studied in this thesis. To take place, the CBRAM forming needs a “working” memory stack. In other words, in order to switch the CBRAM, the stack must be composed of specific layers such as electrodes, ion source layer and electrolyte. Each one must be composed of defined materials such as a metal able to supply ions during the forming, a dielectric where the diffusion of ions under electrical field is possible,… Otherwise, the phenomena leading to the memory effect cannot take place.

In this chapter, we will try to realize an effective CBRAM stack, arising from literature survey. As already explained in 1.6, this stack will then serve as reference in the other chapters, where the dielectric and ion source layer will be modified. For this purpose, in the first part of this chapter, we will focus on the forming effect and the related state of the art on this subject. Then, the choice of the stack will be detailed layer by layer. Finally, in the last part, the forming of the chosen memory stack will be studied through material characterizations.

3.2. Forming in metal oxides: State of the art

As presented in the 1.4.2, the CBRAM principle is believed to be based on the electrochemical formation and dissolution of a metallic filament through an insulating layer. Formation and dissolution of this conductive filament induce low or high resistive variations of the insulating layer, which are used to retain information in the form of bits ([1]-[3]). For this purpose the CBRAM stack is composed of a Metal 1/Insulator/Metal 2 stack (also called MIM stack), with Metal 1 different from Metal 2 in term of chemical properties, such as oxygen solubility or affinity, or in term of electrical properties, such as the Fermi level when in contact with the dielectric.

However, depending to the stack, when the memory is in the pristine state (in other words initial or unwritten state), the first filament formation could require a higher voltage than the one used afterwards in the writing cycles ([1]-[5]). This effect of forming a first filament is clearly visible in Figure 7. Indeed, this figure presents a current-voltage curve (also called I-V curve) of a Cu/SiO_2/Pt CBRAM stack, studied in literature [1]. The first filament formation, called “forming cycle” in the graph, presents a sudden increase of current around 4V which is called $V_{SET,form}$, and reach 10nA which corresponds to the applied compliance. This increase is believed to correspond to the formation of the first filament. Then, after the dissolution of the filament with a reset voltage of less than -0.5V, a second filament is formed. This step corresponds to “subsequent cycle” in the graph. It presents an increase of the current until the 10nA compliance at around 1.5V, which corresponds to a second filament formation. Therefore, it appears here that the forming step needs a higher voltage than the next steps, as the first filament formation appears around 4V whereas the second filament formation appears around 1.5V. In this work this first filament formation, which needs a higher voltage than the others, is called “forming” and the next ones “sets”.

The memory operation is highly dependent on the chosen materials, the deposited thicknesses or the experimental conditions during electrical testing, such as the compliance applied, etc… ([6]-[8]). The main purpose of a memory stack is to be enough unstable for a certain set of parameters, such as the application of a small voltage in order to have a resistivity change. One can state the paradox of such memory where the aim is to monitor the two states of an unstable system, which must be also reliable or stable regarding other parameters. Therefore, the comprehension of the memory mechanisms is necessary.

Fundamental understanding of the relative stability of the set and reset voltages has been partially explained using physical modeling and simulations. Main model is based on the control of a current constriction in a nanometer size filament by taking into account the electro-migration force and Joule heating [9]. Nevertheless, forming is a fundamental characteristic of filamentary oxide-based memories as it enables the memory to cycle. This first transition regime has been barely studied and must be conducted if one wants to manage the inherent instability and subsequent reliability of such memories.

In Figure 25, a summary of mechanisms assumed to take place in oxide-based CBRAM during the first filament formation is displayed. The metal called M which is present in the ion source layer is expected to provide the metallic ions required to form the conductive filament.

When applying the voltage, the M metal is first oxidized (a). Thus the reaction (5) takes place at the anode ([1], [4], [10] and [11]):

$$M \rightarrow M^{n+} + ne^{-} \tag{5}$$

Then the M^{n+} ions, following the electrical field, are attracted by the cathode, thus the bottom electrode. In order to diffuse toward the bottom electrode the cations must first cross the interface between the ion source layer and the dielectric (b). Depending on the materials used in the ion source layer and in the dielectric, the energy required to jump over this barrier could be more or less important. Therefore the electrical potential required to ease the cations movement through this interface could be different according to the materials used in the stack. Finally the ions diffuse through the dielectric (c) and then are reduced at the bottom electrode (d) according to the reaction (6):

$$M^{n+} + ne^{-} \rightarrow M \tag{6}$$

Then the M^{+} ions are reduced on these new M ad-atoms, which will progressively lead to the formation of a conductive metallic filament between the two electrodes. This is obviously the phenomena occurring in an electrochemical cell, but here at nanometer scale and in solids.

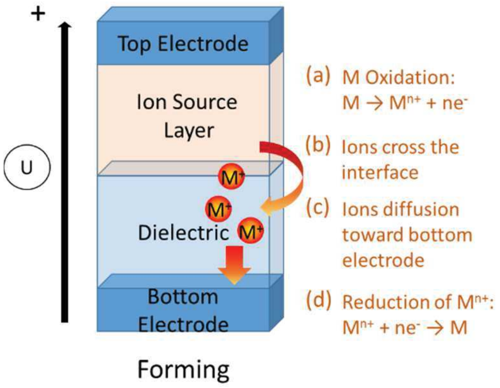

Figure 25: Mechanisms expected to take place in CBRAM forming

If we consider the CBRAM stack as an electrochemical cell (see discussion in 1.4.2), we can state that if an oxidation reaction takes place at the anode, a reduction reaction must occurs at the cathode. In literature few papers focus on this counter reaction. An interesting paper, wrote by S. Tappertzhofen *et al.* [12], focuses on the study of a Pt/SiO_2/Cu memory stack. The Figure 26 presents some of their results. In a), the evolution of the copper ion concentration in the dielectric (SiO_2) is displayed in function of the water partial pressure. It is possible to see that when the water partial pressure is increased, the copper ion concentration in the dielectric also increases. As the copper ion concentration seems to depend on moisture they deduce that the moisture, absorbed from atmosphere by the dielectric, reacts at the bottom electrode to give OH^- counter charges as depicted in b). Thus according to the authors, the counter reaction in their stack is (7):

$$\frac{1}{2} O_2 + H_2O + 2\ e^- \rightarrow 2\ OH^- \qquad (7)$$

Therefore, the moisture could play an important role of counter charges in their stack. However, if S. Tappertzhofen *et al.* chose SiO_2 as dielectric it was – among other advantages – because no OXRAM mechanism was reported with this dielectric [12]. Thus, it is possible to deduce that in the case of an oxide which could be easily reduced with the application of an electrical field, mobile O^{2-} ions could be produced together with fixed V_O^{2+} oxygen vacancies in the dielectric. These mobile O^{2-} ions could then diffuse toward the surface and thus behave as counter charges. However, the formation of V_O^{2+} oxygen vacancies is an OXRAM behavior. Therefore, the reduction of the dielectric will lead to a hybrid mechanism with both copper and oxygen vacancies filaments, as already observed in the literature ([13]-[16]).

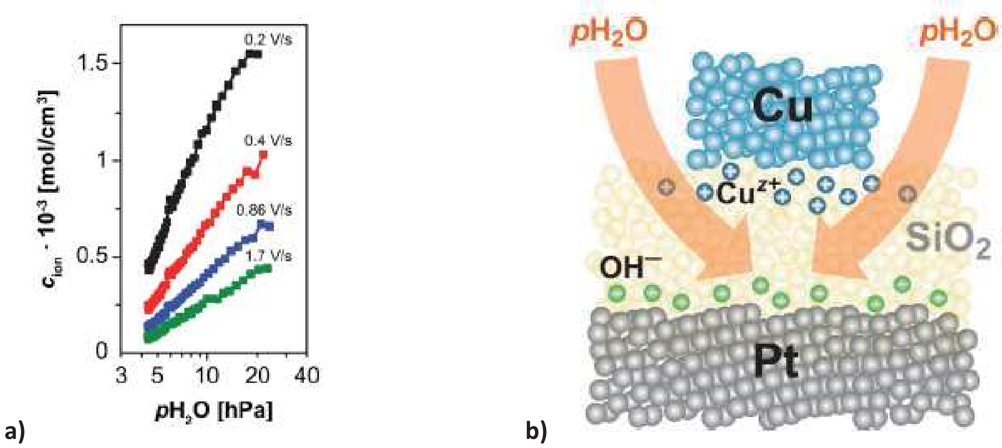

Figure 26: Study of Pt/SiO₂/Cu stack, figures extracted from [12]: a) copper ion concentration versus water partial pressure b) schematic cross section of the stack showing expected forming mechanisms

As observed previously in Figure 7, the forming appears with a higher voltage than the next writing cycles. To explain this decrease of the writing voltage in sets, literature proposed several causes. A first one, described in Figure 27 Case 1, could be due to a morphological change in the dielectric layer such as creation of vacancies, modification of the crystallography, etc... Indeed it is supposed that during the reset, thus the dissolution of the first filament, the dielectric does not return at its original state in the area of the filament. In other words the dielectric may contain more bulk defects or a different crystallography in the filament region after the reset. Therefore, during the next set this morphological change leads to a path where the ions could diffuse more easily, thus enabling a lower voltage for the set than for the forming [1]. A second reason could be the partial dissolution of the filament during the reset as described in Figure 27 Case 2. Indeed if we suppose that the filament is not completely dissolved during the reset, thus we can consider that during the set the length required to rebuild is shorter than during forming. Therefore the set requires a lower voltage than the forming ([1], [2]).

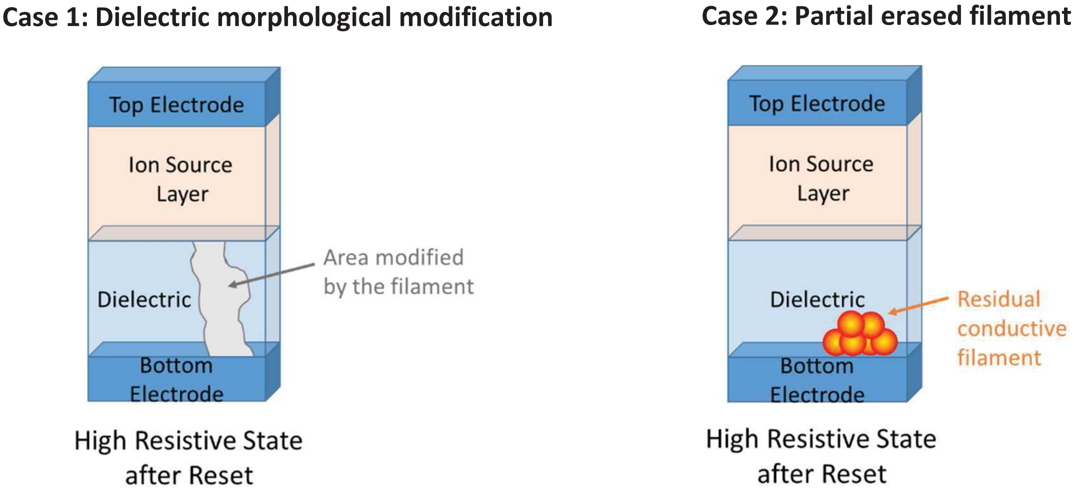
Case 1: Dielectric morphological modification

Case 2: Partial erased filament

Figure 27: Proposed mechanisms explaining the decrease of the voltage during the set

To summarize, the literature presents the forming in metal oxides as a complex phenomenon which implies several mechanisms such as reduction-oxidation reactions, ions diffusions, etc… In this work we try to simplify the system in order to study the forming in CBRAM with a metal oxide as dielectric. We deliberately decided to view the CBRAM memory as an electrochemical cell. This assumption is limited since one cannot ruled out some solid state phenomena such as electron hoping and/or tunneling through defects and this also assisted by thermal activation, etc... But, this point of view partially simplifies our study and implies that a counter diffusion of anions could be expected. Below, the choice and the study of a reference CBRAM stack is presented, whereas the study of the impact of ion source layer and dielectric on the forming mechanisms will be studied in the other chapters, through the progressive modification of the reference stack.

3.3. Choice of the reference stack

3.3.1. Choice of the ion source layer

The ion source layer provides the ions required to form the metallic filament. This work principally focuses on copper since it is commonly used as connections and wiring in standard microelectronics devices. One can notice that also silver is often used in CBRAM. Indeed both Cu and Ag have high ion mobility in dielectrics, a pre-requisite to induce metallic diffusion [4].

3.3.1.1. Copper activation thanks to Te alloying

In literature, lots of CBRAM stacks with a pure copper ion source layer deposited on the dielectric film are presented ([17]-[20]). However, first tests that we performed show that our pure copper-based memories could be written but not erased, whatever the parameters used during electrical tests. Figure 28 shows a typical current voltage curve obtained with a Cu 20nm/Ta_2O_5 10nm memory stack. When applying the voltage up to 3V, the current shows a sudden increase up to 0.01A around 1.5V. Then, when the potential is reversed no set or reset is observed, the current stays at the fixed compliance. Thus the memory can be written but not erased. Nevertheless, when alloying tellurium with copper in a CuTe alloy our memories were able to cycle. Therefore, to obtain a memory effect with the possibility to dissolve the filament in reset, a copper-based alloy is used instead of pure copper ion source layer.

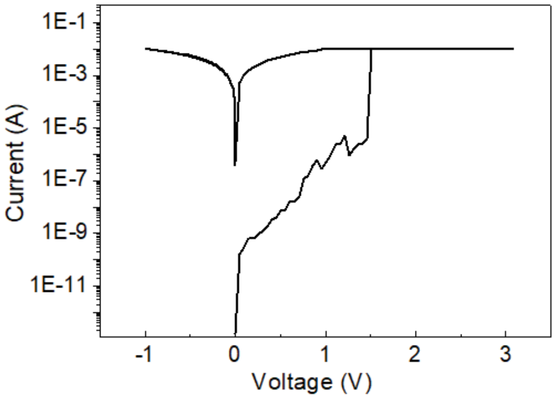

Figure 28: Typical I-V curve obtained with Cu/Ta_2O_5 stack

In literature some studies on $CuTe_x$-based CBRAM memories are presented ([7], [21]-[24]) and seems to show improved memory properties compared to pure copper-based memories ([22], [23]). Indeed, according to the composition of the alloy, $CuTe_x$-based memories show a reduction of the forming voltage and a rather stable filament. Table 1 presents the qualitative evolution of the filament stability in function of the Cu_xTe_{1-x} stoichiometry as observed in literature ([7] and [21]). It is possible to see that when the tellurium content is increased the filament is less stable. According to L. Goux *et al.* [7], this behavior could mean that the tellurium acts mainly during reset by reducing the barrier required to dissolve the formed filament. Thus, for a given reset voltage, more copper returns in the ion source layer when the tellurium content in the ion source layer is more important.

Cu_xTe_{1-x} composition	**x < 0.3**	**0.3 < x < 0.5**	**0.5 < x < 0.7**	**x > 0.7**
Commentary	Instable filament	Erase easily but not very stable filament	Stable filament $I_{reset} \approx I_{comp}$	Too stable filament $I_{reset} >> I_{comp}$

Table 1: Filament stability in function of the Cu_xTe_{1-x} stoichiometry as presented in [7] and [21]

Oxido-reduction reactions are useful to apprehend the impact of tellurium on copper dissolution in the ion source layer. Half-reactions of copper (8) and tellurium (9) show that in a CuTe alloy, Cu could be bonded to Te thanks to ionic bonds in the form of Cu^{2+} + Te^{2-}. Thus, when bonded to tellurium the copper is already in Cu^{2+} ionic form. Therefore the first step of forming, which involves the oxidation of copper (Figure 25 step (a)), requires a lower voltage than pure copper case to be performed ([10] and [11]).

$$\mathrm{Cu} \underset{\mathrm{Red}}{\overset{\mathrm{Ox}}{\rightleftarrows}} \mathrm{Cu}^{2+} + 2\mathrm{e}^{-} \tag{8}$$

$$\mathrm{Te}^{2-} \underset{\mathrm{Red}}{\overset{\mathrm{Ox}}{\rightleftarrows}} \mathrm{Te} + 2\mathrm{e}^{-} \tag{9}$$

To choose the alloy composition, one can analyze the results from literature. It seems that the most interesting Cu_xTe_{1-x} alloy composition is situated between 0.3 and 0.7. Indeed, for x under 0.3 the filament is too unstable to achieve the proper operation of the memory and for x above 0.7 the filament is too stable to be erased. However, the composition must also be chosen in relation to the integration path. Indeed, in order to be integrated in a memory as ion source layer, the CuTe must be smooth and stable in temperature, more precisely up to 400°C, the temperature reached in back end of line process. This drives the following next paragraphs: first, to check the evolution of the alloy under temperature, the phase diagram of the CuTe alloy is studied, then the surface roughness is evaluated through scanning electron microscopy (SEM) observations and finally the crystalline behavior of the alloy is studied by XRD.

The CuTe phase diagram is displayed in Figure 29. In a), it shows the phases found in the alloy for a tellurium composition from 0 to 100% with temperature from 550K to 1500K. In b) a zoom is given between around 33% and 36.5%, as the phase diagram is particularly complex in this region. First, in a), an eutectic can be observed at 613K for a Te-rich CuTe alloys with compositions ranging from 50 to 100%. It means that for these compositions the increase in temperature will lead to a melt of the alloy, in other words such compositions cannot be used in integrated memories as the memories must resist up to at least 673K (400°C). Then, in b) the numerous phases present in this small range of composition (only 3.5% wide) indicate phase instability in temperature. Therefore, it seems that the composition range showing the best electrical results in the literature, which is Cu_xTe_{1-x} with x between 0.3 and 0.7, in other words between 70 and 30% of tellurium, implies phase instabilities in temperature according to the phase diagram, meaning that this alloy cannot be directly integrated. Therefore, a solution must be proposed in order to stabilize the alloy in temperature.

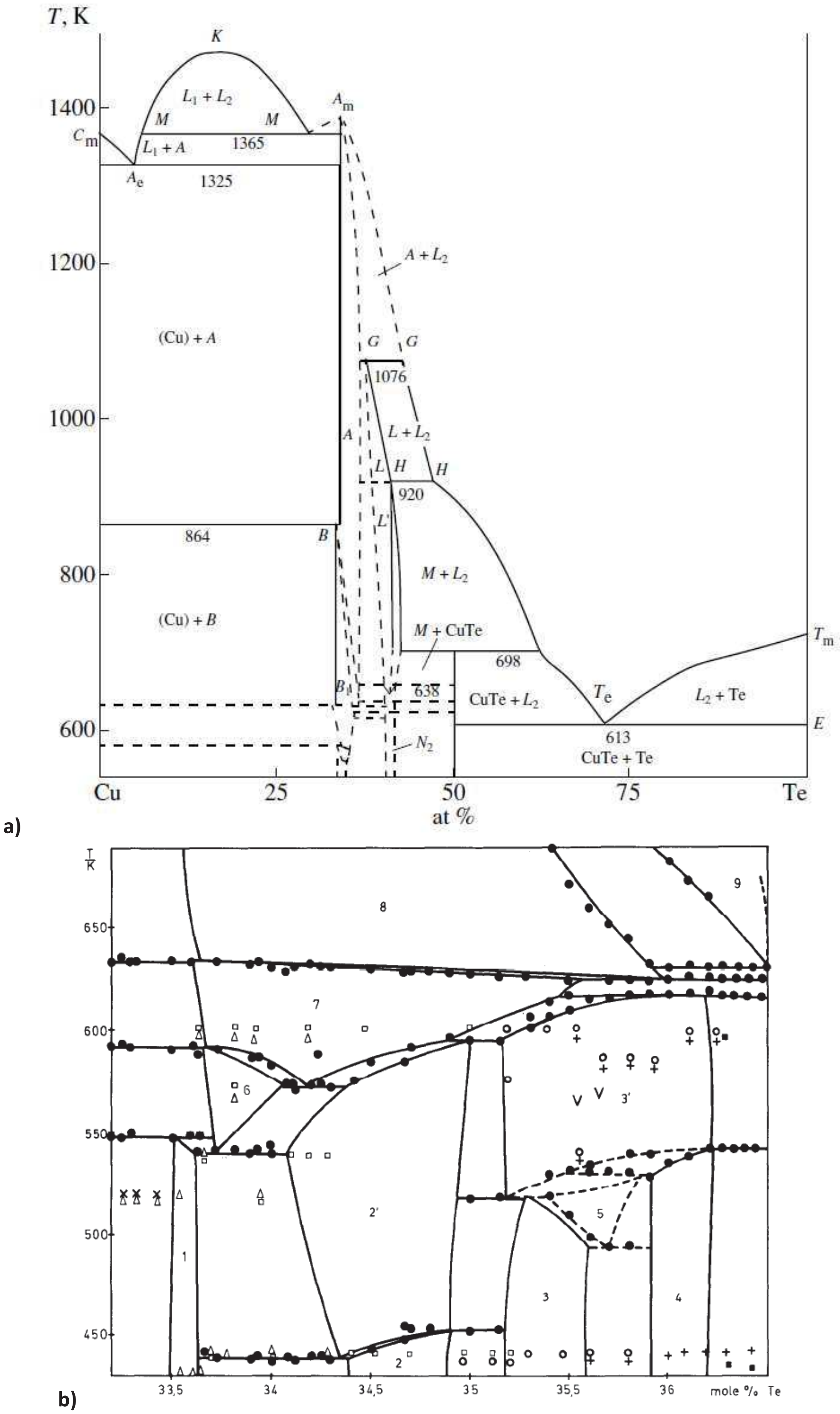

Figure 29: a) Cu-Te phase diagram from [25] and b) detail of the diagram between 33% and 36.5% of tellurium, from [26]

The Figure 30 shows the SEM pictures of Cu_2Te, CuTe and $CuTe_2$ alloys deposited by cosputtering. In the Cu_2Te case in a), the layer is composed of 10-50nm grains. Then, the CuTe sample in b) presents larger grains with a size of approximately 200nm, embedded in a rather smooth material. Finally, the $CuTe_2$ sample in c) has a surface with hillocks of several hundred nanometers wide. Hence, the three compositions of CuTe alloy present an inhomogeneous and rough surface and therefore cannot be used in an integrated memory.

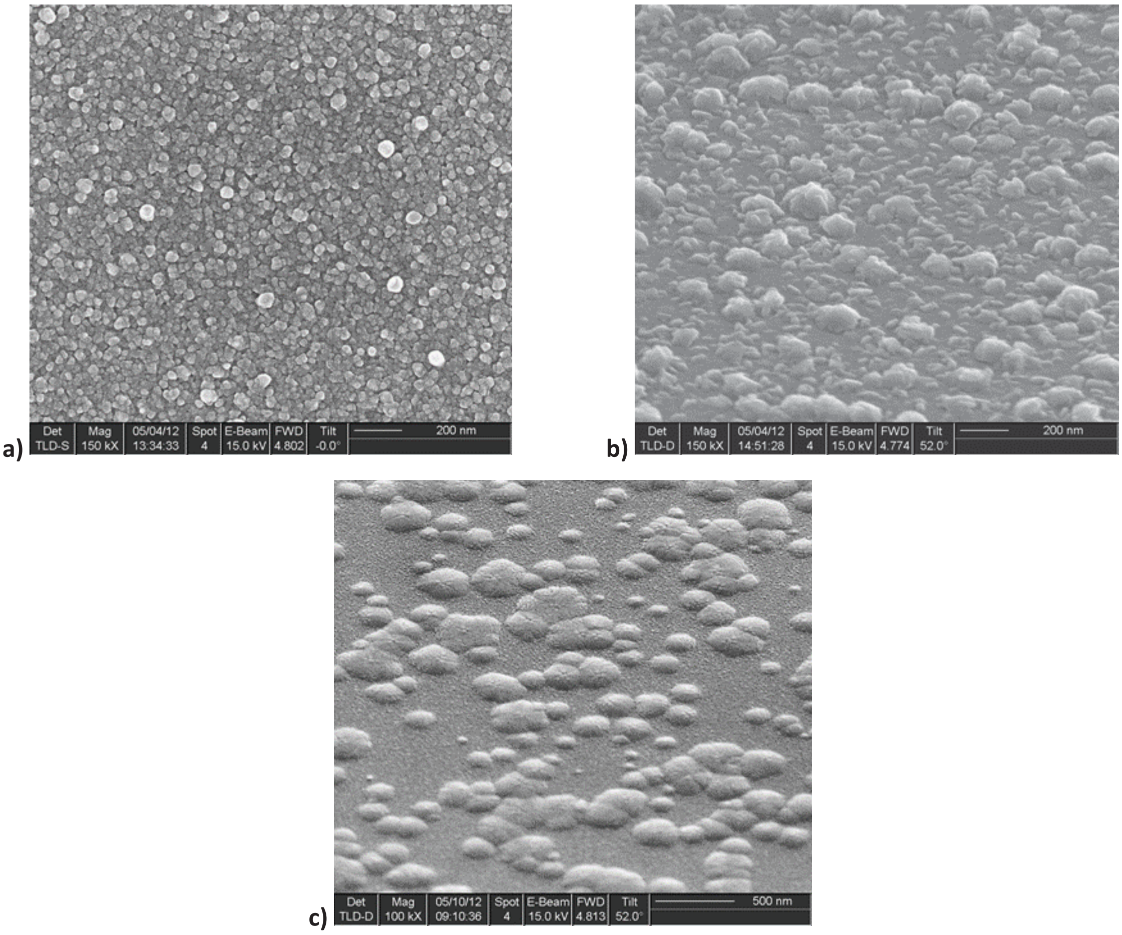

Figure 30: SEM pictures of a Cu_2Te layer in a), a CuTe layer in b) and a $CuTe_2$ layer in c)

Finally, the Figure 31 shows the XRD spectrum of a $Cu_{60}Te_{40}$ layer. The layer is deposited by sputtering of a $Cu_{60}Te_{40}$ target with a power density of 0.6W/cm^2 and an Ar flow of 40sccm. The XRD spectrum presents three peaks: the first, at 12.8° corresponds to hexagonal Cu_2Te (0,0,3) [27], the second at 25° could correspond to hexagonal Cu_2Te (0,0,6) [27] and the last one, at 25.9° to α-TeO_2 (1,1,0) [28]. Therefore, the layer is crystalline with hexagonal Cu_2Te phase. Moreover, the presence of α-TeO_2 seems to indicate an oxidation of the layer, probably due to the exposition to atmosphere.

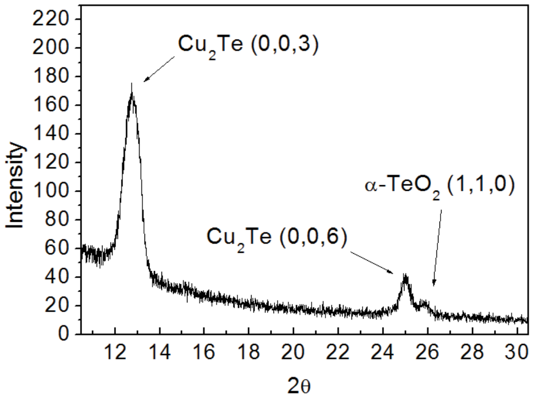

Figure 31: XRD spectra for $Cu_{60}Te_{40}$ sample

To summarize the last three paragraphs, our memory stack does not cycle with pure copper as ion source layers but with a CuTe alloy. However, the alloy phase diagram is complex with many instable phases and shows a lots of phase modifications with the temperature up to 400°C. Moreover, the surface analysis at different stoichiometries shows that the alloy is rough and inhomogeneous. Finally, XRD measurements show that $Cu_{60}Te_{40}$ is crystalline. For all these purposes, the CuTe binary alloy is difficult to integrate in scaled devices where temperature stability is also required. This leads us to consider the amorphization as a solution to integrate such binary alloy. Indeed, an amorphization of the layer, with an increasing of its crystallization temperature, could lead to an improved stability in temperature of the alloy. Also, it also could bring a smooth layer. We decide to use germanium as crystallization inhibitor as this property has been previously observed in literature ([29]-[30]). The amorphization behavior of germanium will be studied in detail in chapter 5.

3.3.1.2. Te-rich $CuTe_2Ge$ ion source layer

For the reference stack we decide to use a Te-rich alloy $CuTe_2Ge$ with 15 atomic% of germanium. Indeed, the literature survey led us to consider that a Te-rich ion source layer is beneficial to reset the memory. A Cu-rich CuTeGe alloy will be also studied and compared with the Te-rich alloy in chapter 5.

To define the ion source layer thickness used in the reference stack, some electrical tests have been performed with 20 or 50nm of $CuTe_2Ge$ in a Ta 200nm/TiN 5nm/Ta_2O_5 10nm/$CuTe_2Ge$/TiN 50nm memory stack, deposited through a shadow mask (technique described in 2.1.2) on a 200mm Si wafer. As the forming voltages obtained do not show an important difference (respectively 1.9(±0.2)V and 1.8(±0.7)V), the ion source layer thickness seems to have no impacts on the memory behaviors in this range of values. To conclude, the reference stack studied in this chapter will have a 20nm ion source layer thickness, however in other chapters thickness could vary between 15 and 50nm, according to the stacks used and the characterizations performed (especially for synchrotron analyses).

The $CuTe_2Ge$ layer is deposited by sputtering of a $CuTe_2$ + Ge 15% target with a power density of $0.6W/cm^2$ and an Ar flow of 40sccm. The composition determined by RBS is presented in Table 2 and shows a composition close to $CuTe_2$, as the target and the results are similar. For convenience this composition is going to be called in this work $CuTe_2Ge$.

	Cu (atomic %) ±2%	**Te (atomic %) ±4%**	**Ge (atomic %) ±1.5%**	**Cu/Te**
Target	28.3	56.6	15	0.50
Deposited layer	28.4	57.9	13.7	0.49

Table 2: $CuTe_2Ge$ composition, expected and obtained

3.3.2. Choice of the electrolyte

The CBRAM memory is an asymmetric MIM stack, where the electrolyte separates two electrodes. The electrolyte first role is to enable the diffusion of copper ions under electrical field. This thesis mainly focuses on metal oxides but chalcogenides glasses, such as $GeSe_x$, GeS_2 or Cu_2S have also been proposed [31].

In order to be used in a CBRAM stack, the dielectric should have some required properties to obtain a memory effect. First, in order to prevent leakage current, the dielectric should have a relatively high band-gap. However, a too high band-gap material affects the global resistivity of the stack. Therefore a thinner dielectric layer may be required, which in turn decreases the breakdown voltage of the dielectric layer. Next, the dielectric should also present some barrier properties against copper diffusion. Indeed, if the copper must diffuse under voltage application, the filament must also be stable when no voltage is applied for the data retention. In other words, the diffusion coefficient of copper in the dielectric should be low enough to prevent the dissolution of the filament in the bulk dielectric. Finally, the material chosen should be compatible with microelectronic processes.

The breakdown voltage could be estimated thanks to the dielectric constant, as presented in Figure 32, which is extracted from the article of J. McPherson *et al.* [32]. According to this paper, the breakdown field E_{Bd} can be estimated from the following equation (10). Then, the breakdown voltage V_{Bd} can be easily calculated thanks to the equation (11), with e the thickness of the layer in cm.

$$E_{Bd}\ (MV.cm^{-1}) = 29.9\ (\kappa)^{-0.65} \tag{10}$$

$$V_{Bd}\ (MV) = E_{Bd} \times e \tag{11}$$

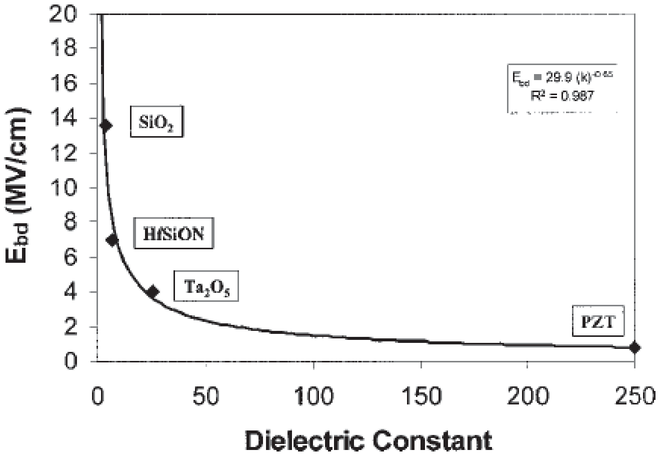

Figure 32: Observed breakdown field versus the dielectric constant in [32]

Therefore the breakdown voltage of the dielectric can be estimated at first approximation thanks to the dielectric constant and the layer thickness. As said in the previous paragraph, the electrolyte should show a compromise between a band-gap not too weak to prevent leakage current and not too high (which would lead to a too thin layer), in order to have a breakdown voltage higher than the voltage necessary to form the filament. Moreover, a copper diffusion barrier behavior is required for the data retention.

The Figure 33 shows the evolution of the band gaps of some oxides with the dielectric constant κ. One can see a relationship between both properties as indicated through the dash line. Among all the dielectrics displayed, Ta_2O_5 seems to be a reasonable choice: it shows an intermediate band gap, together with a dielectric constant relatively high. Looking at Figure 32, it is possible to see that according to literature this dielectric constant corresponds to a breakdown field of around 4MV.cm^{-1}. According to the equation (11), a 10nm thick Ta_2O_5 layer should give a breakdown voltage of 4V. Moreover, the Ta_2O_5 is well known as barrier against copper diffusion ([34]-[35]).

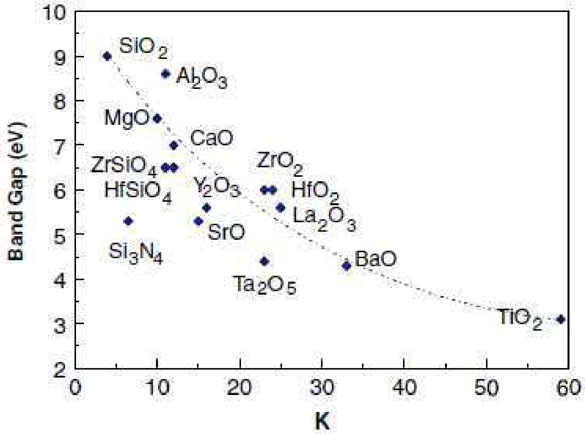

Figure 33: Band gap versus dielectric constant (κ) of several metal oxides, from [33]

Hence, to confirm our assumption, Ta_2O_5 was deposited by DC reactive sputtering of a tantalum target, with Ar at 40sccm, O_2 at 8.1sccm and a power density of 0.7W/cm². To determine its best thickness, four memory stacks were deposited on 200mm Si wafers through a shadow mask (see experimental conditions in 2.1.2), with different dielectric thicknesses, i.e. 5, 7.5, 10 and 12.5nm.

In Figure 34, the forming voltage versus the dielectric thickness was measured in Ta 200nm/Ta_2O_5/$CuTe_2Ge$ 50nm/TaN 50nm stacks. It appears that the forming voltage increases linearly with the thickness until 10nm followed by a plateau at 12.5nm. At 12.5nm, the measurement error is noticeable, which means that it is difficult to distinguish between a linear curve until 12.5nm or saturation with the presence of a plateau. It is supposed that as it is mainly linear, the voltage evolution in function of the thickness could be linked to a field effect. Moreover this measurement error above 10nm implies a lack of repeatability from device to device. Finally, forming values are clearly below 4V, the breakdown voltage expected for a 10nm Ta_2O_5 layer. This highlights the fact that the forming is mainly induced by the contact of $CuTe_2Ge$ on Ta_2O_5, which reduces the required potential to modify the oxide resistivity.

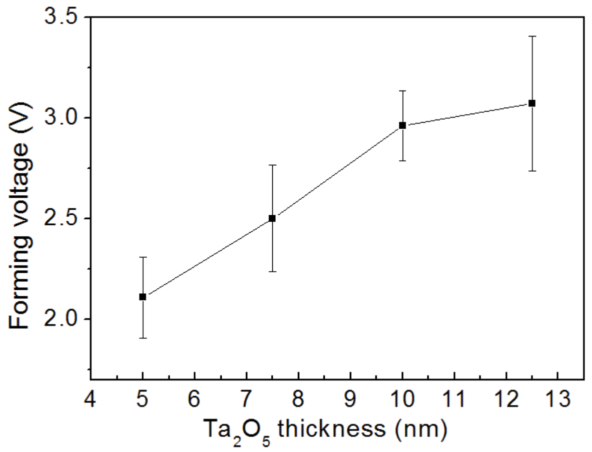

Figure 34: Forming voltage versus the dielectric thickness

3.3.3. Choice of the bottom electrode

The bottom electrode must be electrochemically inert. In other words, it must not react with copper nor oxygen. For this purpose, Pt or other noble metals are an excellent solution. However, such materials are costly and not compatible with CMOS processes [15]. For this purpose, they can be potentially replaced by other materials, such as TiN, Ta, W,…

Titanium nitride is an interesting bottom electrode material as it shows good properties such as high thermodynamic stability, relatively large corrosion resistance and low electrical resistivity ([36]-[38]).

However, one inconvenient of sputtered TiN is its internal mechanical stress, which depends on its deposited thickness. Hence, it is common to measure at least 1GPa of compressive stress in 10nm thick PVD TiN. In order to reduce the internal stress of the layer, nitrogen deficient titanium nitride is generally used. Nevertheless, a non-stoichiometric TiN is known to oxidize at room temperature ([38], [39]). Besides, it is also known that deposition of Ta_2O_5 dielectric on a silicon substrate with an Ar-O_2 plasma creates an interfacial SiO_2 due to the oxidizing atmosphere ([40]-[43]). Therefore, one can expect the oxidation of TiN during the dielectric deposition, as the reactive sputtering implies the use of an Ar-O_2 plasma.

In order to observe if the Ta_2O_5 reactive sputtering deposition has an impact on the TiN bottom electrode, two samples were studied by XPS. The first is a TiN low stress reference sample and the second is a TiN low stress capped with Ta_2O_5 dielectric. The term low stress refers to specific conditions of TiN sputtering process, leading to a TiN layer with a reduced internal stress. Indeed the titanium nitride layers are deposited with a thickness of 5nm on 200mm Si wafers by reactive sputtering of a titanium target, with a power density of 0.7W/cm^2, an Ar flow of 25sccm and a N_2 flow of 35sccm. Then, Ta_2O_5 is deposited, with the same parameters than described in 3.3.2 and a thickness of 2nm, in order to enable TiN XPS analyses through the Ta_2O_5.

Figure 35 shows the Ti$2p_{3/2}$ region of TiN before and after Ta_2O_5 capping. The reference sample spectrum, presented in a), is composed of three contributions positioned at 454.5eV, 456.2eV and 457.9 eV. These contributions have been well reported in the literature and they are respectively identified as TiN, TiON and TiO_2 [44]. Presence of TiON and TiO_2 contributions is related to the oxidation of the TiN bottom electrode, oxidation which is most likely due to the air break between the deposition and the XPS analysis.

In Figure 35 b), the XPS spectrum of the TiN/Ta_2O_5 sample shows a lower intensity compared to the XPS spectrum of the TiN sample. This is due to the TiN layer buried under the Ta_2O_5, implying a strong reduction of the Ti$2p_{3/2}$ signal intensity. However this spectra shows three contributions, the first one at 454.5eV corresponding to a TiN contribution, the second one at 456.5eV to TiON and the last one at 458.1eV to TiO_2. Compared to the TiN spectra in a), in TiN/Ta_2O_5 sample the Ti$2p_{3/2}$ spectra shows a clear higher TiO_2 intensity than TiON and TiN contributions. This increase corresponds to a noticeable oxidation of the TiN layer when Ta_2O_5 is deposited. Therefore, the deposition of Ta_2O_5 by reactive sputtering has oxidized the TiN bottom electrode. Nevertheless, the XPS spectra in Figure 35 b) shows the presence of TiN contribution, which means that the layer is not fully oxidized, the metallic behavior of the electrode seems preserved.

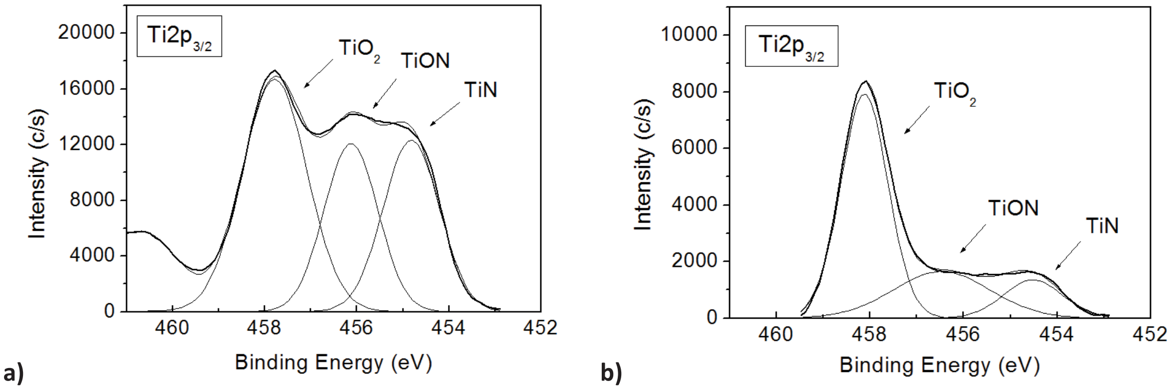

Figure 35: XPS Ti$2p_{3/2}$ of a) the TiN reference sample and b) the TiN/Ta_2O_5 sample

A practical point should also be taken into account in the choice of the bottom electrode: the electrical tests. As it will be described in 3.5, the memory stack will be analyzed by ToF-SIMS. For this purpose, it will be deposited through a shadow mask in order to obtain devices wide enough to be analyzed by ToF-SIMS. Therefore, as presented in 2.2.1, during the electrical tests, one must scratch the dielectric to make the contact with the bottom electrode. However, the thickness scratched is not controlled, therefore it is easy to imagine that the bottom electrode could also be easily scratched. For this purpose, 200nm of Ta is deposited before the TiN. Therefore, the needle probe takes contact with the Ta, which is in direct contact with the TiN of the bottom electrode, as presented in Figure 36.

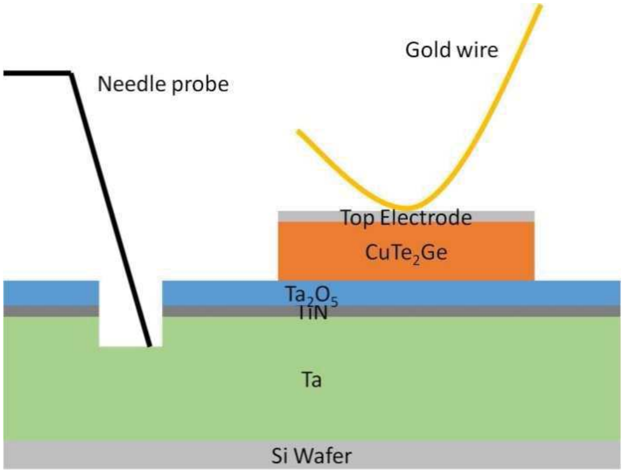

Figure 36: Schematic section of the reference CBRAM device with the electrical assembly

Another solution is to use of the 200nm-Ta as bottom electrode. To test Ta and Ta/TiN differences, two bottom electrodes (called BE in the stack) were electrically tested in a CBRAM configuration with Ta 200nm/TiN 5nm versus pure Ta 200nm as bottom electrode. The BE/Ta_2O_5 10nm/$CuTe_2Ge$ 20nm/TaN 50nm memory stacks were processed on a 200mm Si wafer, using the shadow mask technique (described in 2.1.2).

The electrical tests gave a forming voltage of 3.0(±0.1)V in the case of pure Ta bottom electrode stack and 1.7(±0.2)V for the Ta/TiN bottom electrode stack. This difference of voltage could be due to the difference between titanium and tantalum oxides. Indeed, as the bottom electrode is oxidized during the Ta_2O_5 deposition (as discussed above), use of TiN or Ta as bottom electrode will add to the Ta_2O_5 electrolyte a thin TiO_2 or Ta_2O_5/TaO_x layer, forming a bilayer electrolyte. As Ta_2O_5 and TiO_2 have different dielectric properties, it seems realistic to think that this can also impact the forming values. Another explanation could be that a Ta bottom electrode induces a reduction in copper ion concentration in Ta_2O_5 than a TiN bottom electrode, implying a higher forming voltage [45]. Indeed, as seen in 3.2 Figure 26, the moisture could act as a counter charge in the forming. Thus, this redox reaction of moisture at the bottom electrode, which depends among others on the bottom electrode material, may have an influence on the resulting copper ion concentration, therefore on the forming.

Finally, for the reference stack, the chosen bottom electrode is 200nm-Ta/5nm-TiN, as it shows the lowest forming voltage. However, it is important to keep in mind in the next chapters that bottom electrodes have a noticeable impact on the memory properties.

3.3.4. Choice of the top electrode

In the CBRAM stack the main role of the top electrode is to protect the stack against oxidation due to air break. The top electrode must also be chemically inert, it must not interfere with the memory mechanisms. Finally, it must be conductive and act as a barrier toward oxygen.

TiN or TaN are commonly used as relative inert electrodes in micro-devices or as barrier films. In our case, their good thermal stability, corrosion resistance and low electrical resistivity ([38], [46]) are interesting properties for a top electrode.

In order to check if the nature of the top electrode impacts the memory, both TiN and TaN were studied as Top Electrode (called TE in the stack). The Ta 200nm/TiN 5nm/Ta_2O_5 10m/$CuTe_2Ge$ 20nm/TE 50nm memory stack was deposited on a 200mm silicon wafer using the shadow mask technique (detailed in 2.1.2). The tantalum nitride layer was deposited by reactive sputtering of a tantalum target, with a power density of 5.7W/cm^2, an Ar flow of 40sccm and a N_2 flow of 16sccm. Deposition parameters of the other layers are the same as those described previously.

The electrical tests gave a forming voltage of 1.7(±0.2)V for the stack with TaN and 1.75(±0.7)V for the stack with TiN, thus it seems that the top electrode does not have an impact on the forming at first order. Therefore, for the reference sample it is decided to use the 50nm tantalum nitride as top electrode, deposited with the parameters described above. As no forming voltage differences are noticed between TaN and TiN top electrode, in the next chapters both top electrodes are used depending on the availability of the PVD target in the process equipment.

3.3.5. Reference stack

The reference stack is finally composed of 20nm-$CuTe_2Ge$ ion source layer, 10nm-Ta_2O_5 electrolyte, 200nm-Ta/5nm-TiN bottom electrode and 50nm-TaN top electrode, as explained in the previous sections. The full stack is depicted in Figure 37.

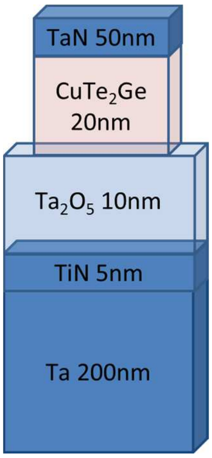

Figure 37: The reference stack

3.4. Electrical tests of the reference stack

Electrical tests of the reference stack are performed with a current compliance of 7mA and a forming voltage of 1.7V. Then the memory is cycled between 1.5V and -1V. Values presented here are averaged on 15 devices. However, only 7 devices are used to determine V_{set} and V_{reset} since some devices are not able to cycle even if they are effectively formed.

The Figure 38 presents the typical I-V characteristics obtained with the stack. The forming and three cycles are displayed. During the forming a sudden current increase is observed around 1.6V and corresponds probably to the formation of a first filament. Then, during the cycles the set voltage seems to be approximately the same, around 0.6V. Additionally, the reset voltage is observed around -0.4V and shows during all the cycles small abrupt current decreases, giving a stair-step shape. According to literature, such decrease could correspond to the formation of a constriction in a conductive filament [9]. Therefore, it could confirm that the conductive phenomenon in the memory stack is based on a filament formation, either CBRAM or OXRAM.

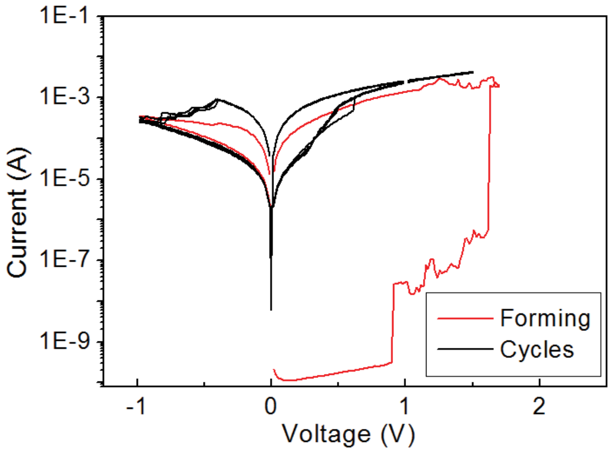

Figure 38: Typical I-V curve obtained with the reference stack

In Table 3, the average results are presented. One can remark that the forming voltage value of 1.7V±0.2 is lower than the 3V forming voltage observed in Figure 34, this difference is obviously due to the difference of bottom electrode as explained in 3.3.3. Then, the 1.7V±0.2 forming voltage is lower than the 4V breakdown voltage, calculated from literature in 3.3.2. Thus, this forming voltage can corresponds to the formation of a metallic filament.

Forming voltage (V)	1.7±0.2
Reset voltage (V)	-0.4±0.1
Set voltage (V)	0.6±0.4

Table 3: Reference stack electrical results

3.5. ToF-SIMS study of the reference stack

The Ta/TiN/Ta_2O_5/$CuTe_2Ge$/TaN nominal stack is in this part analyzed by ToF-SIMS to observe the evolution of chemical species before and after forming. The comparison between before and after forming samples is expected to show the diffusions that may be induced by the applied electrical field.

The stack was realized on a 200mm Si wafer with the shadow mask technique, forming devices of 2mm of diameter. One of them was kept in pristine state (no electrical tests were performed) and a second one was formed by applying an electrical field. These samples are respectively called OFF and ON samples and were studied by ToF-SIMS.

As the stack is composed of many layers, with different materials which could be more or less repelled during sputtering, several parameters of analysis were tuned in order to ease the interfaces identification. Thus profiles were acquired using a Cs^+ sputter gun at a low sputtering energy of 500eV and using two ions detection modes. One mode using Bi^+ ions and the other one Bi^{3+}. Both of these detection modes were achieved at an energy of 25keV, which enable detection of respectively negative and positive ions and are called Negative and MCs modes. Here only MCs mode is presented, but the same behaviors have been observed and confirmed in Negative mode.

3.5.1. ToF-SIMS analyses

3.5.1.1. ON sample forming

Before the ToF-SIMS analyses the forming of the ON sample was performed by ramping up the voltage from 0 to 2.5V with a fixed compliance current at 2x10^{-4}A. The I-V curve obtained is shown in Figure 39. A sudden increase is observed at 1.6V, it corresponds to the formation of the filament.

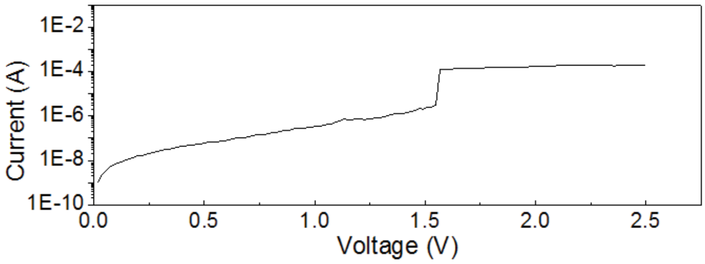

Figure 39: I-V curve obtained during the forming of the ON sample

3.5.1.2. ToF-SIMS results and discussion

The copper, tellurium, tantalum and oxygen profiles in OFF and ON states are visible in Figure 40. Germanium, titanium and nitrogen were also measured but they are not shown here since the germanium signal is too noisy and titanium and nitrogen do not show any variations between OFF and ON states.

The profiles have been first smoothed with an average on 5 points as the raw data were quite noisy. In Figure 40, the Ta bottom electrode is used as reference to shift and align intensity and sputtering time between the samples. In order to ease the interpretation of the profiles, expected positions of the layers are placed on top of the graphs as guides.

In Figure 40, the Ta profiles overlap in the Ta_2O_5 region, therefore the oxide thickness and tantalum concentration seem unchanged after forming. Also the TaN top electrode seems to be thinner in the ON state as the Ta signal is shifted toward longer sputtering times in the TaN region (see arrow (1)). This shift is also observed in the Cu, Te and O profiles around 50s and is visible only because the ON and OFF spectra have been aligned at the bottom electrode. As the devices in ON and OFF states were extracted from the same wafer, thin TaN shrinkage must be explained. First, the electrical connection used during the forming of the ON sample could have load the film and consequently deformed the stack. In that hypothesis, it could be possible that the TaN layer absorbs a part of the mechanical load as the shift at the surface is more important than the one at the interface with the ion source layer (arrow (2)). However, the gold wire has a diameter of 500µm, which means that its contact surface is much lower than the area analyzed by the ToF-SIMS, which has 300µm of diameter. Another explanation could be the uniformity of the deposition. However, sheet resistance measurements performed on a 50nm TaN layer gives a maximum difference of 3nm between two points of the sample, thus an error of 6%. However, the shift (see arrow (1)) corresponds to around 15% of the expected 50nm TaN top electrode, which is much larger than the error observed with the single 50nm TaN layer. Finally, a last explanation could be a shadow effect, induced by the mask during the stack deposition. Indeed, the shadow effect may induce a non-uniformity of the ion source/top electrode layers. Actually, OFF and ON samples have not been analyzed exactly at the same position on the area of 2mm diameter of the device. It is possible that this shadow effect is enough to induce an important difference of thickness, observable by ToF-SIMS when moving slightly the position of the ToF-SIMS guns.

One can remark that Cu and Te ON profiles show a shift toward longer sputtering times (arrows (3) and (4)), which is observed at the $CuTe_2Ge$/TaN interface. Thus these shifts seem to be due to the same artifact than the TaN thickness evolution. Nevertheless, it is important to remark that contrary to what is expected for a CBRAM, copper is not observed to diffuse toward the bottom electrode after forming, which seems incoherent with the electrochemical formation of a copper conductive filament. This point is discussed below.

Finally, OFF and ON oxygen ToF-SIMS profiles overlap, which make sense since Ta_2O_5 was deposited prior to cell masking and subsequent shadow effect. Therefore oxygen seems to not participate to the forming mechanisms.

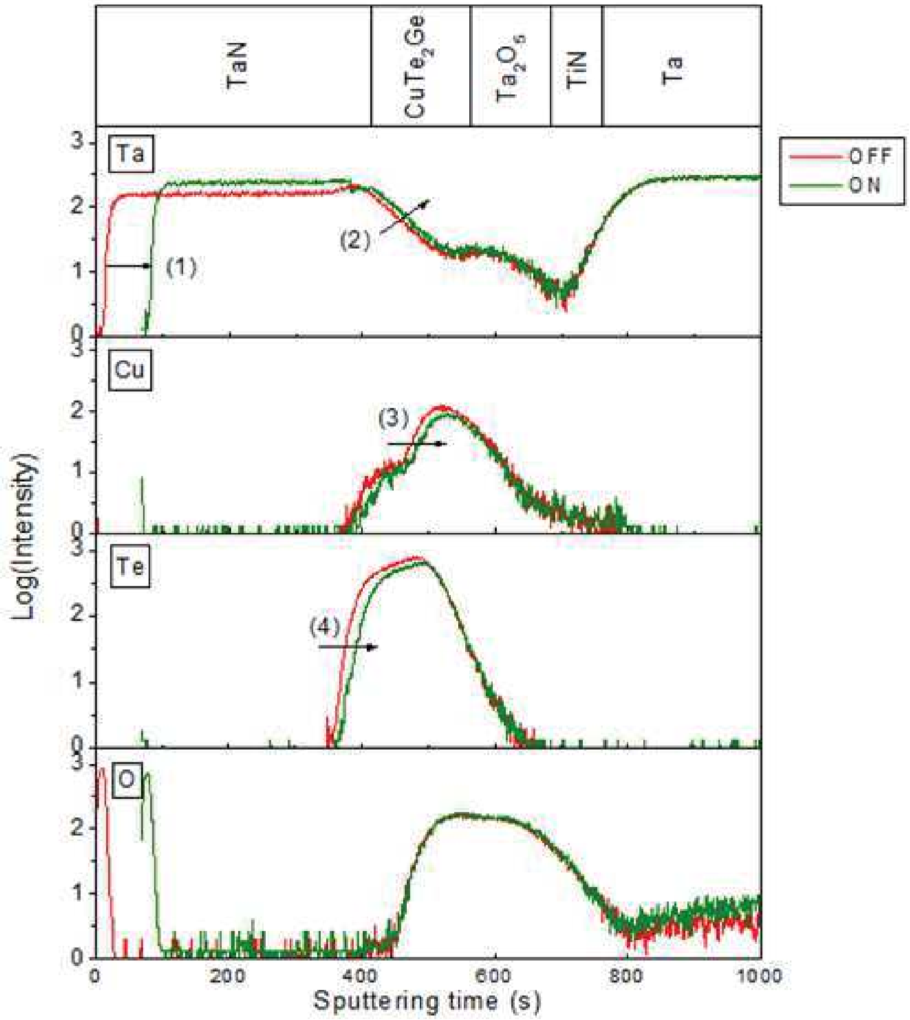

Figure 40: Ta, Cu, Te and O ToF-SIMS profiles of OFF and ON states (i.e. before and after forming)

As observed in the previous part, even if a forming is measured electrically (see Figure 39), the stack does not show any detectable diffusions by ToF-SIMS after the forming even if the analyses have been performed just after the forming, thus when the filament is normally not dissolved by ageing.

ToF-SIMS analysis was chosen since it appeared as the main adapted characterization method to address such complex stack. In the present case, one would object that this method is not adapted for the purpose, namely try to determine the position of diffused atoms induced by the electrical field in a localized region (in term of lateral dimension), i.e. the filament area. However, we assume that the diffusions supposed to take place in CBRAM forming could be observed by ToF-SIMS, since prior to forming one could expect a collective movement of copper in the dielectric until only one filament is finally locally formed leading to a short circuit. We do not see any collective movement here but we will see in fact such diffusion signatures in the next chapters.

Therefore, this absence of diffusion while a forming step is observed enables us to think that the phenomenon linked to the forming is local and not global. We can try to explain this phenomenon by the known differences between CBRAM and OXRAM. A CBRAM is different from an OXRAM in the sense of the nature of the conductive bridge formed in the dielectric. It is admitted that in the case of a CBRAM, the bridge is composed of metallic cations moving into the dielectric. In the case of OXRAM, it is formed internally in the dielectric, through the movement of oxygen from inside toward outside the dielectric leading to a path of vacancies (in other words, a bridge of metallic atoms of the dielectric). Nevertheless, in the case of OXRAM the forming is presumed to correspond to a local movement of oxygen, also viewed as a “soft dielectric” breakdown [50].

Here it is interesting to notice that despite the presence of copper in the ion source layer, the reference stack is similar to an OXRAM stack. Indeed CBRAM and OXRAM stacks are quite close, the only difference are the materials used, which enable the formation of a conductive filament composed of metal atoms or of oxygen vacancies. Additionally, the Ta_2O_5 used in the reference stack could also be used in OXRAM ([47]-[49]), contrary to other types of dielectrics used in CBRAM such as SiO_2 (see 3.2).

ToF-SIMS results do not show a global diffusion even if a forming is observed. Moreover the stack is similar to an OXRAM stack, with an electrolyte which could be used both in CBRAM and OXRAM memories. Therefore, an explanation to this absence of global diffusion could be an OXRAM forming.

If the memory behaves as an OXRAM, this is obviously surprising as copper in the stack was expected to induce a CBRAM-like behavior (through Cu cations movements). It would mean that the electric breakdown of the dielectric has occurred before the copper ions diffusion when ramping up the external potential, as already been observed in literature [51]. In other words, the OXRAM behavior is obtained if the potential needed to form the metallic filament is higher than the electric breakdown voltage of the dielectric.

Several reasons could explain the potential presence of an OXRAM behavior in the reference stack. A first reason is linked to the electrical properties of the dielectric, in particular the electrical gap and the dielectric constant. Indeed, the breakdown voltage is dependent of the layer thickness and of its dielectric constant (see 3.3.2). If the dielectric constant is too important or if the thickness is too small, the oxide may break easily under electrical field, thus facilitating an OXRAM behavior. Another reason implies the diffusion property of a given element in the dielectric, namely the barrier properties against diffusion. Tantalum and its oxide are known as a good barrier against copper diffusion. It is possible that the Ta_2O_5 is a barrier against copper diffusion and is well efficient regarding this diffusion, requiring a high voltage to drift copper ions. In the next chapters we will see that a modification of the dielectric or of the ion source layer will lead to a change of the type of forming obtained.

3.6. Conclusions

In this chapter, after a short state of the art on the study of CBRAM forming mechanisms, the detailed choice of a CBRAM memory stack is achieved according to the literature and internal knowledges. Then the stack is deposited and analyzed before and after forming by ToF-SIMS in order to assess the chemical species movements induced by the forming.

Surprisingly, the ToF-SIMS results do not present any diffusion in the stack, even if a forming is achieved. Therefore an OXRAM behavior is suspected. It seems that such a forming could take place in the CBRAM memory if the OXRAM forming voltage is lower than the voltage required to form the metallic filament. Another explanation could be the copper diffusion barrier properties of the dielectric, which can be too high to enable the formation of the metallic filament under electrical field. Therefore, the frontier between CBRAM and OXRAM seems tight and depends on the properties of the electrolyte and the ion source layer.

Thus questions are raised on the real impact of each layer on the forming mechanisms. Which properties are needed to reach a CBRAM-like behavior? What is the impact of the dielectric or the ion source layer on the forming? If OXRAM mechanisms could be obtained with copper in the stack, does a CBRAM behavior could also be obtained without Cu or Ag in the stack? What is the role of oxygen? What is the role of tellurium, and why a chalcogenide alloy is required for the ion source layer? How a hybrid CBRAM/OXRAM memory could be obtained?

We are going to try to apprehend some of these items in next chapters, through material modifications. For this purpose this reference stack will be modified step by step, in order to observe the effects on the forming. First, we will try to modify the dielectric through deposition of a thin oxygen getter such as pure titanium in the next chapter. Then, the dielectric will be changed using a lower Gibbs free energy dielectric and finally in the last chapter the impact of the ion source layer will be studied.

3.7. Bibliography

[1] R. Waser, R. Dittmann, G. Staikov, and K. Szot, “Redox-Based Resistive Switching Memories - Nanoionic Mechanisms, Prospects, and Challenges”, Advanced Materials, vol. 21, no. 25–26, pp. 2632–2663, 2009.

[2] Y. Li, S. Long, Q. Liu, H. Lü, S. Liu, and M. Liu, “An overview of resistive random access memory devices”, Chinese Science Bulletin, vol. 56, no. 28–29, pp. 3072–3078, 2011.

[3] P. A. N. Feng, C. Chao, Z. Wang, Y. Yang, Y. Jing, and Z. Fei, “Nonvolatile resistive switching memories-characteristics, mechanisms and challenges”, Progress in Natural Science: Materials International, vol. 20, pp. 1–15, 2010.

[4] I. Valov and M. N. Kozicki, “Cation-based resistance change memory”, Journal of Physics D: Applied Physics, vol. 46, no. 7, p. 074005, 2013.

[5] I. Valov, R. Waser, J. R. Jameson, and M. N. Kozicki, “Electrochemical metallization memories—fundamentals, applications, prospects”, Nanotechnology, vol. 22, no. 28, p. 289502, 2011.

[6] M. Tada, T. Sakamoto, N. Banno, K. Okamoto, N. Iguchi, H. Hada, and M. Miyamura, “Improved ON-State Reliability of Atom Switch Using Alloy Electrodes”, IEEE Transactions on Electron Devices, vol. 60, no. 10, pp. 3534–3540, 2013.

[7] L. Goux, K. Opsomer, R. Degraeve, R. Müller, C. Detavernier, D. J. Wouters, M. Jurczak, L. Altimime, and J. A. Kittl, “Influence of the Cu-Te composition and microstructure on the resistive switching of Cu-Te/Al_2O_3/Si cells”, Applied Physics Letters, vol. 99, no. 5, p. 053502, 2011.

[8] T. Tsuruoka, K. Terabe, T. Hasegawa, and M. Aono, “Temperature effects on the switching kinetics of a Cu-Ta_2O_5-based atomic switch”, Nanotechnology, vol. 22, no. 25, p. 254013, 2011.

[9] S. Blonkowski and T. Cabout, “Bipolar resistive switching from liquid helium to room temperature”, Journal of Physics D: Applied Physics, vol. 48, no. 34, p. 345101, 2015.

[10] D.-Y. Cho, S. Tappertzhofen, R. Waser, and I. Valov, “Bond nature of active metal ions in SiO_2-based electrochemical metallization memory cells”, Nanoscale, vol. 5, no. 5, p. 1781, 2013.

[11] T. Tsuruoka, K. Terabe, T. Hasegawa, I. Valov, R. Waser, and M. Aono, “Effects of Moisture on the Switching Characteristics of Oxide-Based, Gapless-Type Atomic Switches”, Advanced Functional Materials, vol. 22, no. 1, pp. 70–77, 2012.

[12] S. Tappertzhofen, I. Valov, T. Tsuruoka, T. Hasegawa, R. Waser, and M. Aono, “Generic Relevance of Counter Charges for Cation-Based Nanoscale Resistive Switching Memories”, ACS Nano, vol. 7, no. 7, pp. 6396–6402, 2013.

[13] L. Yang, C. Kuegeler, K. Szot, A. Ruediger, and R. Waser, “The influence of copper top electrodes on the resistive switching effect in TiO_2 thin films studied by conductive atomic force microscopy”, Applied Physics Letters, vol. 95, no. 1, p. 013109, 2009.

[14] Y. Kang, M. Verma, T. Potnis, T. Liu, and M. Orlowski, “Conditions for Formation and Rupture of Multiple Conductive Cu and V_O Filaments in a Cu/TaO_x/Pt Device”, ECS Transactions, vol. 50, no. 34, pp. 19–24, 2013.

[15] H. Jeon, J. Park, W. Jang, H. Kim, H. Song, H. Kim, H. Seo, and H. Jeon, “Resistive switching behaviors of Cu/TaO_x/TiN device with combined oxygen vacancy/copper conductive filaments”, Current Applied Physics, vol. 15, no. 9, pp. 1005–1009, 2015.

[16] A. Wedig, M. Luebben, D.-Y. Cho, M. Moors, K. Skaja, V. Rana, T. Hasegawa, K. K. Adepalli, B. Yildiz, R. Waser, and I. Valov, “Nanoscale cation motion in TaO_x, HfO_x and TiO_x memristive systems”, Nature Nanotechnology, 2015.

[17] T. Nagata, M. Haemori, Y. Yamashita, H. Yoshikawa, Y. Iwashita, K. Kobayashi, and T. Chikyow, “Bias application hard x-ray photoelectron spectroscopy study of forming process of Cu/HfO_2/Pt resistive random access memory structure”, Applied Physics Letters, vol. 99, no. 22, p. 223517, 2011.

[18] M. Kudo, M. Arita, Y. Ohno, and Y. Takahashi, “Filament formation and erasure in molybdenum oxide during resistive switching cycles”, Applied Physics Letters, vol. 105, no. 17, p. 173504, 2014.

[19] S. Tappertzhofen, H. Mündelein, I. Valov, and R. Waser, “Nanoionic transport and electrochemical reactions in resistively switching silicon dioxide”, Nanoscale, vol. 4, no. 10, p. 3040, 2012.

[20] Q. Liu, J. Sun, H. Lv, S. Long, K. Yin, N. Wan, Y. Li, L. Sun, and M. Liu, “Real-Time Observation on Dynamic Growth/Dissolution of Conductive Filaments in Oxide-Electrolyte-Based ReRAM”, Advanced Materials, vol. 24, no. 14, pp. 1844–1849, 2012.

[21] L. Goux, K. Opsomer, R. Schuitema, R. Degraeve, R. Muller, C. Detavernier, D. J. Wouters, M. Jurczak, L. Altimime, and J. A. Kittl, “Self-Limited Filament Formation and Low-Power Resistive Switching in Cu_xTe_{1-x}/Al_2O_3/Si CBRAM Cell”, in 2011 3rd IEEE International Memory Workshop (IMW), pp. 1–4, 2011.

[22] K. Aratani, K. Ohba, T. Mizuguchi, S. Yasuda, T. Shiimoto, T. Tsushima, T. Sone, K. Endo, A. Kouchiyama, S. Sasaki, A. Maesaka, N. Yamada and H. Narisawa, “A novel resistance memory with

high scalability and nanosecond switching", in 2007 IEEE International Electron Devices Meeting (IEDM), pp. 783–786, 2007.

[23]M. Kudo, M. Arita, Y. Takahashi, K. Ohba, M. Shimuta, and I. Fujiwara, "Visualization of conductive filament during write and erase cycles on nanometer-scale ReRAM achieved by in-situ TEM", in 2015 IEEE 7th International Memory Workshop (IMW), p. 85, 2015.

[24]W. Devulder, K. Opsomer, G. Rampelberg, B. De Schutter, K. Devloo-Casier, M. Jurczak, L. Goux, and C. Detavernier, "Improved thermal stability and retention properties of Cu–Te based CBRAM by Ge alloying", J. Mater. Chem. C, vol. 3, no. 48, pp. 12469–12476, 2015.

[25]A. S. Pashinkin and L. M. Pavlova, "pT phase diagram of the Cu-Te system", Inorganic materials, vol. 41, no. 9, pp. 939–944, 2005.

[26]R. Blachnik, M. Lasocka, and U. Walbrecht, "The System Copper-Tellurium", Journal of Solid State Chemistry, vol. 48, pp. 431–438, 1983.

[27]H. Ghoumari-Bouanani, G. Brun, B. Liautard, J. Tedenac, "Equilibres de phases dans le système tellurure de cuivre, tellurure de bismuth", Material Research Bulletin, 28, 901, 1993.

[28]P. A. Thomas, "The crystal structure and absolute optical chirality of paratellurite, α-TeO_2", J. Phys. C: Solid State Phys., 21, 4611, 1988.

[29]J. Yu, B. Liu, T. Zhang, Z. Song, S. Feng, and B. Chen, "Effects of Ge doping on the properties of Sb_2Te_3 phase-change thin films", Applied Surface Science, vol. 253, no. 14, pp. 6125–6129, 2007.

[30]L. van Pieterson, M. H. R. Lankhorst, M. van Schijndel, A. E. T. Kuiper, and J. H. J. Roosen, "Phase-change recording materials with a growth-dominated crystallization mechanism: A materials overview", Journal of Applied Physics, vol. 97, no. 8, p. 083520, 2005.

[31]D. Jana, S. Roy, R. Panja, M. Dutta, S. Z. Rahaman, R. Mahapatra, and S. Maikap, "Conductive-bridging random access memory: challenges and opportunity for 3D architecture", Nanoscale Research Letters, vol. 10, no. 1, 2015.

[32]J. McPherson, J.-Y. Kim, A. Shanware, and H. Mogul, "Thermochemical description of dielectric breakdown in high dielectric constant materials", Applied Physics Letters, vol. 82, no. 13, p. 2121, 2003.

[33]J. Robertson, "High dielectric constant gate oxides for metal oxide Si transistors", Reports on Progress in Physics, vol. 69, no. 2, pp. 327–396, 2006.

[34]P. Alén, M. Vehkamäki, M. Ritala, and M. Leskelä, "Diffusion Barrier Properties of Atomic Layer Deposited Ultrathin Ta_2O_5 and TiO_2 Films", Journal of The Electrochemical Society, vol. 153, no. 4, p. G304, 2006.

[35]A. L. Salaün, A. Mantoux, E. Blanquet, and E. Djurado, "ESD and ALD Depositions of Ta_2O_5 Thin Films Investigated as Barriers to Copper Diffusion for Advanced Metallization", Journal of The Electrochemical Society, vol. 156, no. 5, p. H311, 2009.

[36]I. Milošv, H.-H. Strehblow, B. Navinšek, and M. Metikoš-Huković, "Electrochemical and thermal oxidation of TiN coatings studied by XPS", Surface and interface analysis, vol. 23, no. 7–8, pp. 529–539, 1995.

[37]H.-Y. Chen and F.-H. Lu, "Oxidation behavior of titanium nitride films", Journal of Vacuum Science & Technology A: Vacuum, Surfaces, and Films, vol. 23, no. 4, p. 1006, 2005.

[38]A. W. Groenland, I. Brunets, A. Boogaard, A. A. I. Aarnink, A. Y. Kovalgin, and J. Schmitz, "Thermal and plasma-enhanced oxidation of ALD TiN", 2008.

[39]S. Logothetidis, E. I. Meletis, G. Stergioudis, and A. A. Adjaottor, "Room temperature oxidation behavior of TiN thin films", Thin Solid Films, vol. 338, pp. 304–313, 1999.

[40]C. Chaneliere, J.L. Autran, R.A.B. Devine, and B. Balland, “Tantalum pentoxide (Ta_2O_5) thin films for advanced dielectric applications”, Materials Science and Engineering, vol. R22, pp. 269–322, 1998.

[41]R. A. B. Devine, “Nondestructive measurement of interfacial SiO_2 films formed during deposition and annealing of Ta_2O_5”, Applied Physics Letters, vol. 68, no. 14, p. 1924, 1996.

[42]Nagahori and R. Raj, “Electron Cyclotron Resonance Plasma-Enhanced Metalorganic Chemical Vapor Deposition of Tantalum Oxide Thin Films on Silicon near Room Temperature”, Journal of the American Ceramic Society, vol. 78, no. 6, pp. 1585, 1995.

[43]T. Dimitrova and E. Atanassova, “Electrical and transport properties of RF sputtered Ta_2O_5 on Si”, Solid-State Electronics, vol. 42, no. 3, p. 307, 1998.

[44]Y. Cheng and Y. F. Zheng, “Surface characterization and mechanical property of TiN/Ti-coated NiTi alloy by PIIID”, Surface and Coatings Technology, vol. 201, no. 15, pp. 6869–6873, 2007.

[45]S. Tappertzhofen, R. Waser, and I. Valov, “Impact of the Counter-Electrode Material on Redox Processes in Resistive Switching Memories”, ChemElectroChem, vol. 1, no. 8, pp. 1287–1292, 2014.

[46]D. Kim, H. Lee, D. Kim, and Y. Keun Kim, “Electrical and mechanical properties of tantalum nitride thin films deposited by reactive sputtering”, Journal of Crystal Growth, vol. 283, no. 3–4, pp. 404–408, 2005.

[47]J. Yang-Scharlotta, M. Fazio, M. Amrbar, M. White, and D. Sheldon, “Reliability characterization of a commercial TaO_x-based ReRAM”, in 2014 IEEE International Integrated Reliability Workshop Final Report (IIRW), pp. 131–134, 2014.

[48]Y. Hayakawa, A. Himeno, R. Yasuhara, W. Boullart, E. Vecchio, T. Vandeweyer, T. Witters, D. Crotti, M. Jurczak, S. Fujii, and others, “Highly reliable TaO_x ReRAM with centralized filament for 28-nm embedded application”, in 2015 Symposium on VLSI Technology, pp. T14–T15, 2015.

[49]M.-J. Lee, C. B. Lee, D. Lee, S. R. Lee, M. Chang, J. H. Hur, Y.-B. Kim, C.-J. Kim, D. H. Seo, S. Seo, U.-I. Chung, I.-K. Yoo, and K. Kim, “A fast, high-endurance and scalable non-volatile memory device made from asymmetric Ta_2O_{5-x}/TaO_{2-x} bilayer structures”, Nature Materials, vol. 10, no. 8, pp. 625–630, 2011.

[50]N. Xu, L. Liu, X. Sun, X. Liu, D. Han, Y. Wang, R. Han, J. Kang, and B. Yu, “Characteristics and mechanism of conduction/set process in TiN/ZnO/Pt resistance switching random-access memories”, Applied Physics Letters, vol. 92, no. 23, p. 232112, 2008.

[51]M. Saadi, P. Gonon, C. Vallée, C. Mannequin, H. Grampeix, E. Jalaguier, F. Jomni, and A. Bsiesy, “On the mechanisms of cation injection in conducting bridge memories: The case of HfO_2 in contact with noble metal anodes (Au, Cu, Ag)”, Journal of Applied Physics, vol. 119, no. 11, p. 114501, 2016.

Chapter 4: Impact of the dielectric on the forming mechanisms

4.1. Introduction

In the previous chapter a reference stack Ta/TiN/Ta_2O_5/$CuTe_2Ge$/TaN was studied by ToF-SIMS. The results bring us to suspect an OXRAM behavior based on the movement of oxygen, leading to a so called soft breakdown ([1]-[3]). We assume that it is due to the breakdown voltage of the dielectric Ta_2O_5 which could be lower than the voltage needed to diffuse copper ions through the dielectric. Thus, when applying a voltage ramp to write the memory, a “soft breakdown” voltage is reached prior to the potential required for copper diffusion. Therefore, an OXRAM forming appears before the expected CBRAM forming. It is suspected that different types of forming mechanisms could be obtained by modifying the stack, more precisely by modifying the dielectric and the ion source layer.

For example, an increase of the dielectric breakdown voltage could enable a CBRAM behavior if it became higher than the voltage required to diffuse copper ions. This increase of the strength of the dielectric against external potential could be performed by changing the Ta_2O_5 by a material with a higher breakdown field. Another kind of modification of the electrolyte, which is expected to modify the type of forming obtained, relies on the initial amount of vacancies in the dielectric and its ability to form vacancies. Indeed the diffusion of copper is known to be principally driven by the defects present in the layer [4]. Thus, oxygen vacancies in a metal oxide, which are defects, are expected to ease the diffusion of copper ions in the dielectric. Therefore, the voltage required for the copper ion diffusion should decrease.

In this chapter, a focus is given on the study of the impact of oxygen reduction in the solid electrolyte on the forming mechanisms. The importance of the role of oxygen and more precisely of the Ta-O bond strength will be assessed. This will conduct us to study in a second part the impact of the standard Gibbs free energy of the oxide on the forming mechanisms, which could be seen as the M-O bond strength in a MO_x metal oxide.

4.2. Ta_2O_5 reduction by oxygen scavenging

4.2.1. Introduction

As discussed above in 4.1, the oxygen reduction of Ta_2O_5 is expected to improve copper diffusion as oxygen vacancies present in reduced tantalum oxide are supposed to be a preferential path for copper diffusion. Thus, the voltage required to induce copper ions movement through the dielectric should be less important.

To reduce the oxygen level in the tantalum pentoxide, two ways are possible. The first one consists in directly depositing a tantalum sub-oxide, which is possible by reactive sputtering of pure tantalum with an adjustment of the oxygen flow. However, due to the low oxygen partial pressure required to reach the right stoichiometry, this method induces reproducibility issues. The second way consists in the addition of a layer which reacts with the tantalum pentoxide and reduces it, in other words which scavenges the oxygen of the dielectric. This last solution is finally chosen, because this interlayer also modifies the properties of the ion source layer/dielectric interface, which could enable a "control" of the copper ion injection in the dielectric ([5], [6]). Indeed, as discussed in 3.2 with the Figure 25, copper ions need to pass through the ion source layer/dielectric interface before the diffusion toward the bottom electrode.

Addition of a buffer layer in RRAM stacks has been already studied in literature ([5]-[10]). One can particularly mention the work of S. Z. Rahaman *et al.* [6], where they studied the deposition of titanium on tantalum oxide. For this purpose, they inserted a titanium interlayer, also called buffer layer, in a W/TaO_x/Cu/Al memory stack. XPS measurements indicated that obviously the stack became a W/deoxidized TaO_x/TiO_2/Cu/Al stack. S. Z. Rahaman *et al.* showed that this is due to the lower standard Gibbs free energy of TiO_2 compared to Ta_2O_5 (respectively -889.5 and -760.75 kJ/mol at 300K [6]). Thus the Ti interlayer scavenges the oxygen of the Ta_2O_5 layer according to the following reaction (12):

$$\mathrm{Ti} + \frac{2}{5}\,\mathrm{Ta_2O_5} \rightarrow \mathrm{TiO_2} + \frac{4}{5}\,\mathrm{Ta} \tag{12}$$

This reaction implies an increase of the global insulating thickness through the TaO_x/TiO_2 formation. Moreover, oxygen vacancies are formed in the dielectric as the oxygen of Ta_2O_5 has been scavenged by the titanium. In consequence, S. Z. Rahaman observed an improvement of the memory properties such as wider resistances ratio, better endurance and data retention. This appears to be due to the thickening of the dielectric, which implies a higher resistance in OFF state, thus a wider resistance ratio. Moreover, the TiO_2 acts as a barrier for copper diffusion and thus retains copper in the Ta_2O_5, which in turn improves the data retention.

As the addition of titanium between the ion source layer and the dielectric of a CBRAM memory stack seems to improve its properties, titanium seems to be a good candidate for reducing oxygen in Ta_2O_5 in the reference stack described in 3.3.5. However, such reduction could also be obtained with other materials such as aluminum for example.

Figure 41 shows the Ellingham diagram of Ta, Ti and Al metals and oxygen. The Ellingham diagram presents the thermal evolution of the standard Gibbs free energy of the reactions of some metals (Ta, Ti and Al) with 1 mole of O_2. One can see that TiO_2 has a lower standard Gibbs free energy than Ta_2O_5 as already observed in the paper of S. Z. Rahaman *et al.* [6]. However, it appears that Al_2O_3 has a standard Gibbs free energy even lower than Ta_2O_5 or TiO_2, enabling the following reactions (13) and (14) (reaction (13) is also reported in Figure 41):

$$\frac{4}{3}\,\mathrm{Al} + \frac{2}{5}\,\mathrm{Ta_2O_5} \rightarrow \frac{4}{5}\,\mathrm{Ta} + \frac{2}{3}\,\mathrm{Al_2O_3} \tag{13}$$

$$\frac{4}{3}\,\mathrm{Al} + \mathrm{TiO_2} \rightarrow \mathrm{Ti} + \frac{2}{3}\mathrm{Al_2O_3} \tag{14}$$

Thus, both aluminum and titanium can reduce the tantalum oxide. Moreover, alumina and titanium oxides are known for their copper diffusion barrier behavior (respectively [11]-[14] and [6], [15]). It means that both will have an impact on the injection of copper ions during the forming, but also on the retention of the filament in the dielectric if Al_2O_3 or TiO_2 are positioned between the Ta_2O_5 dielectric and the ion source layer. Therefore, both alumina and titanium oxide could be used as interlayer between the Ta_2O_5 and the ion source layer in the CBRAM memory stack. Nevertheless, as described by the reaction (14), the aluminum can also reduce the titanium oxide. As a reminder, the reference stack described in Chapter 3 has a Ta/TiN bottom electrode. Moreover, in 3.3.3 Figure 35 and associated paragraphs, it is observed that the TiN layer of the bottom electrode is partially oxidized during the Ta_2O_5 deposition. Therefore, when using aluminum interlayer on the Ta_2O_5, it seems possible that the oxygen content of the oxidized titanium nitride is also reduced.

Hence in the next parts the impact of Al and Ti interlayers on the TiN/Ta_2O_5-based reference memory stack are studied through material characterizations and electrical tests.

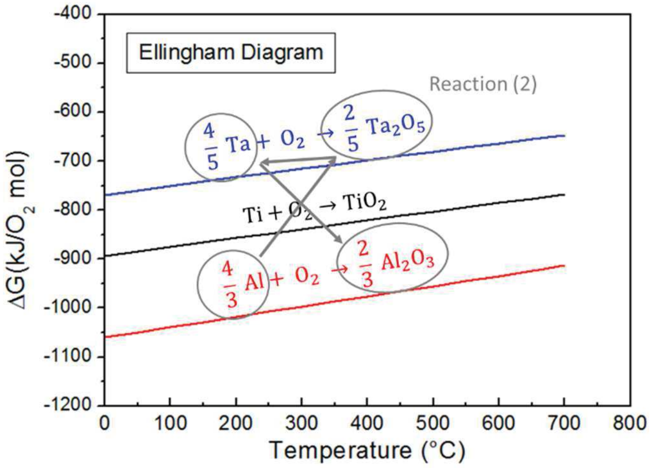

Figure 41: Ellingham diagram

4.2.2. Effect of the insertion of a metal scavenger on the memory layers

4.2.2.1. Studied samples

To study the impact of interlayers insertion on the oxides present in the stack, TiN/Ta_2O_5-based samples were used and Ti or Al interlayers were deposited on the top. In the work of S. Z. Rahaman *et al.* [6] discussed previously, thin TiO_2 layers of 3nm were used in order to enable the copper diffusion under electrical field and to reduce 18nm of TaO_x. Here similar thicknesses of about 1nm were used to enable copper diffusion under electrical field and reduce the 10nm of Ta_2O_5.

The 5nm TiN bottom electrode was deposited on 200mm Si wafers by sputtering (see 3.3), followed by Ta_2O_5 dielectric deposition by reactive sputtering of a Ta target. In this study, 5nm tantalum oxide was deposited instead of 10nm as in the reference, in order to enable the analysis of the bottom electrode by XPS as the depth analyzed is limited to about 5-8nm (see 2.2.2.1). Finally the interlayer was deposited. As discussed in the previous part, Ti and Al were chosen as oxygen scavenger. They were deposited by sputtering of pure Al or Ti target with a low power density ($2x10^{-2}W/cm^2$ for Al and $4x10^{-2}W/cm^2$ for Ti) and a very short time of deposition (few seconds). Several deposition times were used from 3 to 24s, in order to obtain different interlayer thicknesses, which seem to vary between 0.5nm and 1nm for Ti, 2nm for Al.

Thicknesses have been determined by XRR, but due to their very low values, XRR spectra are rough, thus only approximate fits can be obtained. Thicknesses calculations have also been made with ARXPS measurements and give thicknesses of the same order, which seems to confirm an interlayer thickness in the nanometer range.

The stack was finally studied by XPS and by WDXRF in order to observe the evolution of Ta_2O_5 and TiN oxidation. The parameters used for measurements are presented in 2.2.2.1 and 2.2.2.5.

4.2.2.2. Material characterizations

(i) XPS characterizations

Figure 42 shows in a) Ti*2p* spectra for samples with Ti interlayers and in b) Al*2p* region for samples with Al interlayers (for a better comprehension of XPS spectra see 2.2.2.1). In a), the Ti*2p* doublet is used for identification but for the clarity of the figure only the Ti$2p_{3/2}$ peak is shown. In b), the Al*2p* doublet is presented. As the peaks are very close (the doublet separation Δ_{Al2p} = 0.41 [16]) they are not identified separately. Finally, spectra for several deposition times are presented, with in a) 3, 6 and 8s of titanium and in b) 8, 12 and 24s of aluminum.

All the spectra present a unique contribution, identified thanks to literature in a) as TiO_2 with a peak at 458.3eV [17] and in b) as Al_2O_3 with a peak at 73.8eV [18]. As pure metals were deposited, the presence of these oxides means that the metallic interlayer is obviously oxidized. This could be due to the exposition to air of the sample, which happens between the deposition and the characterizations steps. It could also be due to the scavenging of the Ta_2O_5 by the Ti or Al, which therefore gives a TiO_2 or Al_2O_3 layer. In order to see if the oxygen scavenging has taken place in the sample, Ta*4f* and Ti$2p_{3/2}$ regions are analyzed to observe an eventual reduction of oxygen in the dielectric or at the bottom electrode.

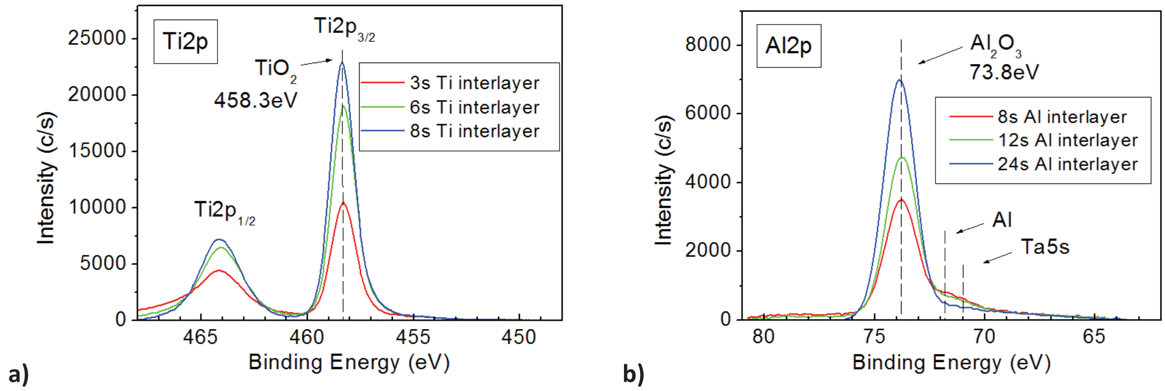

Figure 42: XPS Ti*2p* and Al*2p* spectra of samples with a) Ti and b) Al interlayers versus the deposition time

In Figure 43, Ta*4f* XPS spectra are presented, with the reference sample without interlayer in a), the Ta_2O_5/8s Ti-based sample in b) and the Ta_2O_5/8s Al-based sample in c). The entire doublet (Ta$4f_{7/2}$ and Ta$4f_{5/2}$ peaks) is used for the identification of contributions. However the binding energy values given in the graph correspond only to the Ta$4f_{7/2}$ peak to ease the graph reading. We can notice that the doublet separation Δ_{Ta4f}=1.8eV [19].

In the reference sample a contribution is observed at 25.7eV and according to literature it corresponds to Ta_2O_5 [19]. For the two samples with an interlayer a second contribution appears at 25.1eV. As it has a lower binding energy than for Ta_2O_5 peak it indicates the presence of tantalum sub oxide, here called TaO_x. Presence of this tantalum sub-oxide seems to prove that Al and Ti interlayers reduce the Ta_2O_5 electrolyte, forming TaO_x and potentially oxygen vacancies.

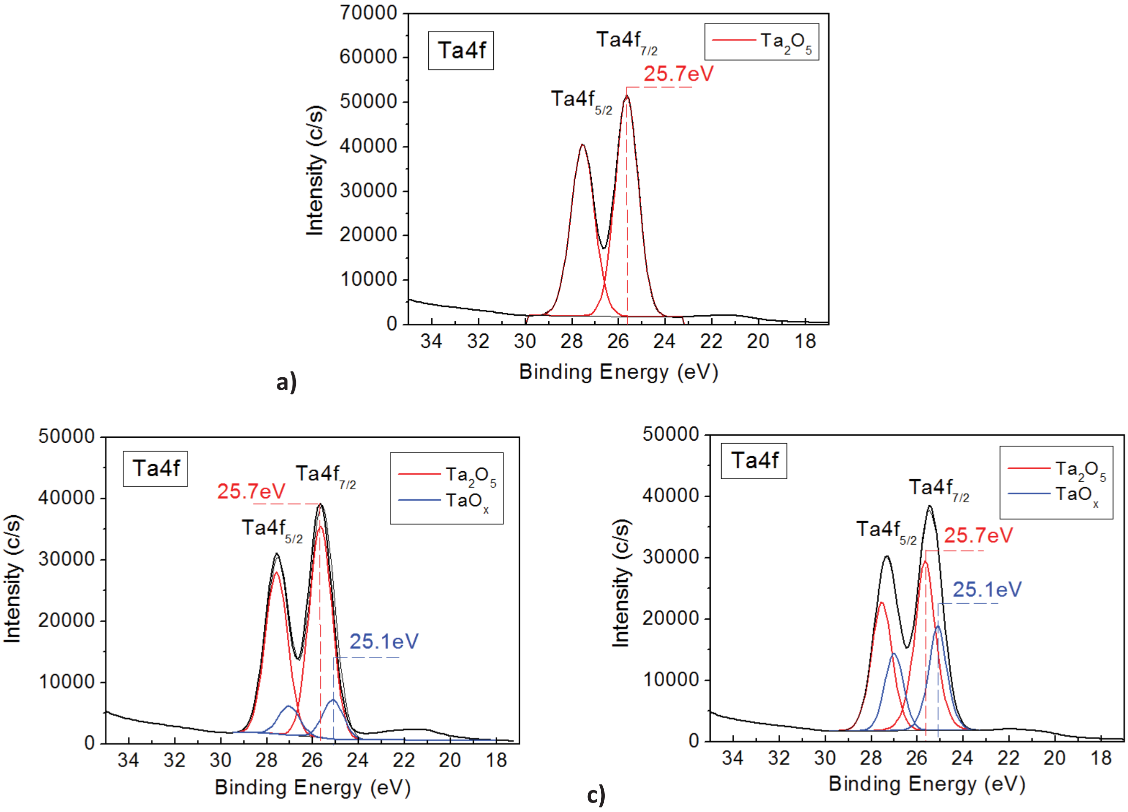

a)

b)

c)

Figure 43: Ta*4f* XPS spectra for a) TiN/Ta_2O_5 sample b) TiN/Ta_2O_5/8s Ti sample and c) TiN/Ta_2O_5/8s Al sample

In order to see if aluminum deoxidized also the titanium nitride bottom electrode, Ti*2p* XPS regions were analyzed. However as in the Ta_2O_5/Ti-based samples the bottom electrode TiN signal is mostly hidden by the TiO_2 interlayer signal, TiN reduction with a Ti interlayer cannot be observed by XPS. Consequently, only Ta_2O_5/Al-based samples are studied here. Therefore, the reference sample and Al interlayer samples for three deposition times are analyzed by XPS. Moreover, as the TiN is buried in the stack and as the evolutions investigated are probably very thin, only the Ti$2p_{3/2}$ peak is presented in Figure 44 in order to see clearly the differences between the samples.

The reference sample presents a peak at 458eV which corresponds to TiO_2 [17]. Then, samples with interlayers show a peak shifted toward low energies compared to the TiO_2 peak. This new position around 457.4eV could correspond to a sub-oxidized titanium as the binding energy is lower than for TiO_2. Thus, presence of sub-oxidized titanium is observed, when adding an Al interlayer. Therefore it seems that the Al interlayer also reduces oxygen in the bottom electrode.

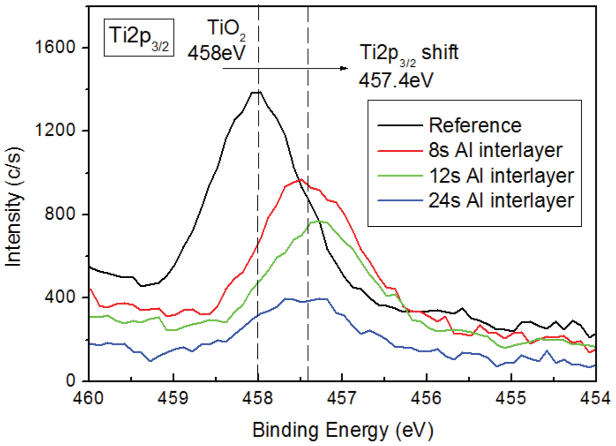

Figure 44: Ti*2p*$_{3/2}$ XPS spectra for TiN/Ta_2O_5 reference and the TiN/Ta_2O_5/Al samples

(ii) Impact of air on the interlayer

In previous paragraphs it was observed that interlayers scavenge the oxygen, leading to a reduction of the bottom electrode and of the dielectric together with an oxidation of the interlayer. However, the interlayer in these samples is in direct contact with the atmosphere. Thus, it could be partly oxidized by air break, reducing its impact on the other layers. In order to know if the interlayer is oxidized by the atmosphere, the amount of oxygen in the entire stack can be count. If it increases with the thickness of the metallic interlayer, it means that this supplementary oxygen comes from air. If the quantity of oxygen does not change with the increasing of the interlayer thickness, thus it is possible to say that the atmosphere does not oxidize the interlayer. In order to see the evolution of oxygen quantity in the stacks, WDXRF measurements were performed.

In Figure 45, WDXRF results are presented for Ta_2O_5/Ti- and Ta_2O_5/Al-based samples. For both cases when the deposition time increases, an increase of the oxygen WDXRF intensity is observed. Consequently, this additional oxygen can only come from atmosphere. Therefore, the oxidation of the interlayer observed by XPS in Figure 42 is partly due to air break. In other words, the interlayer instead of reacting only with Ta_2O_5, reacts with both air and Ta_2O_5. Therefore, it is possible that the interlayer does not have deoxidized the Ta_2O_5 as much as it could be expected regarding the deposition thicknesses.

Finally, when increasing the deposition time, the intensities seem to reach a plateau. It corresponds to a saturation in oxygen of the interlayer, conducting to passivation. In contact with air, titanium or aluminum oxides are formed at the surface of the samples. This oxidized surface limits the oxygen penetration in the stack and in increasing the interlayer thickness, the oxide at the surface become wider and improve the barrier against oxygen, therefore less atoms of oxygen can penetrate the stack.

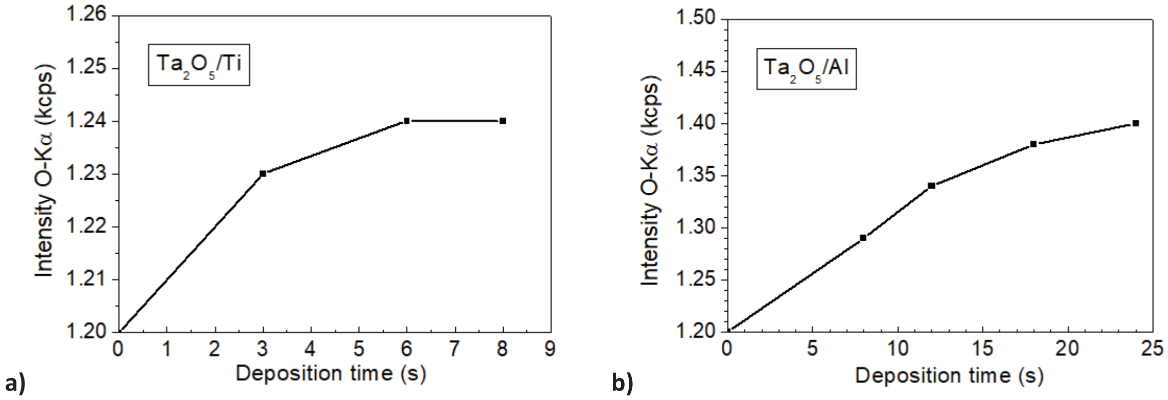

Figure 45: WDXRF O-Kα intensity in function of the deposition time for a) Ta_2O_5/Ti-based samples and b) Ta_2O_5/Al-based samples

4.2.2.3. Conclusions on the impact of interlayers on the stack

A summary is presented in Figure 46. XPS analyses reveal that when a titanium or aluminum interlayer is deposited on the dielectric, a reduction of the Ta_2O_5 dielectric together with the oxidation of the metallic interlayer take place. Moreover, with aluminum interlayer a reduction of the oxidized TiN bottom electrode (which is an unwanted source of oxygen in the memory stack) is also observed.

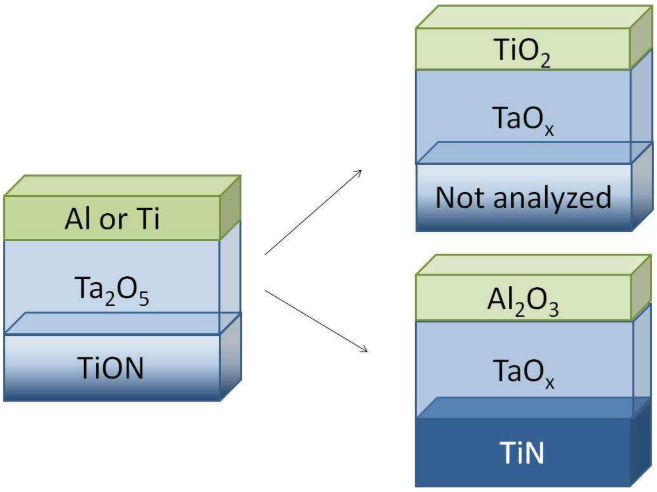

Figure 46: Summary of the impact of the interlayer on the stack layers

However, in both titanium and aluminum cases the WDXRF measurements prove that part of the interlayer oxidation is due to the air break. Thus, it is possible that in a memory stack the scavenging effect could be more efficient as the interlayer is not in contact with air and could therefore react entirely with Ta_2O_5. In order to see if a Ta_2O_5/Ti-based memory could work properly and to see if the memory behavior is OXRAM or CBRAM-like, the full memory stack must be studied through material characterizations and electrical tests.

4.2.3. HAXPES and ToF-SIMS study of a memory with titanium interlayer

4.2.3.1. Samples

The stack studied in this part is described in Figure 47. It is similar to the reference stack studied in 3.3.5, but with a 8s Ti interlayer added between the dielectric and the ion source layer. TiN is used instead of TaN for the top electrode. The interlayer was deposited with the same parameters as in 4.2.2. The stack was realized on a 200mm Si wafer and the Ti interlayer/ $CuTe_2Ge$/TiN were deposited through a shadow mask. Thicknesses were adapted for the HAXPES measurements which were performed with a 15keV incident energy, thus implying a maximum depth analyzed of around 50nm. Therefore, the global thickness of the stack is reduced compared to the chapter 3 reference stack in order to reach the tantalum bottom electrode. It gives the following stack: Ta 200nm/TiN 5nm/Ta_2O_5 10nm/Ti 8s/$CuTe_2Ge$ 15nm/TiN 5nm. The stack was then studied by ToF-SIMS and HAXPES at OFF and ON states, which means in pristine and formed states, in order to see modifications appearing after the forming.

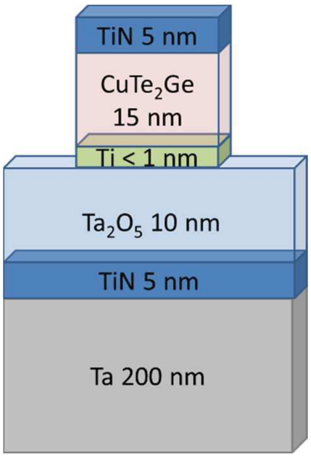

Figure 47: Stack studied to observe the impact of the interlayer on the forming

For ON state, a device was formed with a ramp voltage from 0V to 4V and a $5x10^{-3}$A compliance current. Then the HAXPES analyses were performed at the ESRF synchrotron with an incident energy of 15keV. The ToF-SIMS, which is a destructive technique, was thus performed at last on the sample. Sputter guns with 500eV O_2 or Cs were used, with an ion detection mode with Bi^+ and Bi^{3+} ions at 25keV and a detection of positive ions in M^+, M^- and MCs^+ modes. Here only the MCs^+ mode is presented in the ToF-SIMS profiles, but variations observed were also present with the other modes. Finally, as in the previous chapter position of the layers are indicated in ToF-SIMS graphs for a better comprehension.

4.2.3.2. Forming of the ON sample

The current-voltage curve obtained during the writing of the ON sample is displayed in Figure 48. The forming, which corresponds to the sudden increase of the current, appears clearly around 2V and is then followed by a plateau at $5x10^{-3}$A which corresponds to the chosen compliance.

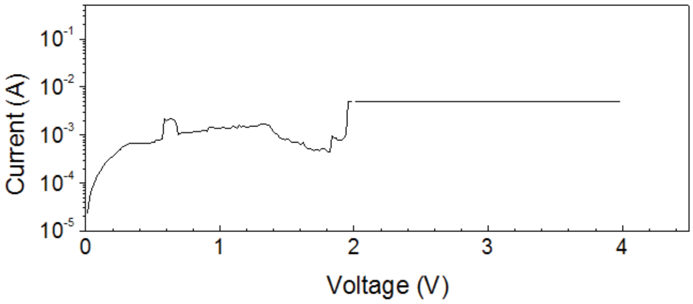

Figure 48: I-V curve obtained for the ON sample

4.2.3.3. Characterizations results

Copper, oxygen and tellurium ToF-SIMS MCs^+ profiles are presented in Figure 49, Figure 50 a) and Figure 51. The other chemical elements were also measured but are not shown here as they show overlapped OFF and ON spectra. It is observed that the precise positions of stack interfaces are very difficult to estimate. This is partly induced by the repelling of the atoms during ion sputtering, but it also reveals that $CuTe_2Ge$/ Ta_2O_5 layers are already well intermixed in the as-deposited stack. In other words, in the OFF sample layers have already diffused in each other.

In Figure 49, copper ToF-SIMS profiles in OFF and ON state are presented. First, in the OFF state it appears that copper has diffused toward the surface as an increase of its intensity appears in the TiN top electrode. This diffusion of copper through the top electrode is not observed in the reference stack (see 3.5.1.2). This may be due to the thin 5nm top electrode used here instead of the 50nm top electrode used in 3.3.5.

Then, in the ON state Cu intensity in the $CuTe_2Ge$ region decreases (see arrow 1). An increase of intensity is also observed in the signal incoming from the TaO_x region (arrow 2). This copper content shift toward longer sputtering times, observed after forming, corresponds to a diffusion of copper from the ion source layer toward the bottom electrode. This copper diffusion is consistent with a CBRAM behavior. This behavior is different from the one observed in 3.5 on reference stack. This point will be developed later in the discussion part in 4.2.3.4.

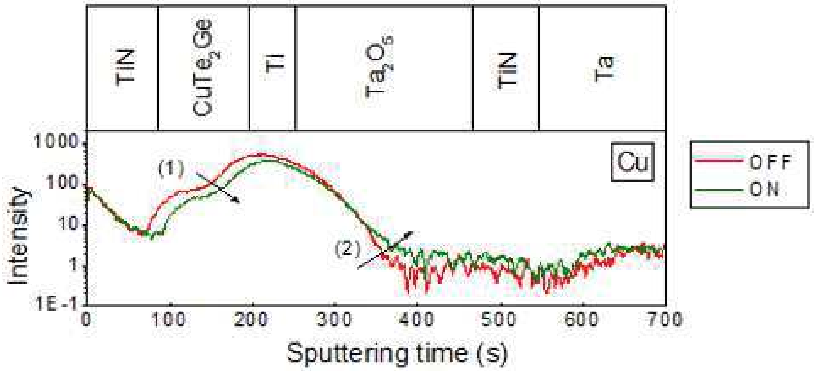

Figure 49: Copper ToF-SIMS profiles of OFF and ON samples

Figure 50 shows the oxygen ToF-SIMS profiles in a) and the corresponding HAXPES Ta$3d_{5/2}$ region in b) and c). Already in the OFF state, an interesting behavior can be noticed. Oxygen appears to be much more spread in the stack than in the reference sample in 3.5.1, where it appears to be confined in the Ta_2O_5 layer (see 3.5.1.2). This difference could be due to the substitution of 50nm-TaN top electrode in 3.3.5 by 5nm-TiN, which is probably too thin to protect the stack from atmosphere.

Then, when comparing OFF and ON states, the ON state profile shows a decrease of oxygen content in the dielectric. More precisely, it seems to occur in the TaO_x layer, as the shift seems to be more important in this layer than in other ones (see arrow 1). Moreover, an increase of oxygen content is also observed in the $CuTe_2Ge$ region (arrow 2). This oxygen content shift corresponds to an oxygen diffusion toward the surface. Additionally, it seems that the oxygen comes from the TaO_x layer. This last point is confirmed by the Ta$3d_{5/2}$ HAXPES spectra on the same samples presented in Figure 50 b) and c).

Ta$3d_{5/2}$ OFF and ON spectra show the same three contributions. The first peak around 1732.5eV is identified as metallic tantalum according to literature [20] and is attributed to the Ta bottom electrode. The peak situated around 1737.5eV is identified thanks to the chemical shift given in literature for Ta_2O_5: 4.7eV [21]. Addition of this value to the current position of the metallic tantalum (1732.5eV) gives a theoretical position for Ta_2O_5 peak at 1737.2eV. This is particularly close to the 1737.5eV peak which therefore could be identified as Ta_2O_5 and corresponds to the dielectric layer. Finally, the third peak situated around 1734.5eV is situated between the Ta and the Ta_2O_5 peak. Therefore it could correspond to tantalum sub-oxide, potentially formed by the titanium interlayer (see 4.2.2) as it is situated between Ta and Ta_2O_5 contributions. However, few TaN bonds can also be expected, coming from the Ta/TiN interface. We suppose that the principal contribution which corresponds to this peak is TaO_x.

Comparing OFF and ON samples, ON sample presents an increase of the metallic tantalum contribution intensity. This increase of the metallic contribution indicates the formation of oxygen vacancies in the dielectric. Therefore it is possible to say that oxygen vacancies are formed in the dielectric during the forming, which confirms the diffusion of oxygen from the TaO_x layer observed previously by ToF-SIMS.

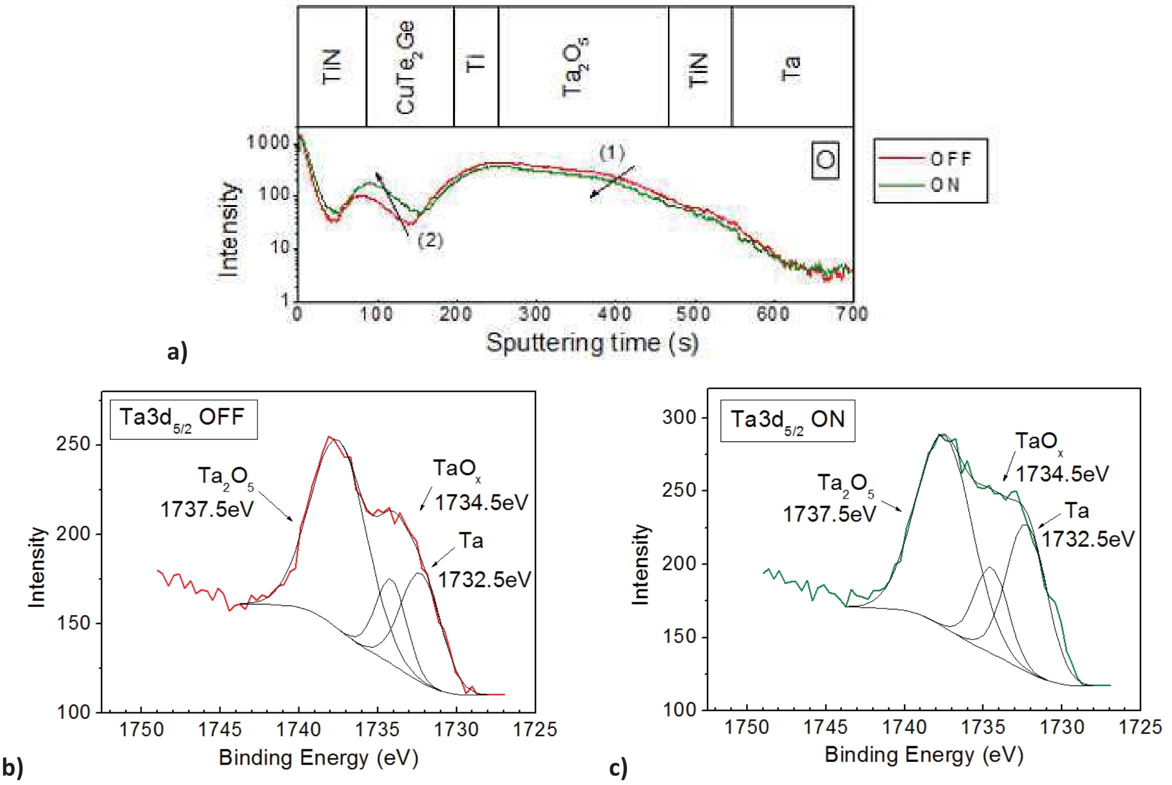

Figure 50: a) OFF and ON samples oxygen ToF-SIMS profiles ; b) OFF sample HAXPES Ta$3d_{5/2}$ spectrum ; c) ON sample HAXPES Ta$3d_{5/2}$ spectrum

The tellurium ToF-SIMS profiles are presented in Figure 51. In the OFF state some tellurium is already present at the top electrode surface as an increase of the intensity is observed around 0 and 20s sputter time. This implies that the tellurium could diffuse without electrical field from the ion source layer through the 5nm top electrode. Here again this behavior was not observed in the chapter 3 reference stack (see 3.5.1) where a 50nm top electrode was used.

Then, compared to OFF spectra, the ON sample shows a decrease of Te intensity in the $CuTe_2Ge$ layer (arrow 1) together with an increase of Te intensity in the TiN top electrode (arrow 2). Thus, the tellurium seems to diffuse from the $CuTe_2Ge$ layer toward the surface during forming, a behavior similar than oxygen.

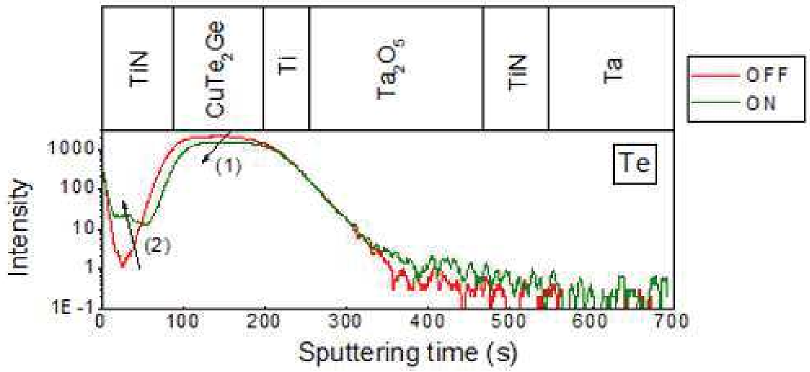

Figure 51: Tellurium ToF-SIMS profiles for OFF and ON samples

4.2.3.4. Discussion

Figure 52 summarizes the observations made above. After forming, the memory stack shows diffusion of copper from the ion source layer toward the bottom electrode (1), diffusion of oxygen from Ta_2O_5 toward the surface, thus forming oxygen vacancies (2), and diffusion of tellurium from the ion source layer toward the surface (3).

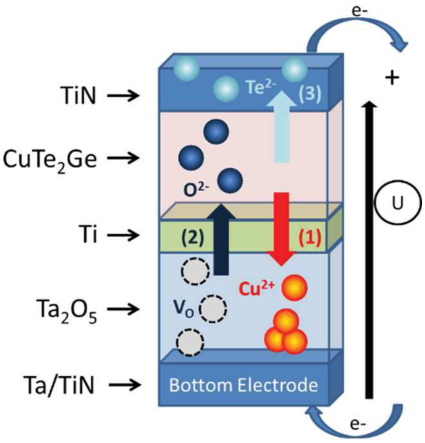

Figure 52: Summary of the forming mechanisms observed in the Ta_2O_5/Ti-based stack

The diffusion of copper after forming from the ion source layer toward the bottom electrode could lead to the metallic filament formation, with diffusion of copper cations through the dielectric until first filament is formed. This behavior seems to correspond to a CBRAM-like forming [22]. It is different from an OXRAM forming as observed in the Ta_2O_5 reference stack in 3.5, where the switching properties are mainly explained by vacancies evolution in a dielectric. The difference between the reference stack and the current study could be explained by the addition of the titanium interlayer. Indeed, we observed in 4.2.2 that the interlayer reduces the Ta_2O_5, leading to TaO_x dielectric probably essentially composed of vacancies ([5], [6]).

A diffusion of oxygen is also observed after forming in ON state, with oxygen movement from the Ta_2O_5 toward the surface. This diffusion is in the opposite direction with the copper diffusion. As already discuss in 3.2, if one adopts an electrochemical point of view to interpret the observed phenomena, negative counter charges are also expected to diffuse toward the top electrode when the copper cations diffuse toward the bottom electrode [23]. Here the oxygen seems to play the role of the counter-charges.

Part of the diffused oxygen in ON state comes from the Ta_2O_5 dielectric as observed in Figure 50. It means that some oxygen vacancies are formed in the dielectric during forming. Since the Gibbs free enthalpy of Ta-O is clearly higher than Ti-O or either Al-O (see Figure 41), this support the fact that potential assisted oxygen release is mainly occurring in the Ta_2O_5 volume rather than the TiO_2 interlayer (or even Ti-O bonds in the bottom electrode). As we see here both an oxygen and copper evolution when the potential is applied to the electrode, one conclude to an hybrid behavior between pure CBRAM, where the filament is mainly composed of diffused metal and pure OXRAM, where the filament is made of a path of local oxygen deficiencies namely vacancies.

As seen above, it seems that this hybrid CBRAM/OXRAM forming has been possible thanks to the insertion of the titanium interlayer which weakens the Ta_2O_5 diffusion barrier properties against copper ([1], [6]). So we see here that the forming mechanism is strongly correlated between vacancies and copper. Oxygen vacancies formed by Ti deposition and oxygen vacancies formed by the applied potential weaken the chemical barrier properties, which in turn eases copper diffusion. Stated differently, copper can easily follow paths formed by the organization of vacancies in the dielectric, i.e. vacancies are filled by copper atoms which leads to a lower forming potential. We also see that this mechanism also depends on the TiO_2 interlayer thickness, which can also play a role of barrier against copper injection from the ion source layer toward the Ta_2O_5. A too thick barrier may induce no copper diffusion. In the meantime, this barrier may play an important role regarding retention of copper once the cell is formed, as it can retain copper against back diffusion toward ion source layer.

Finally a third diffusion is also observed in the stack: the tellurium diffusion, from the ion source layer toward the surface. This diffusion is in the same direction than oxygen diffusion. One can notice that tellurium is a chalcogen, in other words that it is in the same column as oxygen in the periodic table. Therefore it seems possible to say here that tellurium has a similar chemical behavior than oxygen and thus diffuses in a Te^{2-} anion form and may also participate to the cell current flow.

4.2.4. Electrical tests of memories with titanium interlayer

In this part, electrical tests were performed on Ta_2O_5/Ti memories in order to see the impact on the forming voltage of the titanium interlayer.

4.2.4.1. Samples

In order to ease measurements and have a relatively reliable statistic, integrated memories were studied instead of simple memory plots deposited through a shadow mask. One should be aware that the available substrates in 1R configuration have a W bottom electrode instead of TiN. This can strongly influence the memory behavior, such as the required voltages to form the cells. Meanwhile, we try to achieve here a relative comparison between with and without Ti insertion.

The studied memory stacks are described in Figure 53. The different layers were deposited with the same parameters as described elsewhere (see 3.3) on the tungsten plugs and interlayers were deposited with the same parameters as in 4.2.2. Electrical tests were then performed on about 20 or 30 devices and average results are given below.

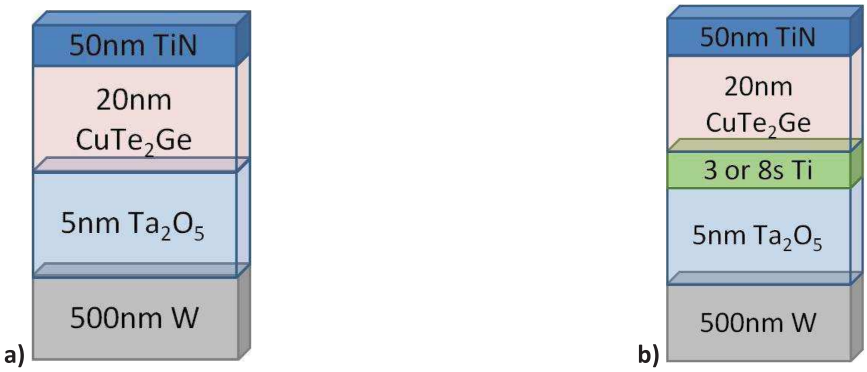

Figure 53: Memory stacks used during the electrical studies. a) the reference sample, b) the Ta_2O_5/3s and 8s Ti-based samples

4.2.4.2. Results and discussion

Figure 54 shows the average results of the electrical tests as a function of the titanium deposition time. Before any interpretation of these results, it is important to notice that in regards to the average values, the errors are important. Therefore the resistance or voltage variations observed must be taken with precaution as it may be not due to the real behavior of the memory stacks, but could only correspond to the measurements errors. In order to control if these variations are real behaviors or not, more samples with other Ti deposition time would have been tested. However this is not the case here, but it could be interesting for further researches.

In a) the pristine or initial resistance of the devices shows an increase with the Ti deposition time. It seems probably due to the dielectric thickness, which increases when depositing the titanium as the latter reacts with the tantalum oxide to form titanium oxide. In b) the forming voltage increases with the Ti thickness, which is linked to the increase of the initial resistance observed in a). However, this behavior could also be partly due to the copper barrier effect of the TiO_2, which increases with the interlayer thickness and which induces a higher forming voltage. Then in c) and d) the absolute value of reset and set voltages appear to decrease when increasing the titanium thickness. It could be partly explained by the oxygen vacancies present in the tantalum oxide. These one were expected to facilitate the diffusion of copper ions through the dielectric (see 4.2.3.4), thus the set and reset voltages can be lower than without the interlayer.

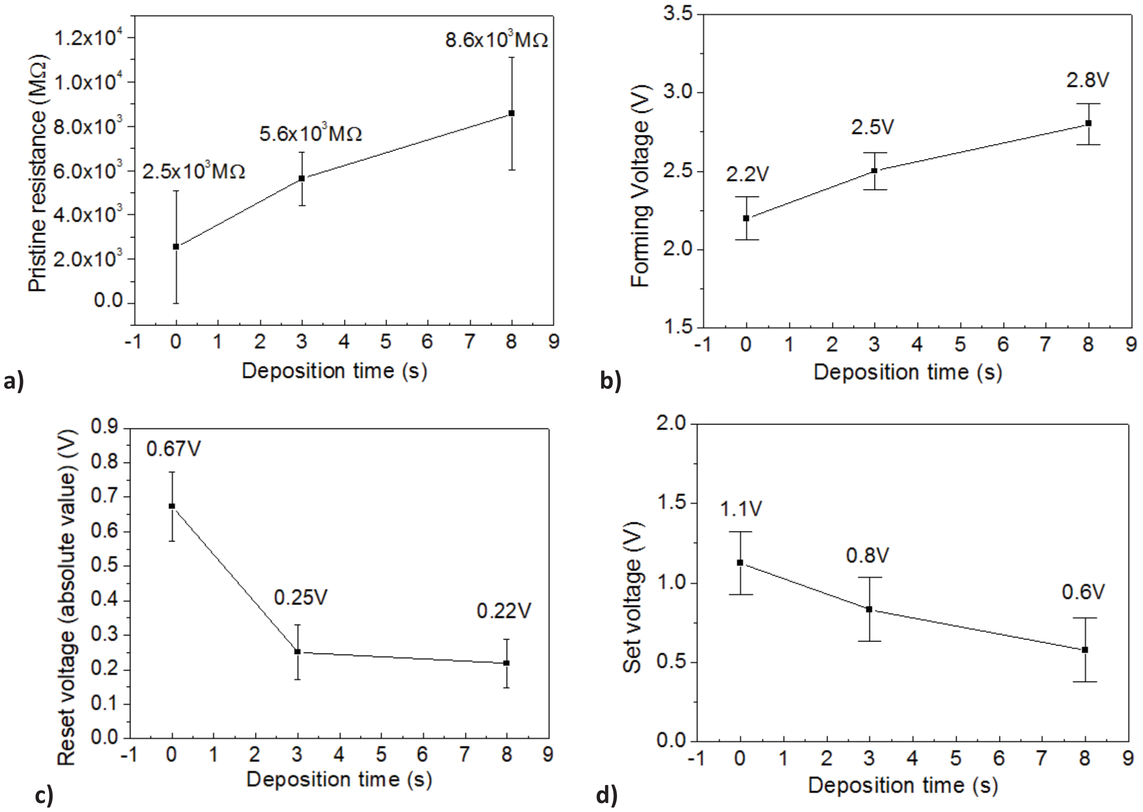

Figure 54: a) Pristine resistance, b) forming voltage, c) reset voltage and d) set voltage in function of the Ti interlayer deposition time

To conclude, it seems that the oxygen vacancies, which are expected to ease the diffusion of copper in the Ta_2O_5 layer, seem to have not a sufficient effect to decrease the forming voltage when increasing the thickness of the interlayer. Thus, the TiO_2 thickening has a greater impact on the forming voltage than the oxygen vacancies formed in the dielectric by the interlayer. However, the set and reset seem to be impacted principally by the oxygen vacancies, which enable a decrease of their voltages when increasing the interlayer thickness.

4.2.5. Conclusion on the interlayer

In this part, the influence of Ti inserted in the memory stack has been studied. The results show that the interlayer scavenges the dielectric, resulting in the formation of oxygen vacancies in the dielectric and the oxidation of the interlayer. These changes in the stack lead to a hybrid CBRAM/OXRAM-like behavior of the memory stack. Actually the CBRAM behavior seems to be due to the oxygen vacancies formed by the interlayer, as they could ease the copper diffusion. Moreover oxygen acts as a counter-charge, forming oxygen vacancies in the dielectric. These oxygen vacancies could correspond to a conductive path, leading to the OXRAM behavior. Additionally the tellurium was also observed to act as a counter charge. Finally, the electrical tests show that the pristine resistance and the forming voltage increase due to the increase of the oxidized interlayer thickness, whereas the reset and set voltage seem to decrease, due to the oxygen vacancies formed by the interlayer.

However, the real impact of the standard Gibbs free energy of the dielectric on the forming is still not very clear. Indeed as saw above the couple Ta_2O_5/Ti induces TiO_2/TaO_x bilayer, which in turn leads to in the hybrid forming observed above. Yet, we would like to see the effect if one uses another dielectric with a lower Gibbs free formation enthalpy such it is the case for gadolinium oxide.

4.3. Impact of gadolinium oxide dielectric on the memory

4.3.1. Introduction

In the previous part, hybrid CBRAM/OXRAM forming was observed when adding an interlayer at the ion source layer/dielectric interface in the Ta_2O_5-based reference stack. In consequence, copper, oxygen and tellurium diffusions were observed. The CBRAM behavior seems to be triggered by the oxygen vacancies formed by the interlayer deposition. We would like to know how the forming mechanisms are impacted if a dielectric with a lower standard Gibbs free energy than Ta_2O_5 is used.

For this purpose the dielectric proposed is the gadolinium oxide. This oxide, which has already been used in resistive memories ([28]-[30]), has been chosen for its low standard Gibbs free formation enthalpy. Indeed in Figure 55, the Ellingham diagram shows the standard Gibbs free energy versus the temperature for some oxides. The oxides studied previously as dielectric or as scavenger are displayed: the Ta_2O_5, the TiO_2 and the Al_2O_3. Gd_2O_3 is also displayed for comparison. It appears that the Gd_2O_3 has a standard Gibbs free energy clearly lower than Ta_2O_5, with ΔG_{Gd2O3}=-1155.5kJ/O_2 mol and ΔG_{Ta2O5}=-764.6kJ/O_2 mol at 25°C.

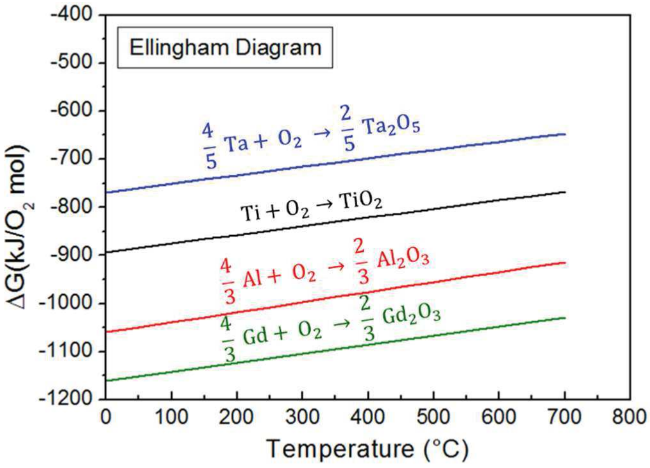

Figure 55: Ellingham diagram

Moreover the gadolinium oxide is highly hygroscopic [31]. The hygroscopy is the ability of a material to attract and retain water molecules. In Figure 56 we can see the ionic radii (in white squares) and the electronegativity (in black squares) of lanthanides metal elements (such as Pr, Sm, Gd and Dy) and the hygroscopic behavior of their respective oxides. The hygroscopicity increases with the ionic radius. Therefore, one can assume that GdO_x is much more hygroscopic than Ta_2O_5.

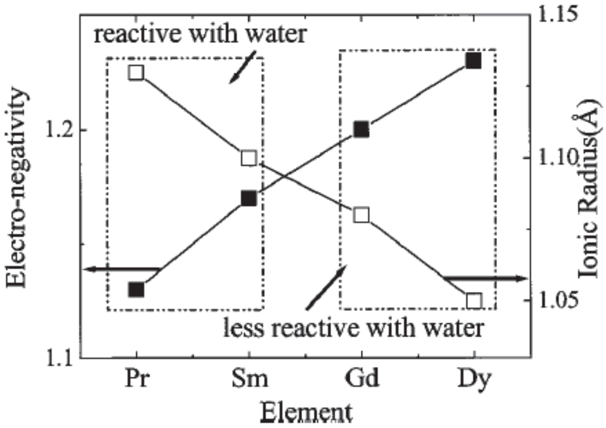

Figure 56: Ionic radii, electronegativity and hygroscopy for Pr, Sm, Gd and Dy

Strong metal-oxygen bonds in the dielectric may prevent oxygen atoms in the dielectric to act as counter-charges. Alternatively, the expected oxygen counter-charges that may trigger copper diffusion may be replaced by tellurium in the form of Te^{2-} ions as observed in 4.2.3. Another source of counter-charges could also be the hydroxide ions. Indeed, the air moisture could be absorbed in the layers and bring OH^- counter-charges [23]. The level of absorption depends on the used dielectric (linked to hygroscopic effects) and the way the devices are processed (geometry of the devices, air breaks, caps barriers, etc…). Therefore, in this section we try to understand the role of the oxygen bonding energy in the dielectric regarding the electro-forming and keeping in mind some probable hygroscopic effects prompt to induce OH^- ions.

4.3.2. HAXPES and ToF-SIMS study of GdO_x-based memory

4.3.2.1. Samples

The studied stack is presented in Figure 57. The stack was deposited on a 200mm silicon wafer and was composed of Ta 200nm/TiN 5nm/GdO_x 5nm/$CuTe_2Ge$ 15nm/Ti 5nm/TiN 5nm. Note that in this stack, the Ti interlayer has been deliberately deposited on top of the ion source layer instead of on the gadolinium oxide. This has been achieved by following the recommendations from the electrical team since their results were better in this configuration. The deposition parameters of the ion source layer and the electrodes are the same as described in 4.2.3, with the ion source layer and top electrode which were deposited through a shadow mask (see 2.1.2). The gadolinium oxide was deposited by RF-sputtering of a Gd_2O_3 target, with a 40sccm Ar flow and a power density of 2.5W/cm². As presented in Table 4, previous RBS measurements show that this gadolinium oxide layer deposited by RF-sputtering has a composition of 35.0% of gadolinium and 65.0% of oxygen. This implies a higher atomic percentage of oxygen than in a stoichiometric Gd_2O_3. This is probably due to the hygroscopicity of this dielectric, which thus absorbs lots of moisture when in contact with air [31]. As we are not sure on the exact composition of the deposited gadolinium oxide, the latter will be called GdO_x in this work.

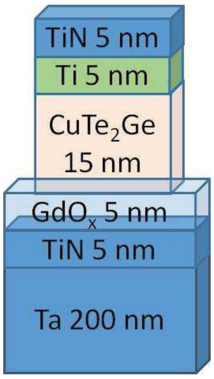

Figure 57: GdO$_x$-based stack

	Stoichiometric Gd$_2$O$_3$	**Deposited GdO$_x$**
Gd (atomic percent)	40	35.0±1.5
O (atomic percent)	60	65.0±1.5

Table 4: RBS deposited gadolinium oxide results

After deposition electrical tests were averaged on twelve devices to extract the forming voltage of the stack. Finally two devices were analyzed before and after the forming by ToF-SIMS and HAXPES in order to observe diffusions and bond environments in the stack. They are respectively called OFF and ON samples.

The ON sample was written thanks to a ramp voltage from 0 to 4V and with a compliance current of 20mA. Then, HAXPES analyses were performed at the ESRF synchrotron with an incident energy of 15keV. The ToF-SIMS was finally achieved in last as it is a destructive technique. Several ToF-SIMS parameters conditions were used in order to prevent confusion between the stack behavior and the matrix effects. For this purpose sputter guns with 500eV O$_2$ or Cs are used, with an ion detection mode with Bi$^+$ and Bi^{3+} ions at 25 keV. Moreover the detection of positive ions was performed in M$^+$, M$^-$ and MCs$^+$ modes.

4.3.2.2. Forming of the ON sample

In Figure 58, the current-voltage curve of the ON sample forming can be seen together with the 2V±0.5 average voltage obtained during the electrical tests. At around 2.1V, one observes on the curve a sudden current rise until it reaches the chosen compliance. This 2.1V forming voltage is in line with the average forming voltage measured on other devices.

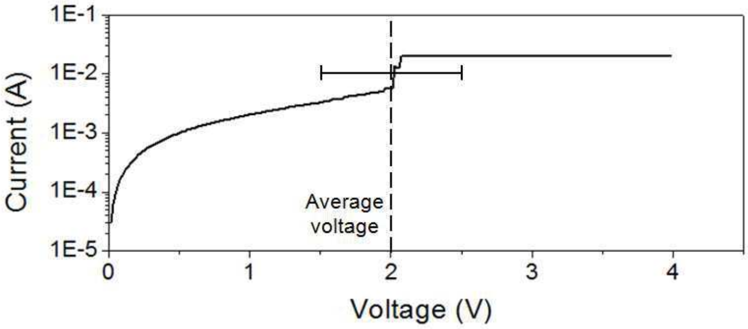

Figure 58: Filament forming I-V curve obtained with the GdO$_x$-based ON sample

4.3.2.3. ToF-SIMS and HAXPES results

The MCs$^+$ ToF-SIMS profiles of copper, oxygen and tellurium are respectively displayed in Figure 59, Figure 60 and Figure 61. As in the previous chapters, interfaces between layers are depicted in ToF-SIMS graphs for a better comprehension. The gadolinium, titanium, nitride and tantalum have also been measured by ToF-SIMS, however they do not present clear differences. Thus they are not presented here.

As in the Ta_2O_5/Ti stack studied in 4.2.3, the ToF-SIMS profiles show interface positions which are difficult to precisely determine. This is probably induced by the repelling of the atoms during ion sputtering but also due to intermixed films. In other words the layers have diffused in each other already at OFF state.

The Figure 59 presents the ToF-SIMS profiles of copper at OFF and ON states. Compared to OFF state profile, the ON state profile shows a decrease of intensity around 250s sputter time (see arrow 1), which could correspond to a decrease of copper content in the $CuTe_2Ge$ layer. Then, an increase of intensity is also observed around 450s (see arrow 2), which could correspond to an increase of copper content in the GdO_x or TiN layers. This shift of copper content toward longer sputtering times indicate a diffusion of copper after forming from the ion source layer toward the bottom electrode. Thus this behavior may be related to metallic filament formation. It is important to remark here that the differences between the two profiles are particularly low. However, we assume that the differences of intensity observed correspond to diffusions. These low differences will be also observed in the oxygen and tellurium profiles.

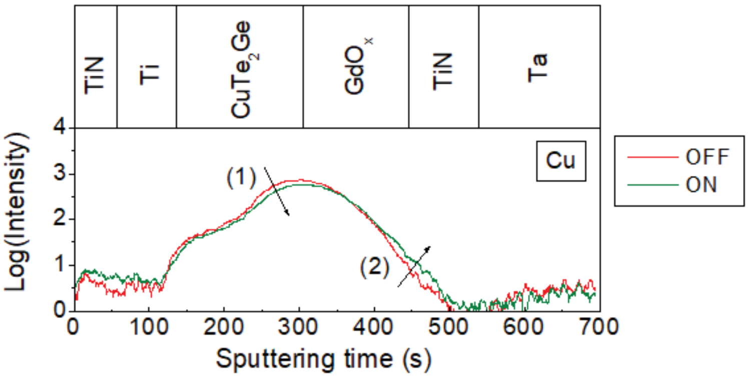

Figure 59: Copper OFF and ON samples ToF-SIMS profiles of the GdO_x stack

In Figure 60 a) the oxygen ToF-SIMS profiles of OFF and ON samples are displayed. Then in b), corresponding Gd$3p_{3/2}$ HAXPES spectra are presented.

Already in the OFF state we see that the oxygen is spread in the entire stack such as in the Ta_2O_5/Ti stack (see 4.2.3). As already explained in 4.2.3, this behavior is different from the reference sample in 3.5 where oxygen is mainly confined in the Ta_2O_5 layer (see 3.5.1.2). This difference in the copper behavior at OFF state could be due to the use of 5nm-TiN instead of 50nm-TaN into the reference, which seems to be not enough to protect the stack from air break.

The oxygen ToF-SIMS ON profile presents a small decrease of the intensity around 500s sputter time compared to the OFF profile (arrow 1), whereas an increase is observed around 200s (arrow 2). Thus it seems that the oxygen content decreases in the TiN layer and increases in the $CuTe_2Ge$ layer. Therefore it seems possible to say that an upward diffusion, apparently from the TiN bottom electrode, toward the ion source layer is observed after forming. As already discuss for the Ta_2O_5/Ti stack in 4.2.3, this oxygen diffusion could result from the counter charges required to diffuse copper cations when the electrochemical cell is closed. However, contrary to the previous Ta_2O_5/Ti-based stack, here the oxygen seems to come from the TiN bottom electrode and not from the dielectric.

HAXPES Ti1s spectra would have helped to confirm if the oxygen comes from the bottom electrode or not. However the presence of titanium nitride at both bottom and top electrodes induces the presence of both contributions in the HAXPES Ti1s spectra. Therefore, it is difficult to discriminate in the spectra the behavior of the bottom electrode from the top electrode. This is not the case for the Gd$2p_{3/2}$ core region that is presented in Figure 60. Spectra are particularly noisy, however despite the noise it seems that no shift appear between OFF and ON. This means that there are probably no chemical modifications of the GdO_x after the electro-forming. In other words, GdO_x does not shows any deoxidation after forming. This make sense if the oxygen which has acted as counter charge during the forming process is not coming from the GdO_x layer but rather from the TiN bottom electrode, which supports the observation made by ToF-SIMS.

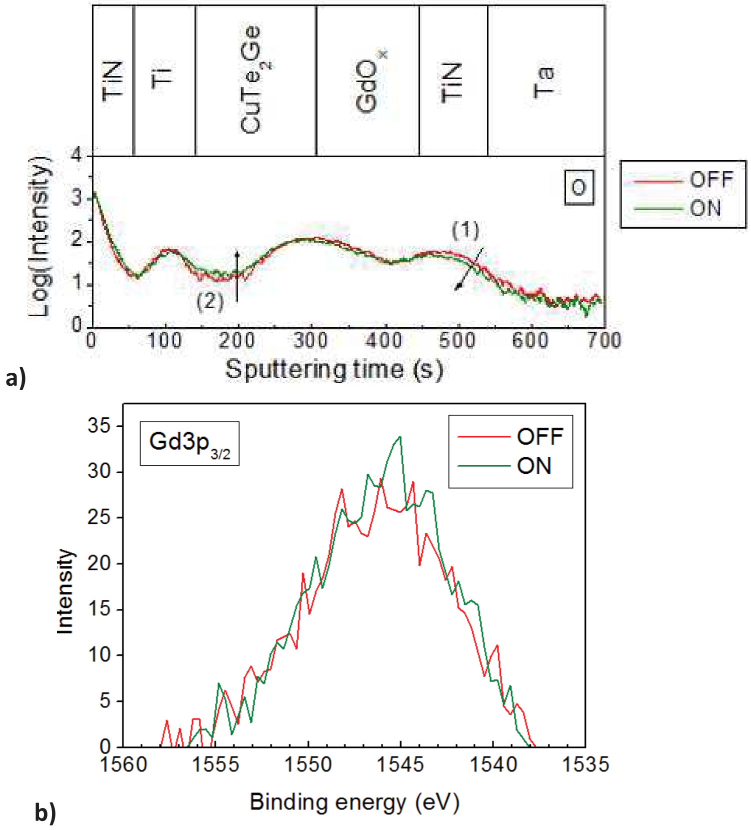

Figure 60: a) Oxygen OFF and ON ToF-SIMS profiles ; b) Gd$3p_{3/2}$ HAXPES spectra of OFF and ON samples

Finally, tellurium ToF-SIMS profiles are displayed in Figure 61. It is possible to see that already at OFF state some tellurium is present at the top electrode surface. Indeed an increase of tellurium intensity is observed between around 0-50s. Thus a diffusion of the tellurium from the ion source layer toward the surface at OFF state takes place. This behavior was already reported in the Ta_2O_5/Ti sample (4.2.3), together with a diffusion of oxygen and copper. The top electrode is supposed to be too thin to act as a tellurium diffusion barrier.

When comparing OFF and ON states profiles, ON profile presents a decrease of intensity around 300s (arrow 1) together with an increase around 0-80s (see arrow 2). Thus, the tellurium content seems to decrease in the $CuTe_2Ge$ layer and to increase in the TiN top electrode. This behavior is also explained by an upward diffusion assisted by the applied potential of tellurium from $CuTe_2Ge$ toward the surface during the forming. This behavior, already observed in the Ta_2O_5/Ti-based stack is similar to the oxygen behavior (see 4.2.3.4).

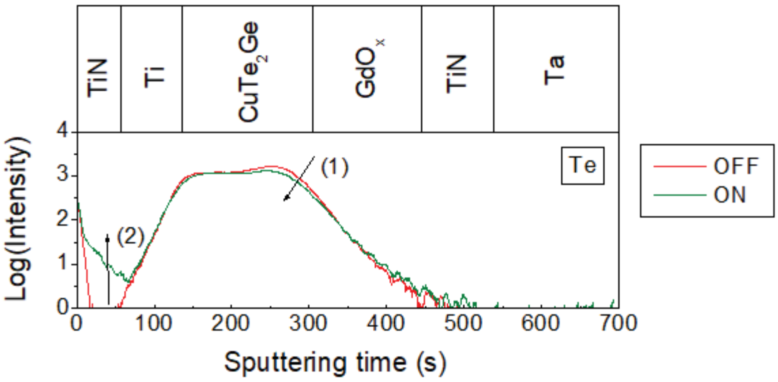

Figure 61: Tellurium ToF-SIMS profiles of OFF and ON samples

4.3.2.4. Discussions

The Figure 62 summarizes the forming mechanisms observed in the GdO_x stack. When the electrical circuit is closed, at a given potential corresponding to the electro-forming, a diffusion of copper takes place from the ions source layer toward the bottom electrode (1), together with a diffusion of oxygen from the bottom electrode toward the surface (2). Diffusion of tellurium is also observed from the ion source layer to the top electrode surface (3).

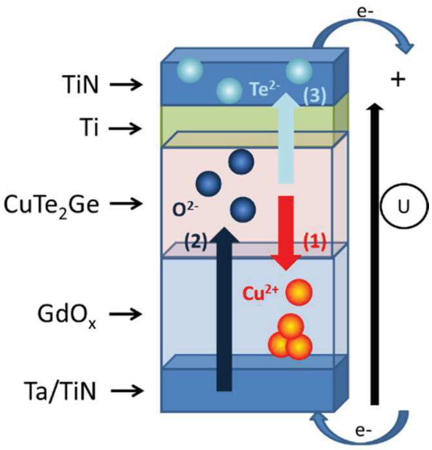

Figure 62: Summary of the forming mechanisms observed in the GdO_x-based stack

The diffusion of copper from the ion source layer toward the bottom electrode is attributed to a cationic based diffusion as expected in CBRAM cell. As in the Ta_2O_5/Ti stack, a diffusion of oxygen in the opposite direction is observed. Indeed, as already discuss in 3.2 and 4.2.3, the diffusion of copper and the counter charges required to trigger this cationic diffusion are intimately linked [23]. In the current process, oxygen seems to play the role of counter charges. However, contrary to the Ta_2O_5/Ti stack, in GdO_x memory the oxygen seems to find its source in the bottom electrode rather than in the bulk the dielectric. This, in turn, leads to a CBRAM-like forming rather than a hybrid OXRAM/CBRAM process as observed in reduced TaO_x dielectric, where vacancies appeared to play the major role in the electro-forming process.

This phenomenon can at least be explained considering the very low Gibbs free formation enthalpy of Gd-O system compared to Ta-O. Indeed as observed in the Ellingham diagram in Figure 55, the standard Gibbs free energy of GdO_x at 25°C is -1155.5kJ/O_2 mole whereas for Ta_2O_5 it is -764.6kJ/O_2 mole. Knowing that fact, one can expect that the gadolinium oxide has a stronger metal to oxygen bond than the tantalum oxide. Therefore, these bonds are expected to be more difficult to break, which prevent oxygen to diffuse from the bulk dielectric. Also, the oxygen comes from the bottom electrode, meaning that the latter is oxidized. This source of oxygen may find its origin in the hygroscopic behavior of GdO_x where the dielectric can absorb a noticeable amount of moisture (compared to TaO_x) during the short air-break required for shadow mask insertion (see 2.1.2). The moisture could partly oxidize the titanium nitride bottom electrode which is in direct contact with the gadolinium oxide. Therefore the oxygen observed here could be O^{2-} or OH^- anions, originating from moisture as in literature [23].

A third diffusion path is also observed in the stack: the tellurium, whose main role is to ionize copper in the ion source layer in cationic form, diffuses from the ion source layer toward the surface. As already noticed in section 4.2.3.4, tellurium may also be active in the diffusion process since its chemical behavior is close to oxygen (in the same column in the periodic table). Therefore, it is also possible to imagine that tellurium acts as counter charge in this GdO_x-based stack.

4.4. Conclusions

In this chapter, starting from the reference stack described in 3.3.5, we inserted a thin Ti or Al scavenger as interlayer between the ion source layer and the dielectric. We achieved an in-depth analysis of the elements positions and chemical environments before and after applying an external potential to the cell electrodes. XPS analyses show that the interlayer reduces the Ta_2O_5 and the TiN bottom electrode, thus forming oxygen vacancies in the dielectric and an oxidized TiO_2 or Al_2O_3 interlayer.

HAXPES and ToF-SIMS before and after filament formation show a diffusion of copper together with counter-diffusion of oxygen and tellurium. As the oxygen comes from the Ta_2O_5, it is believed that oxygen vacancies are formed in the bulk dielectric through reduction of Ta_2O_5 in TaO_x. We propose that the Ta_2O_5/Ti solution may be viewed as a hybrid CBRAM/OXRAM concept where a copper conductive filament is triggered by counter-charges represented by the oxygen coming from the Ta_2O_5. Stated differently, copper could diffuse in the path formed of vacancies in Ta_2O_5.

The formation of oxygen vacancies during the forming are expected to be partly induced by the low Ta_2O_5 standard Gibbs free energy (compared to other dielectrics). In order to support this hypothesis, we replaced Ta_2O_5 with GdO_x, knowing that GdO_x has a clear lower standard Gibbs free energy than Ta_2O_5 and that it is very reactive to moisture due to its high hygroscopicity.

HAXPES and ToF-SIMS before and after forming show a diffusion of copper and counter-diffusion of oxygen and tellurium. However in this latter case the oxygen does not come from the bulk dielectric but from the bottom electrode which is maybe oxidized by moisture absorbed by the gadolinium oxide. Therefore, it is possible to say that this stack seems to have a pure CBRAM behavior, with formation of copper filament and counter-diffusion of oxygen or hydroxide ions and tellurium ions. We conclude that the strength of the metal-oxygen bond and the hygroscopicity of the dielectric may play a major role in the memory behavior, in particular in the forming mechanism. Here, it is important to keep in mind that the ToF-SIMS results were delicate to interpret as the differences observed between OFF and ON spectra were particularly low.

4.5. **Bibliography**

[1] P. Lorenzi, R. Rao, G. Romano, and F. Irrera, “Model of Reversible Breakdown in HfO_2 Based on Fractal Patterns”, Advances in Condensed Matter Physics, vol. 2015, pp. 1–8, 2015.

[2] N. Xu, L. Liu, X. Sun, X. Liu, D. Han, Y. Wang, R. Han, J. Kang and B. Yu, “Characteristics and mechanism of conduction/set process in TiN∕ZnO∕Pt resistance switching random-access memories”, Applied Physics Letters, vol. 92, no. 23, p. 232112, 2008.

[3] M. Saadi, P. Gonon, C. Vallée, C. Mannequin, H. Grampeix, E. Jalaguier, F. Jomni and A. Bsiesy, “On the mechanisms of cation injection in conducting bridge memories: The case of HfO_2 in contact with noble metal anodes (Au, Cu, Ag)”, Journal of Applied Physics, vol. 119, no. 11, p. 114501, 2016.

[4] D. Jana, S. Roy, R. Panja, M. Dutta, S. Z. Rahaman, R. Mahapatra, and S. Maikap, “Conductive-bridging random access memory: challenges and opportunity for 3D architecture”, Nanoscale Research Letters, vol. 10, no. 1, 2015.

[5] B. Attarimashalkoubeh, A. Prakash, S. Lee, J. Song, J. Woo, S. H. Misha, N. Tamanna, and H. Hwang, “Effects of Ti Buffer Layer on Retention and Electrical Characteristics of Cu-Based Conductive-Bridge Random Access Memory (CBRAM) ”, ECS Solid State Letters, vol. 3, no. 10, pp. P120–P122, 2014.

[6] S. Z. Rahaman, S. Maikap, T.-C. Tien, H.-Y. Lee, W.-S. Chen, F. T. Chen, M.-J. Kao, and M.-J. Tsai, “Excellent resistive memory characteristics and switching mechanism using a Ti nanolayer at the Cu/TaO_x interface”, Nanoscale research letters, vol. 7, no. 1, pp. 1–11, 2012.

[7] A. Prakash, S. Maikap, H.-C. Chiu, T.-C. Tien, and C.-S. Lai, “Enhanced resistive switching memory characteristics and mechanism using a Ti nanolayer at the W/TaO_x interface”, Nanoscale Research Letters, vol. 9, p. 125, 2014.

[8] H. Wu, X. Li, M. Wu, F. Huang, Z. Yu, and H. Qian, “Resistive Switching Performance Improvement of Ta_2O_{5-x}/TaO_y Bilayer ReRAM Devices by Inserting AlO_x Barrier Layer”, IEEE Electron Device Letters, vol. 35, no. 1, pp. 39–41, 2014.

[9] S. Kim, S. Cho, and B.-G. Park, “Improved resistive switching properties in SiO_x-based resistive random-access memory cell with Ti buffer layer”, Journal of Vacuum Science & Technology B, Nanotechnology and Microelectronics: Materials, Processing, Measurement, and Phenomena, vol. 34, no. 2, p. 022204, 2016.

[10] L. D. V. Sangani, C. R. Kumar, and M. G. Krishna, “Interfacial Electrode-Driven Enhancement of the Switching Parameters of a Copper Oxide-Based Resistive Random-Access Memory Device”, Journal of Electronic Materials, vol. 45, no. 1, pp. 322–328, 2016.

[11] S.-F. Ding, Q. Xie, F. Chen, H.-S. Lu, S.-R. Deng, D. Deduytsche, C. Detavernier, and X.-P. Qu, “Improved Thermal Stability and Electrical Performance by Using PEALD Ultrathin Al_2O_3 Film

with Ta as Cu Diffusion Barrier on Low k Dielectrics", ECS Solid State Letters, vol. 1, no. 3, pp. P54–P56, 2012.

[12]S.-F. Ding, Q. Xie, F. Chen, H.-S. Lu, S.-R. Deng, C. Detavernier, G.-P. Ru, Y.-L. Jiang, and X.-P. Qu, "Investigation of ultra-thin Al_2O_3 film as Cu diffusion barrier on low-k (k= 2.5) dielectrics", in 2011 IEEE International Interconnect Technology Conference and 2011 Materials for Advanced Metallization (IITC/MAM), pp. 1-3, 2011.

[13]P. Majumder, R. Katamreddy, and C. Takoudis, "Effect of film thickness on the breakdown temperature of atomic layer deposited ultrathin HfO_2 and Al_2O_3 diffusion barriers in copper metallization", Journal of Crystal Growth, vol. 309, no. 1, pp. 12–17, 2007.

[14]F. Moya, E.G. Moya, D. Juvé, D. Tréheux, C. Grattepain, and M. Aucouturier, "SIMS Study of Copper diffusion into bulk Alumina", Scripta Metallurgica et Materiala, vol. 28, pp. 343–348, 1993.

[15]Q. Xie, J. Musschoot, D. Deduytsche, R. L. Van Meirhaeghe, C. Detavernier, S. Van den Berghe, Y.-L. Jiang, G.-P. Ru, B.-Z. Li and X.-P. Qu, "Growth Kinetics and Crystallization Behavior of TiO_2 Films Prepared by Plasma Enhanced Atomic Layer Deposition", Journal of The Electrochemical Society, vol. 155, no. 9, p. H688, 2008.

[16]C. Berg, S. Raaen, A. Borg, J. N. Andersen, E. Lundgren, and R. Nyholm, "Observation of a low-binding energy peak in the *2p* core-level photoemission from oxidized Al(111)", Physical Review B, vol. 47, no. 19, p. 13063, 1993.

[17]Y. Cheng and Y. F. Zheng, "Surface characterization and mechanical property of TiN/Ti-coated NiTi alloy by PIIID", Surface and Coatings Technology, vol. 201, no. 15, pp. 6869–6873, 2007.

[18]C. D. Wagner, "Auger and photoelectron line energy relationships in aluminum–oxygen and silicon–oxygen compounds", Journal of Vacuum Science and Technology, vol. 21, no. 4, p. 933, 1982.

[19]C. Guoping, L. Lingzhen, Z. Suixin, and Z. Haokang, "Structures and properties of a Ta_2O_5 thin film deposited by dc magnetron reactive sputtering in a pure O_2 atmosphere", Vacuum, vol. 41, no. 4, pp. 1204–1206, 1990.

[20]W. Huschka, D. Ross, M. Maier, and E. Umbach, "Calibrated binding energies of some core levels in the energy range between 1.5–4 keV", Journal of electron spectroscopy and related phenomena, vol. 46, no. 2, pp. 273–276, 1988.

[21]D. D. Sarma and C. N. R. Rao, "XPES studies of oxides of second- and third-row transition metals including rare earths", Journal of Electron Spectroscopy and Related Phenomena, vol. 20, p. 25, 1980.

[22]R. Waser, R. Dittmann, G. Staikov, and K. Szot, "Redox-Based Resistive Switching Memories - Nanoionic Mechanisms, Prospects, and Challenges", Advanced Materials, vol. 21, no. 25–26, pp. 2632–2663, 2009.

[23]S. Tappertzhofen, I. Valov, T. Tsuruoka, T. Hasegawa, R. Waser, and M. Aono, "Generic Relevance of Counter Charges for Cation-Based Nanoscale Resistive Switching Memories", ACS Nano, vol. 7, no. 7, pp. 6396–6402, 2013.

[24]L. Yang, C. Kuegeler, K. Szot, A. Ruediger, and R. Waser, "The influence of copper top electrodes on the resistive switching effect in TiO_2 thin films studied by conductive atomic force microscopy", Applied Physics Letters, vol. 95, no. 1, p. 013109, 2009.

[25]Y. Kang, M. Verma, T. Potnis, T. Liu, and M. Orlowski, "Conditions for Formation and Rupture of Multiple Conductive Cu and V_O Filaments in a Cu/TaO_x/Pt Device", ECS Transactions, vol. 50, no. 34, pp. 19–24, 2013.

[26]H. Jeon, J. Park, W. Jang, H. Kim, H. Song, H. Kim, H. Seo, and H. Jeon, “Resistive switching behaviors of Cu/TaO_x/TiN device with combined oxygen vacancy/copper conductive filaments”, Current Applied Physics, vol. 15, no. 9, pp. 1005–1009, 2015.

[27]A. Wedig, M. Luebben, D.-Y. Cho, M. Moors, K. Skaja, V. Rana, T. Hasegawa, K. K. Adepalli, B. Yildiz, R. Waser, and I. Valov, “Nanoscale cation motion in TaO_x, HfO_x and TiO_x memristive systems”, Nature Nanotechnology, 2015.

[28]K. Aratani, K. Ohba, T. Mizuguchi, S. Yasuda, T. Shiimoto, T. Tsushima, T. Sone, K. Endo, A. Kouchiyama, S. Sasaki, and others, “A novel resistance memory with high scalability and nanosecond switching”, in 2007 IEEE International Electron Devices Meeting (IEDM), pp. 783–786, 2007.

[29]K.-C. Liu, W.-H. Tzeng, K.-M. Chang, Y.-C. Chan, C.-C. Kuo, and C.-W. Cheng, “The resistive switching characteristics of a Ti/Gd_2O_3/Pt RRAM device”, Microelectronics Reliability, vol. 50, no. 5, pp. 670–673, 2010.

[30]J.-C. Wang, Y.-R. Ye, J.-S. Syu, P.-R. Wu, C.-I. Wu, P.-S. Wang, and J. H. Chang, “Low-Power and High-Reliability Gadolinium Oxide Resistive Switching Memory with Remote Ammonia Plasma Treatment”, Japanese Journal of Applied Physics, vol. 52, no. 4S, p. 04CD07, 2013.

[31]S. Jeon and H. Hwang, “Effect of hygroscopic nature on the electrical characteristics of lanthanide oxides (Pr_2O_3, Sm_2O_3, Gd_2O_3, and Dy_2O_3)”, Journal of Applied Physics, vol. 93, no. 10, p. 6393, 2003.

Chapter 5: Impact of the ion source layer on the forming

5.1. Introduction

In Chapter 3, it was observed that the Ta_2O_5 reference stack seems to present an OXRAM-like forming. First, when one increases the voltage at the memory electrodes, the dielectric broke before a first copper filament is formed. This led us to interpret the observed phenomena as an OXRAM-like mechanism (i.e. based on vacancies through oxygen evolution), instead of the expected CBRAM cationic-based behavior. In such instable systems, it is clear that a modification of the dielectric or of the ion source layer could modify the type of forming obtained in the memory cell. Therefore, as the impact of the dielectric properties on the forming was studied in the chapter 4, in this chapter we propose to further understand the role the ion source layer on the memory operation.

For this purpose, in this chapter new ion source layers are developed and studied through material characterizations and electrical tests. In 3.3.1, the chosen composition of ion source layer was $CuTe_2$ (rich Te composition), owing to its availability to ease the reset. Here, the $Cu_{60}Te_{40}$ alloy will be mainly studied. Indeed, in literature it is expected to bring a more stable filament ([1]-[2]) than $CuTe_2$.

First, the impact of germanium on the $Cu_{60}Te_{40}$ alloy will be studied, in particular its influence on crystallinity. Then, the influence of the alloy composition on the forming will be studied through the comparison of memory stacks containing $Cu_{60}Te_{40}$ + Ge (+Ge referring to the fact that we used two targets to deposit the alloy, this will be explained further) versus $CuTe_2Ge$ ion source layer. In a third part the impact of an oxygen scavenger, a metal such as zirconium alloyed in the ion source layer, will be studied. Finally, in the last part the tellurium and zirconium role in the memory will be studied, through the study of a ZrTe ion source layer.

5.2. Amorphization role of germanium

5.2.1. Introduction

As discussed in 3.3.1 Figure 29, CuTe alloy phase diagram is complex with many instable phases up to the 400°C required for the integration. Moreover, they are rough and inhomogeneous at several compositions and crystalline (see 3.3.1 Figure 30 and Figure 31). For all these reasons CuTe alloy is difficult to integrate. A solution proposed was to amorphize the layer thanks to an inhibitor of crystallization, such as germanium. Amorphization is expected to increase the crystallization temperature, improving the stability in temperature and bringing a smooth surface. The behavior of germanium as crystallization inhibitor has been previously reported in chalcogenides, in particular in PCRAM ([3], [4]). This behavior is supposed to be due to the large coordination number of germanium and its ability to form strong bonds, enabling strong Ge-Te bonds, more difficult to break. Therefore, the crystallization which corresponds to a rearrangement of atoms in the material, needs a higher temperature than in pure CuTe alloys. In other words, germanium could contribute to the stability in temperature of the CuTe layer by increasing its crystallization temperature.

5.2.2. Samples and RBS results

To confirm the germanium impact on the layer crystallization, 20nm-$Cu_{60}Te_{40}$ with Ge alloy is analyzed by XRD. Moreover, the alloy will be compared with a 20nm-$Cu_{60}Te_{40}$ sample by XPS. The 20nm-$Cu_{60}Te_{40}$ with Ge layer is co-deposited by sputtering of $Cu_{60}Te_{40}$ and Ge targets with an Ar flow of 40sccm. The $Cu_{60}Te_{40}$ is deposited with a power density of 0.6W/cm^2 and Ge with a power of 0.3W/cm^2. Its composition was not measured, but RBS results for the same set of samples give a Cu/Te ratio of 1.3 for the $Cu_{60}Te_{40}$ alloy and a composition of 9.7% and 32.5% of germanium when applying respectively 0.2W/cm^2 or 0.8W/cm^2 power density on the Ge target. These results indicate that the deposited $Cu_{60}Te_{40}$ is slightly richer in tellurium than the expected stoichiometric $Cu_{60}Te_{40}$ as the Cu/Te ratio is 1.3 and not 1.5. However, this layer will still be called "$Cu_{60}Te_{40}$" in this work.

5.2.3. Study of the crystallinity

Figure 63 shows the XRD spectrum of the 20nm thick $Cu_{60}Te_{40}$ + Ge sample. The $Cu_{60}Te_{40}$ + Ge spectrum is noisy, without peaks. This indicates the absence of crystals or nano-crystals in the detection limit of the XRD equipment. In other words, it corresponds to an amorphous signature of the layer. It confirms that the germanium acts as an inhibitor of the crystallization in the $Cu_{60}Te_{40}$ layer. Then, XPS analyses are performed on the samples to evaluate the chemical environment around germanium.

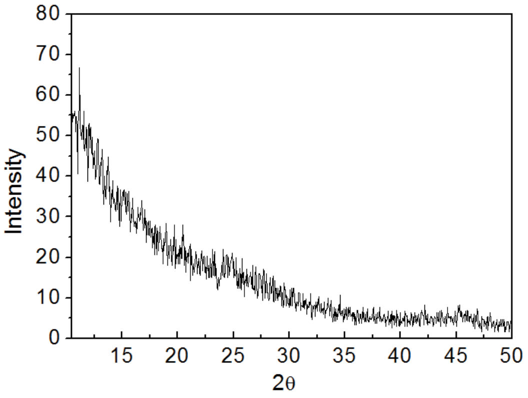

Figure 63: XRD spectra of the $Cu_{60}Te_{40}Ge$ sample

5.2.4. Chemical environments of Ge in $Cu_{60}Te_{40}Ge$

Some references are first processed and analyzed by XPS in order to ease the fit of the $Cu_{60}Te_{40}$-based samples. For this purpose pure Te and TeO_2 layers are used, and deposited by sputtering or reactive sputtering of a Te target with a power density around 0.6W/cm^2. For the Te sample the Ar flow used is set at 40sccm, whereas for the TeO_2 sample Ar 10sccm and O_2 30sccm are mixed. Te and TeO_2 reference samples Te*3d* XPS spectra are presented respectively in Figure 64 a) and b).

In these reference spectra, Te*3d* doublet is visible but only Te$3d_{5/2}$ is used for the fit. In a), three contributions are observed, with Te at 573.1eV and TeO_2 at 576.4eV as described in literature [5]. The third peak, at 573.5eV, is situated between TeO_2 and metallic Te binding energies. As no other bond as Te-Te or Te-O bonds is expected, this peak corresponds probably to sub-oxidized tellurium. It will be called TeO_x as its stoichiometry is unknown. In b), two contributions are recorded, one at 576.4eV which corresponds to TeO_2 [5] and a second one at 573.9eV. As in the previous sample, this contribution is situated between TeO_2 and metallic Te binding energies. Therefore, it is probably sub-oxidized tellurium, probably more oxidized than in the pure Te sample as its binding energy is slightly lower than in the TeO_2 sample.

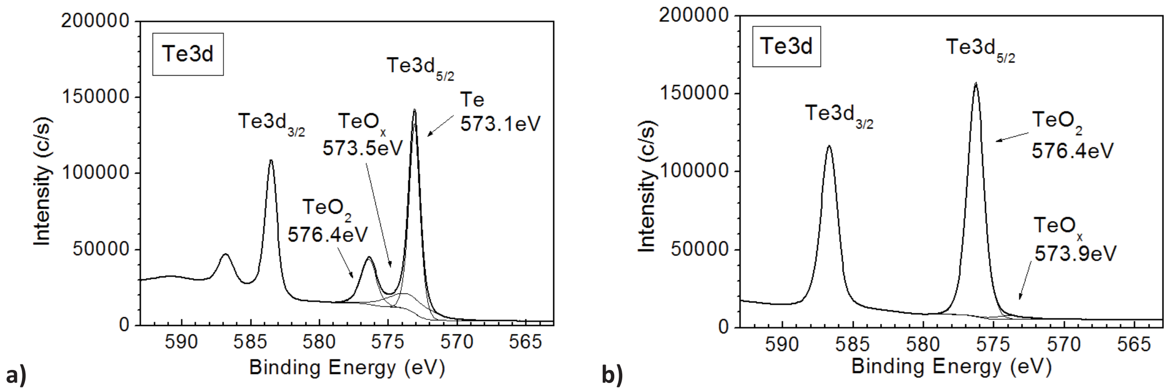

Figure 64: XPS Te*3d* spectra of metallic Te in a) and TeO_2 in b)

The $Cu_{60}Te_{40}$ and $Cu_{60}Te_{40}$ + Ge XPS spectra are displayed in Figure 65 a) the Te$3d_{5/2}$ region, in b) the Cu$2p_{3/2}$ region and in c) the Ge*3p* region. The contributions of the $Cu_{60}Te_{40}$ + Ge layer will be detailed in 5.3.3.

Many contributions are observed in a) for Te$3d_{5/2}$ spectra and some of them have never been reported in particular in the Te region. Thanks to the positions identified with the reference samples, the spectrum can be interpreted. First, in the case of the $Cu_{60}Te_{40}$, three contributions are observed. The first one, positioned at 573.1eV, clearly corresponds to the tellurium metallic Te-Te bonds. The second one at 575.6eV is situated between the Te-Te and TeO_2 binding energies, thus it is supposed to correspond to tellurium sub-oxide. Finally, the third and most important peak is situated at 572.2eV. As it has a lower binding energy than metallic tellurium and as only oxygen and copper are expected to be present in the layer, this peak is attributed to Cu-Te bonds. It is interesting to notice that the second important peak in this spectrum corresponds to oxidized tellurium, which unveils the oxidation of the layer and confirms the interpretations made with the XRD results in 3.3.1, Figure 31. Compared to the $Cu_{60}Te_{40}$ sample, the $Cu_{60}Te_{40}$ + Ge Te$3d_{5/2}$ envelope seems to be shifted toward higher binding energies. In order to have a realistic interpretation of the fit, the positions of the contributions observed in the $Cu_{60}Te_{40}$ are first fixed in the $Cu_{60}Te_{40}$ + Ge spectrum. It appears that to adjust the fit, two new contributions must be added: one at 576.5eV, which corresponds to TeO_2 and another one around 572.7eV. According to the bibliography, this contribution corresponds to Ge-Te bonds [6]. This identification seems coherent because the electronegativity of germanium is lower than that of tellurium but higher than copper. Thus a Ge-Te peak should be positioned between Te-Te and Cu-Te peaks, which seems to confirm the results. Moreover, the shift toward higher binding energies could be explained by the Ge-Te bonds formed, which decrease the number of Cu-Te bonds. Additionally, the oxidized contribution of Te$3d_{5/2}$ changes from TeO_x to TeO_2 with the addition of germanium, together with a peak intensity decrease.

In b), the $Cu_{60}Te_{40}$ Cu$2p_{3/2}$ spectrum presents three peaks, identified thanks to literature [7]: the Cu at 932.6eV, the CuO at 934.1eV and the Cu-Te at 935.2eV. One can remark that the CuO peak intensity is higher than the metallic Cu peak, which means that the copper is oxidized at the surface of $Cu_{60}Te_{40}$ sample. In the case of the $Cu_{60}Te_{40}Ge$ sample the same peaks are recorded, however the CuO peak shows a lower intensity than for the $Cu_{60}Te_{40}$ sample, which indicates a decrease of the Cu oxidation when the germanium is added. Therefore, as both Cu and Te show a decrease of oxidation in the $Cu_{60}Te_{40}$ + Ge sample, it seems that the germanium acts as a passivation element of the CuTe layer against oxidation.

This behavior is confirmed in the last Ge*3d* spectrum in c). Indeed this spectrum presents two contributions, identified thanks to the literature. As the doublet separation of Ge*3d* is only 0.58eV, here the Ge*3d* doublet is represented by one peak. The first peak, with the highest intensity, is situated at 32.5eV and corresponds to GeO_2 [8] and the second one at 30.3eV corresponds to Ge-Te bonds [8]. The high intensity of the GeO_2 contribution seems to confirm the passivation behavior of the germanium supposed above. Indeed we conclude that the germanium forms a GeO_2 layer at the surface of the $Cu_{60}Te_{40}Ge$ alloy, thus protecting the layer from atmosphere.

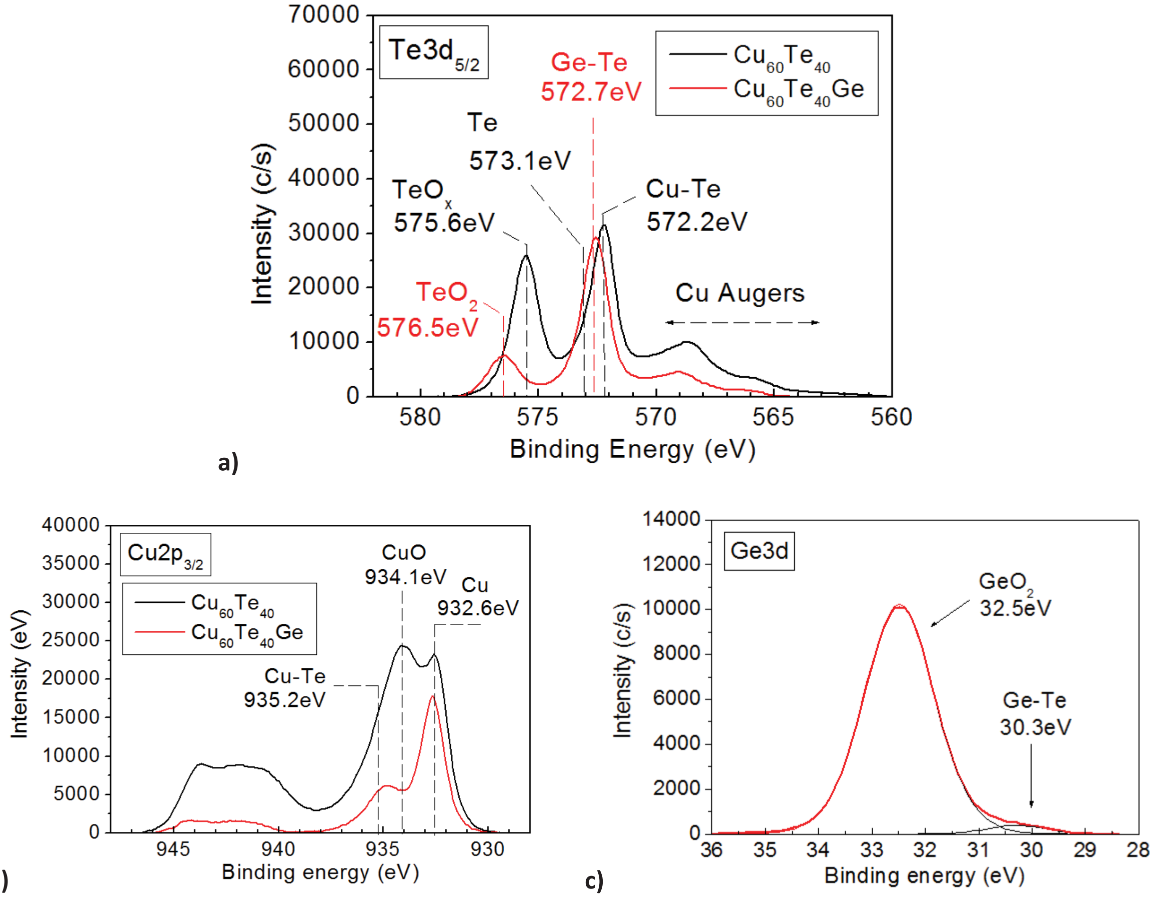

a) b) c)

Figure 65: XPS spectra for $Cu_{60}Te_{40}$ and $Cu_{60}Te_{40}$ + Ge samples, in a) Te*3d*$_{5/2}$, in b) Cu*2p*$_{3/2}$ and in c) Ge*3d*

5.2.5. Conclusion

In conclusion, the material characterizations show that the addition of germanium in CuTe enables its amorphization, prevents the layer from oxidation and forms Ge-Te bonds at the expense of Cu-Te bonds. This was already reported by W. Devulder *et al.* in [9]. In this paper, they studied the influence of germanium addition in Cu-Te films and the impact of this layer when used as ion source layer in an Al_2O_3 CBRAM. The authors observed with germanium, the decrease of the Cu-Te bonds, together with a better stability of the filament, resulting in a better data retention. The improved stability of the filament is explained by the presence of Ge-Te bonds: they reduce the activity of pure tellurium, which is believed to act as copper dissolution element in the ion source layer. Therefore, the copper filament is less able to be re-dissolved in the ion source layer during reset, thus appears more stable.

Moreover, in all the forming studies performed in the previous chapters the germanium was never observed to act during the forming. It never diffuses or changes chemically when applying the electrical field. Thus, we can conclude that germanium does not act during the forming. It is also interesting to notice that other elements can be used instead of germanium to amorphize the CuTe layer as nitrogen, carbon and zirconium. The zirconium study will be presented in 5.4. The other elements were also tested but the results will be not presented here. Even if they all amorphize the $Cu_{60}Te_{40}$ layer, only germanium and zirconium show a memory effect.

5.3. Impact of the copper amount on the cell properties

5.3.1. Introduction

In this part the influence of the CuTe alloy composition on the forming is studied. For this purpose, a $Cu_{60}Te_{40}$ + Ge alloy has been synthesized and analyzed through material characterizations. Then, a comparison through electrical tests will be performed between both $Cu_{60}Te_{40}$ + Ge and $CuTe_2Ge$ stacks.

5.3.2. Samples

As the material characterizations have already been presented in the chapter 3, details on deposition and characterizations parameters are reported in 3.4. For electrical tests the memory stacks are described in Figure 66, with $CuTe_2Ge$ film as reference versus $Cu_{60}Te_{40}$ + Ge film. The electrodes and the dielectric layer are deposited with the same parameters than described in 3.3 for the reference stack. A shadow mask technique is used to realize the devices. The mask is inserted just before the deposition of the ion source layer. Then, the $Cu_{60}Te_{40}$ + Ge ion source layer is deposited by co-sputtering of two targets with an Ar flow set at 40sccm. The first target is a $Cu_{60}Te_{40}$ target, sputtered with a power density of 0.6W/cm^2 and the second target is a pure Ge target, sputtered with a power density of 0.2W/cm^2. The reference $CuTe_2Ge$ layer was achieved using the same parameters than described in 3.3. Note that the bottom electrode is made of tantalum instead of titanium nitride in this study, since it impacts the electrical results.

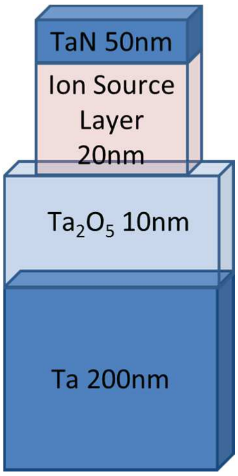

Figure 66: Ta_2O_5-based stack used to compare $CuTe_2Ge$ versus $Cu_{60}Te_{40}Ge$ ion source layers through electrical tests

Finally the electrical tests were achieved on the memory stacks using potential ramps from 0 to 3V for the forming and sets and from 0 to -1.5V for the reset.

5.3.3. Analysis of the $Cu_{60}Te_{40}$+Ge layer

Figure 67 shows the detailed XPS fits: in a) the Te$3d_{5/2}$ region, in b) the Cu$2p_{3/2}$ region and in c) the Ge$3d$ region. As already discuss in 5.2.4, in a) the Te$3d_{5/2}$ region presents four contributions. The TeO_2

is adjusted at 576.5eV, a metal form Te at 573.1eV and two chalcogenides: Ge-Te at 572.7eV and Cu-Te at 572.2eV. In b) the Cu*2p*$_{3/2}$ shows three contributions, with metallic Cu at 932.6eV, CuO at 934.1eV and Cu-Te at 935.2eV. Finally, the Ge*3d* region in c) presents two contributions, the GeO_2 at 32.5eV and the Ge-Te at 30.3eV. Taking into account the composition of the layer measured by RBS in 5.2.2, the Ge-Te has a too low intensity compared to the Ge-Te contribution observed in Te*3d*$_{5/2}$. This is explained by the presence of a GeO_2 top layer, which is formed at the surface of the sample due to air-break. In Ge*3d*, the Ge-Te contribution is hidden by the GeO_2 top layer. This GeO_2 layer also limits the penetration of oxygen in the volume of the layer, which explains why in Te*3d*$_{5/2}$ and Cu*2p*$_{3/2}$ only a very low level of oxide is observed.

Hence, these XPS results show that the alloy is mainly composed of copper metal embedded in a GeTe/CuTe matrix, with GeO_2 top layer which limits oxygen penetration in volume.

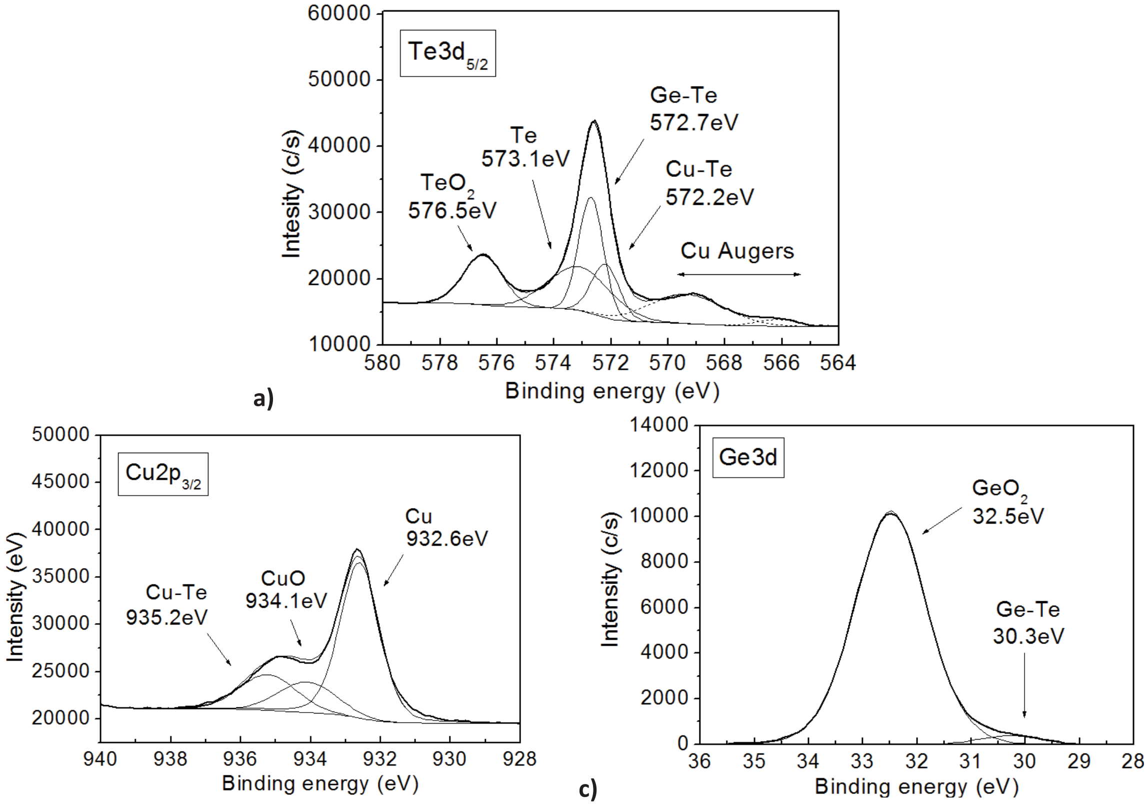

a)

b)

c)

Figure 67: XPS results for the $Cu_{60}Te_{40}Ge$ sample, with in a) the Te*3d*$_{5/2}$ region, in b) the Cu*2p*$_{3/2}$ region and in c) the Ge*3d* region.

5.3.4. Impact of the copper amount on the electrical response

The Figure 68 shows in a) an I-V curve obtained with the Ta_2O_5 10nm/$Cu_{60}Te_{40}Ge$ cell and in b) an I-V curve obtained with the reference $CuTe_2Ge$ cell, both on pure tantalum bottom electrode. The $Cu_{60}Te_{40}Ge$ stack has been cycled three times. During the first cycle the forming is observed at 1.8V, which enables the current to reach the compliance value at $7x10^{-3}$A. Then the voltage is reversed, the reset is observed at -1.4V and next the other cycles are achieved.

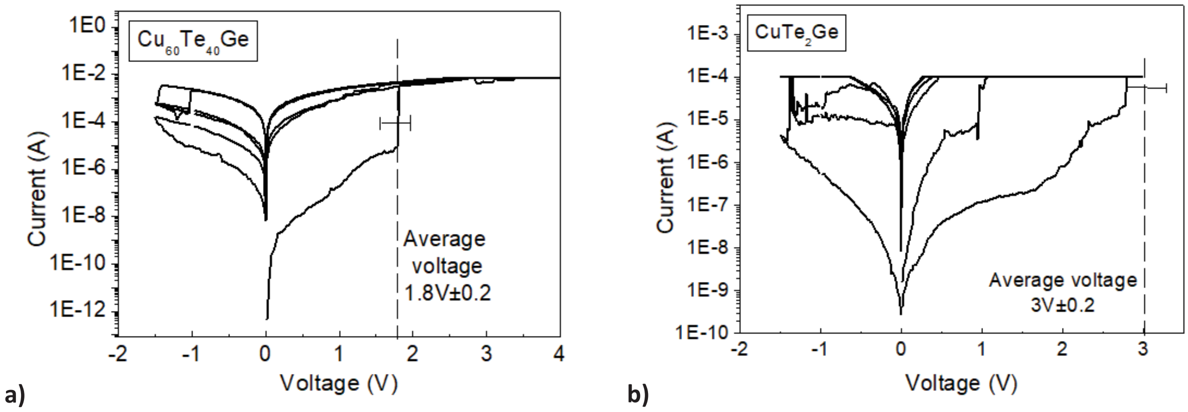

Figure 68: a) Typical I-V curve for the $Cu_{60}Te_{40}Ge$-based stack and b) for the $CuTe_2Ge$-based stack

The average forming voltage of 1.8V±0.2 is extracted from several cells on the same wafer. In comparison, in b) the average forming voltage of the $CuTe_2Ge$ is measured at 3.0V±0.2. Here we notice that the forming voltage of the $CuTe_2Ge$ reference cell is higher than the reference stack reported in 3.4, observed at 1.7V±0.2 on TiN bottom electrode (see Figure 38). To explain such difference, one can assume different effects due to the bottom electrode chemistry. First, TiN as bottom electrode may trap much more oxygen (such as solubilized oxygen in TiN volume) than pure Ta electrode, which in turn also impacts the memory forming. Second, the use of a Ta bottom electrode induces uncertainties on the deposited thickness of Ta_2O_5 since the Ta substrate is oxidized during Ta_2O_5 reactive sputtering deposition due to the oxidizing atmosphere. These assumptions would require a full study on the bottom electrode and its effect on the electrical results in the integrated cell. Nevertheless, in the current paragraph, we try to compare the reference stack and the $Cu_{60}Te_{40}Ge$ stack using the same bottom electrode, here in tantalum.

The electrical results show that the $Cu_{60}Te_{40}Ge$-stack has a clear lower forming voltage than the $CuTe_2Ge$ reference stack on the same bottom electrode. In 3.2 literature survey proposed that the forming voltage should increase when increasing the copper composition of a CuTe alloy [1], which is not the case in our memory.

An explanation could be the possible presence of copper in the Ta_2O_5 before the forming. Presence of copper could decrease the breakdown voltage of Ta_2O_5 as already observed in literature with other dielectrics ([10]-[12]). This initial amount of copper could be induced either by sputtering impacts during PVD, where the copper could be physically implanted in the dielectric, or through diffusion of copper in Ta_2O_5. However, literature survey indicates that Ta_2O_5 is a pretty good barrier against copper diffusion ([13]-[15]). In particular, it is reported that Ta_2O_5 prevents copper diffusion up to 600°C, even at a very thin thickness of 1nm. Whatever the causes of this possible copper presence in the dielectric, it is clear that a higher amount of copper in the ion source layer must conduct to a higher amount of copper in the Ta_2O_5, which in turn reduces the forming voltage.

It is interesting to notice that here the $Cu_{60}Te_{40}Ge$ ion source layer seems similar to a pure copper ion source layer according to XPS results observed in 5.3.3. They shown a high level of Cu-Cu bonds in comparison to Cu-Te and nearly no Cu-O bonds due to Ge passivation effect against oxygen. In 3.3.1 we saw that with a pure copper ion source layer the memory presents a clear forming voltage while reset was impossible. Here, with the addition of an amount of Te lower than in the Te-rich $CuTe_2Ge$, we see that the cell is able to cycle. Therefore, we see here the main role of tellurium, which is to dissolve into the ion source layer the diffused copper presents in the Ta_2O_5, which in turn resets the cell as presented in Figure 69.

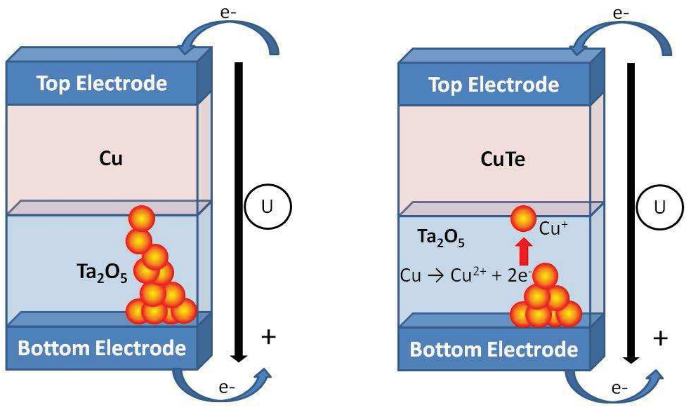

Absence of reset **Reset**

Figure 69: Behaviors observed when reversing the potential with pure Cu ion source layer (left) and CuTe ion source layer (right)

5.3.5. Conclusion

To conclude, XPS results show the $Cu_{60}Te_{40}Ge$ as an alloy mainly composed of copper embedded in a CuTe matrix, with a GeO_2 passivation top layer. Electrical results show a lower forming voltage than the $CuTe_2Ge$ reference with the same bottom tantalum electrode, contrary to the observations made in literature. This could be due to an initial amount of copper in the Ta_2O_5, through either a deposition artifact or the diffusion of copper. However, the second assumption is weak since the barrier properties of Ta_2O_5 are high and no anneal was achieved on the cells. Then, it is observed that the main role of tellurium takes place during the reset, where it helps to dissolve into the ion source layer the diffused copper presents in the Ta_2O_5, which in turns resets the cell. As the role of tellurium is a bit clearer, we will go back to the role of oxygen as we did in chapter 4, but through scavenger alloying.

5.4. Impact of oxygen scavenger alloying

5.4.1. Introduction

In the chapter 4, the importance of oxygen in CBRAM forming mechanisms have been discussed, with its role as a counter charge. Therefore here the impact of an oxygen scavenger, directly inserted in the ion source layer, is studied. An oxygen scavenger is a chemical element able to reduce oxygen in an oxide layer thanks to its reactivity toward oxygen. The reduction can be direct through intimate contact or “remotely” with interlayers.

For this purpose, we decided to replace the germanium by an element that is more reactive toward oxygen. The germanium is chosen to be replaced because the studies on the forming mechanisms that are performed in 3.5.1, 4.2.3 and 4.3.2 seem to show that germanium does not act during the forming. The main role of germanium is to amorphize the CuTe alloy (see 5.2). Therefore, the metal chosen must amorphizes the CuTe alloy and be active toward Ta-O bonds in Ta_2O_5.

The chosen metal for replacing germanium is zirconium. The oxygen scavenging phenomenon is expected as observed in the Ellingham diagram displayed in Figure 70. It presents the standard Gibbs free energy of some oxides as function of the temperature. It is possible to see that the zirconium has a lower standard Gibbs free energy than tantalum, while germanium is higher than tantalum. It means that the germanium cannot reduce the tantalum oxide, but that zirconium should lead to ZrO_2 formation through the following reaction (15):

$$\frac{2}{5}\mathrm{Ta_2O_5} + \mathrm{Zr} \rightarrow \frac{4}{5}\mathrm{Ta} + \mathrm{ZrO_2} \tag{15}$$

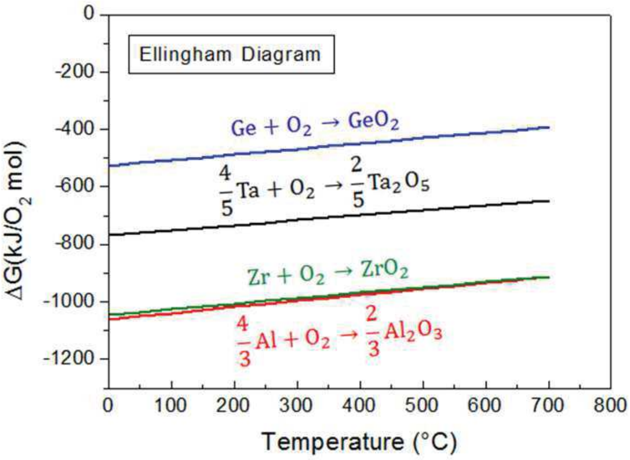

Figure 70: Ellingham diagram

For this purpose in this part a $Cu_{60}Te_{40}Zr$ alloy is going to be developed, which will be first studied through material characterizations. Then, the layer will be used as ion source layer on Ta_2O_5 dielectric and electrical tests will be performed.

5.4.2. Analysis of $Cu_{60}Te_{40}Zr$

5.4.2.1. Samples

Two samples are studied in this section: a $Cu_{60}Te_{40}Zr$ layer compared to a reference $Cu_{60}Te_{40}$ layer. The $Cu_{60}Te_{40}Zr$ layer is deposited by co-sputtering of the $Cu_{60}Te_{40}$ target together with a Zr target with 40sccm Ar flow. The power density used for the $Cu_{60}Te_{40}$ target is 0.6W/cm^2 while for zirconium several compositions are tested by varying powers: 13W, 15W, 30W, 60W and 150W, corresponding respectively to power densities of 0.17, 0.19, 0.38, 0.76 and 1.91W/cm^2. The reference $Cu_{60}Te_{40}$ sample is deposited with an Ar flow at 40sccm and a power density of 0.6W/cm^2. The thicknesses of the layers deposited are 20nm for XPS and XRD samples and 40nm for the RBS samples.

RBS is performed on $Cu_{60}Te_{40}Zr$ 15W and 60W. Then, XRD measurements are performed in order to see the amorphization of the CuTe alloy with zirconium progressive incorporation. $Cu_{60}Te_{40}Zr$ samples with Zr 13W, 15W, 30W and 150W are analyzed together with the reference $Cu_{60}Te_{40}$ sample. Finally XPS analyses are achieved on $Cu_{60}Te_{40}Zr$ 13W sample, in order to identify the bonds between copper, tellurium and zirconium.

5.4.2.2. Composition extracted by RBS

RBS results are presented in Table 5. It appears that for both $Cu_{60}Te_{40}Zr$ 15W and 60W, the Cu/Te ratio is lower than 1.5 as expected for a stoichiometric $Cu_{60}Te_{40}$. However, in this work the layers will be still called “$Cu_{60}Te_{40}Zr$” for a clearer notation. Additionally, the $Cu_{60}Te_{40}Zr$ 15W layer presents a content of 5.1 atomic% of zirconium and the $Cu_{60}Te_{40}Zr$ 60W a content of 19.9 atomic%.

	Cu (atomic %)	Te (atomic %)	Zr (atomic %)	Cu/Te ratio
$Cu_{60}Te_{40}$ Zr 15W	53.4±2	41.5±2	5.1±0.5	1.3
$Cu_{60}Te_{40}$ Zr 60W	43.8±2	36.3±2	19.9±1	1.2

Table 5: RBS compositions of $Cu_{60}Te_{40}$Zr with Zr target sets at 15W and 60W

5.4.2.3. Effect of Zr alloying on $Cu_{60}Te_{40}$ crystallinity

The XRD results are displayed in Figure 71. In a) the XRD spectrum obtained on $Cu_{60}Te_{40}$ reference sample is presented. In b) the results for the several compositions of $Cu_{60}Te_{40}$Zr alloys are shown. The reference sample in a) presents two peaks positioned at 24.8° and 45.6°. According to literature they should correspond to hexagonal Cu_2Te (0,0,6) and (3,0,6) [18], respectively. Therefore, as expected as deposited $Cu_{60}Te_{40}$ is crystalline. In b) $Cu_{60}Te_{40}$ co-sputtered with zirconium is amorphous with no peaks even for the lowest amount of zirconium. Therefore, zirconium inhibits the crystallization of the CuTe alloy. For XPS measurements the $Cu_{60}Te_{40}$Zr 13W will be studied as it is amorphous and has the lowest amount of zirconium.

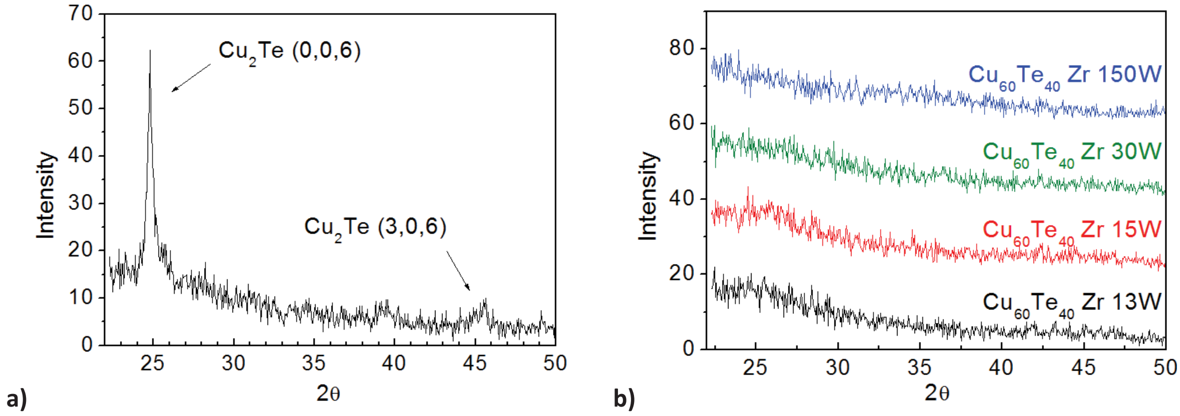

Figure 71: XRD spectra of a) $Cu_{60}Te_{40}$ sample and b) $Cu_{60}Te_{40}$Zr alloys with several Zr compositions

5.4.2.4. Chemical environments of Zr in $Cu_{60}Te_{40}$Zr

XPS results for the $Cu_{60}Te_{40}$Zr 13W sample are displayed in Figure 72, with Te$3d_{5/2}$ spectrum in a), Cu$2p_{3/2}$ spectrum in b) and Zr3d spectrum in c).

The Te$3d_{5/2}$ spectrum is quite complex, with many contributions added to reach a correct fit. Thanks to the fits already discussed in 5.2.4 we easily identify in the $Cu_{60}Te_{40}$Zr sample the tellurium sub-oxide TeO_x at 575.5eV, the metallic tellurium Te at 573.1eV and the Cu-Te bonds at 572.2eV. Then, to complete the fit a contribution must be added at 570.8eV. However, in literature no contributions are identified for tellurium at such a position. Nevertheless, in the $Cu_{60}Te_{40}$Zr layer the elements which can enable a contribution at a lower binding energy than metallic tellurium are copper or zirconium. As Cu-Te bonds are already identified in the fit, it seems that this last contribution at 570.8eV could be attributed to Zr-Te bonds.

Then in b) the Cu$2p_{3/2}$ presents three contributions. They are the same than identified in 5.3.3 and in 5.2.4, with metallic Cu at 932.5eV, CuO at 934.1eV and Cu-Te bonds at 935.1eV.

Finally in c), the Zr$3d$ doublet shows two contributions. Zr$3d_{5/2}$ spin-orbit components are positioned at 179.8eV and 181.5eV, which gives the Zr$3d_{3/2}$ peaks at respectively 182.2eV and 183.9eV as the doublet separation Δ_{Zr3d}=2.4eV [19]. These positions could correspond to zirconium sub-oxides as they are positioned between metallic Zr (178.7eV [20]) and ZrO_2 (182.8eV [20]). Table 6 summaries literature binding energy values of zirconium oxidation states obtained by XPS.

	Zr^0	**Zr^{+1}**	**Zr^{+2}**	**Zr^{+3}**	**Zr^{+4}**
Binding energy (eV)	178.7	179.8	180.7	181.7	182.8

Table 6: Values from literature for the different Zr oxidation states [20]

Thanks to these values, it appears that in our spectrum the first peak at 179.8eV could correspond to Zr^{+1} and the second peak at 181.5eV to Zr^{+3}. In literature it is observed that with a zirconium oxide the sub-oxides contributions have an intensity which decreases when the oxidation state increases. In our case the peak at 181.5eV has the highest intensity, which does not correspond to literature values which may correspond to the presence of Zr-Te bonds. The low oxide peaks in Te$3d_{5/2}$ and Cu$2p_{3/2}$ compared to the CuTe sample observed in 5.2.4, show that as for germanium the zirconium protects the ion source layer from oxidation.

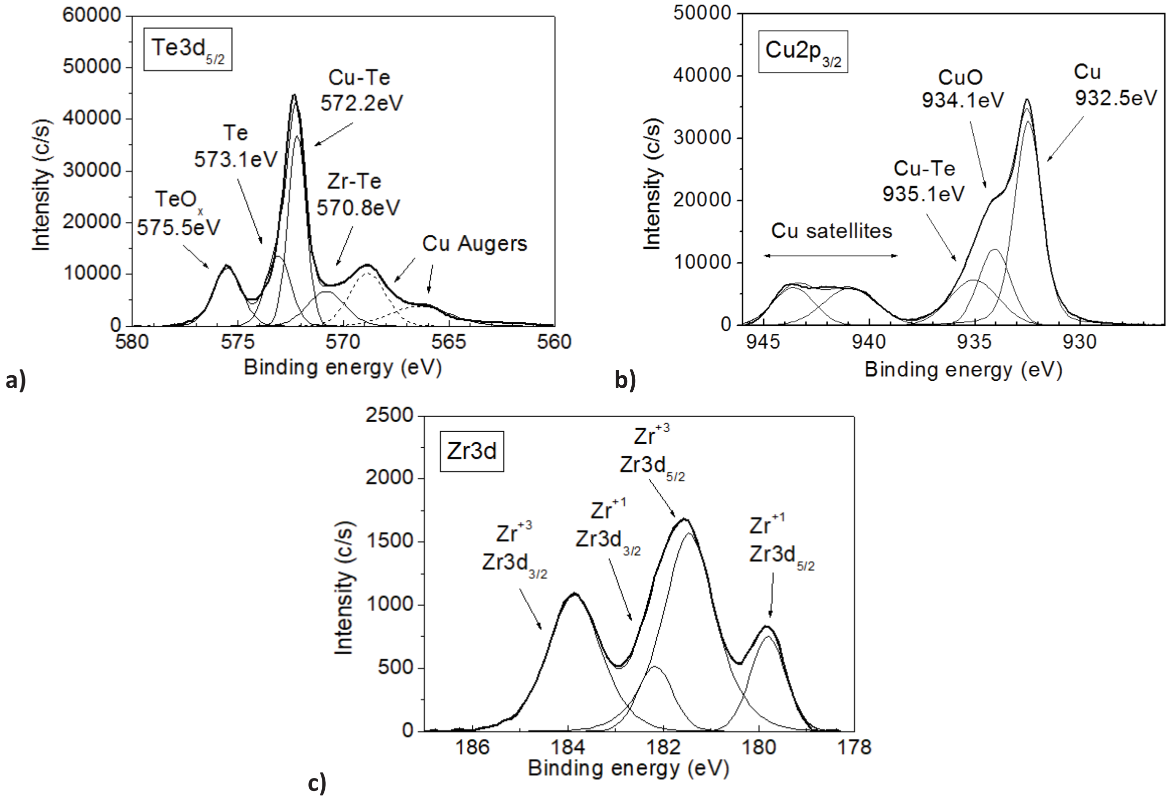

Figure 72: XPS spectra for $Cu_{60}Te_{40}Zr$ 13W sample: a) Te$3d_{5/2}$ b) Cu$2p_{3/2}$ c) Zr$3d$.

To conclude these analyses, the addition of zirconium in $Cu_{60}Te_{40}$ alloy amorphizes and protects the layer against oxidation as with germanium.

5.4.3. Electrical results: a short circuited cell

5.4.3.1. Samples

The $Cu_{60}Te_{40}$ with Zr 15W was inserted as ion source layer in a Ta 200nm/Ta_2O_5 10nm/$Cu_{60}Te_{40}$Zr 15W 20nm/TaN 50nm memory stack. The stack was deposited on a 200mm silicon wafer, with the ion source layer and the top electrode deposited through a shadow mask in order to form the devices (see 2.1.2). The $Cu_{60}Te_{40}$Zr 15W was deposited with an Ar flow of 40sccm by co-sputtering of a $Cu_{60}Te_{40}$ target with a power density of 0.6 W/cm^2, together with a Zr target adjusted at 15W (corresponding to 0.19W/cm^2 power density). The other layers were deposited with the same parameters than in 5.3.2. After the deposition, electrical tests were performed with cycles between -1.5V and 3V and a compliance current of 7x10^{-3}A.

5.4.3.2. Results and discussion

The Figure 73 shows the current-voltage curve obtained with the $Cu_{60}Te_{40}$Zr memory stack. When applying the voltage up to 3V, the current slowly increases until a sudden rise to 7x10^{-3}A, observed at 2.1V. This sudden increase corresponds to the forming. Then, the voltage is decreased until -1.5V and increased back to 0V. It appears that no reset is observed. Moreover, during the second cycle the curve does not present any set or reset and the current directly reaches the compliance. It means that the memory is formed but cannot be erased, thus the memory is short-circuited and no other filament formation can be observed. Other devices were also tested with other parameters, such as a lower compliance or a higher negative voltage. However, no behavior of cycling was observed in all the tested devices. The different tests only indicate an average forming voltage of 2.1V±0.3.

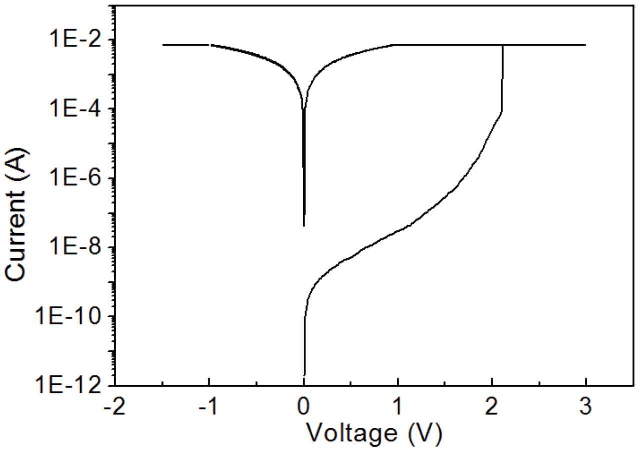

Figure 73: Typical I-V curve obtained with the $Cu_{60}Te_{40}$Zr 15W stack

This forming voltage value is higher than the reported value of 1.7V±0.2 with $Cu_{60}Te_{40}$Ge ion source layer studied in 5.3. It is important to notice that the error bars overlap, meaning that the increase of forming voltage observed between the $Cu_{60}Te_{40}$Zr and $Cu_{60}Te_{40}$Ge samples must be taken with caution as it could be only due to the error. Nevertheless, it seems that the substitution of germanium by zirconium impacts the forming voltage toward a higher forming voltage and an absence of reset for zirconium.

An explanation to the absence of reset could be the reduction of the tantalum oxide by the zirconium. Indeed, as already explain in 5.4.1, due to its very low standard Gibbs free energy the zirconium could have reduced the tantalum oxide. This local deoxidation brings oxygen vacancies in the layer, which could lead to a decrease of the dielectric breakdown voltage. In this case, the forming observed at 2.1V±0.3 corresponds to the breakdown of the Ta_2O_5 layer and the memory cannot cycle anymore.

Another explanation could be linked to the potential assisted diffusion of zirconium in its cationic form (Zr^+ or Zr^{4+}) during forming. Actually, it was seen in previous studies in 5.2 that germanium does not act during forming (no diffusions or chemical changes observed after forming). As the behavior of zirconium is not clear, one cannot exclude any movement of zirconium in sub-layers. This is also supported by the fact that we recorded Zr-Te bonds in the ion source layer. We could expect some Zr ions formation if we imagine that such bonds are prompt to induce ionic elements through the equilibrium $Zr^{4+} + 2Te^{2-}$.

To support these assumptions, we decided to replace the Ta_2O_5 by Al_2O_3. As observed in the Ellingham diagram in Figure 70, it has a lower standard Gibbs free energy than Ta_2O_5 but can still be reduced by zirconium, according to the reaction (16). This point is going to be studied in 5.4.4.

$$\mathrm{Zr} + \frac{2}{3}\mathrm{Al_2O_3} \rightarrow \mathrm{ZrO_2} + \frac{4}{3}\mathrm{Al} \qquad (16)$$

Moreover, further studies with ZrTe in the ion source layer will be started to observe the behavior of zirconium during forming (see later in part 5.5).

5.4.4. Dielectric modification: Al_2O_3

In this part the Ta_2O_5 is replaced by Al_2O_3 and the stack becomes Ta 200nm/Al_2O_3 5nm/$Cu_{60}Te_{40}$Zr15W 20nm/TaN 50nm. The Al_2O_3 layer was deposited by RF sputtering of an Al_2O_3 target with an Ar flow of 40sccm and a power density of 2.5W/cm^2. 5nm thickness was chosen for the dielectric instead of 10nm in the case of Ta_2O_5, to compensate the resistivity increase due to the high band gap of Al_2O_3. Indeed, Figure 33 shows the relationship between the band gap and the dielectric constant for some oxides [21]. The Al_2O_3 shows a higher band gap than Ta_2O_5, which means it is more resistive than Ta_2O_5 for the same deposited thickness. Thus, in order to match the stacks, 5nm of alumina was deposited.

Finally, electrical tests were performed on the stack with a compliance current set at 7x10^{-3}A and cells were cycled between 2.5V and -2V.

The Figure 74 shows the I-V curve obtained with Al_2O_3/$Cu_{60}Te_{40}$Zr cell. During the forming cycle, when increasing the voltage, an abrupt increase of the current appears at 0.5V which is attributed to the forming. This forming voltage is in the average values obtained on other devices with this stack at 0.7V±0.3. Then the current stabilized at the compliance current (here 7mA). Additionally, when one reverses the potential, a reset behavior with a variation of the current is observed, followed by a set in the next cycle. Hence, this behavior supports the fact that Ta_2O_5 could have been severely reduced with the previous $Cu_{60}Te_{40}$Zr ion source layer (see Figure 73), due to the strong chemical activity of Zr regarding tantalum pentoxide.

Finally, we must say a word on the barrier properties of alumina versus tantalum pentoxide. In fact, if diffusion of copper in Al_2O_3 is less effective than in Ta_2O_5, copper could be constrained mainly in the filament region instead of being spread into the dielectric, which could improve cell cycling.

To summarize, Al_2O_3 has a standard Gibbs free energy low enough to be less reduced by zirconium and could have better barrier properties against copper diffusion than Ta_2O_5, which opens a R_{ON}/R_{OFF}

contrast required to the cell operation. For the next studies with zirconium, Al_2O_3 will be used as dielectric.

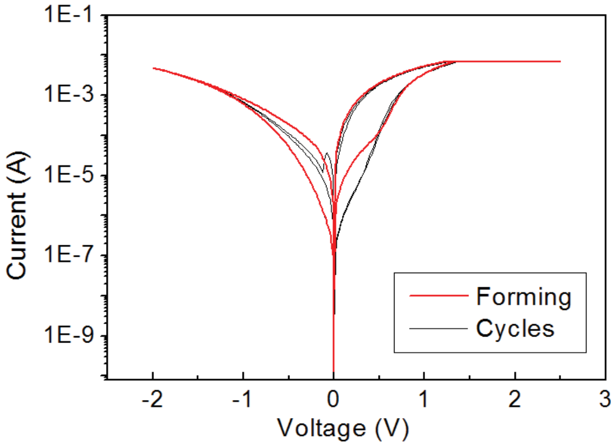

Figure 74: Typical I-V curve of the $Al_2O_3/Cu_{60}Te_{40}Zr$-based stack

5.4.5. Conclusion

We observed in the previous chapters that oxygen element has a fundamental role on the memory operation. We studied in this part the substitution of germanium by zirconium in the ion source layer in order to evaluate the influence of strong oxygen scavenger on the electro-forming. For this purpose a $Cu_{60}Te_{40}Zr$ layer was studied, first through material characterizations and then through electrical tests in a Ta_2O_5-based memory stack, with $Cu_{60}Te_{40}Zr$ layer as ion source layer. XRD and RBS analyses show that less than 5 atomic% of zirconium is enough to amorphize the CuTe alloy, which is a pre-requisite path toward integration. Moreover, XPS spectra show the presence of Zr-O bonds and less Cu-O and Te-O bonds than in CuTe layer, indicating that Zr protects the ion source layer against oxidation. Even if the electrical tests present a forming, the cell cannot be cycled.

Several assumptions were proposed to explain the absence of a reset. Among them, one is about the eventual reduction of Ta_2O_5 by Zr. The zirconium could reduce the tantalum pentoxide, leading to a large oxygen vacancies path where copper diffuses. A large copper filament is consequently formed and is too thick to be dissolved in the ion source layer when reversing the applied potential. To confirm this assumption, we switch from Ta_2O_5 to Al_2O_3, as the latter has a lower standard Gibbs free energy and is thus expected to be less reactive to zirconium. It appears that effectively with alumina as dielectric, the cells with $Cu_{60}Te_{40}Zr$ were able to cycle. Therefore, it is decided to use Al_2O_3 as dielectric in the further studies when zirconium is alloyed in the ion source layer.

Moreover, it is possible that zirconium has a role during the forming in its ionic form. Indeed, if germanium was not observed to diffuse or be chemically active in $CuTe_2Ge$ ion source layer, maybe zirconium behaves differently in $Cu_{60}Te_{40}Zr$. In particular, we observed the presence of Zr-Te bonds which could promote a solubilized form of Zr^{4+} through potential assisted splitting of $Zr^{+}Te^{-}$ bonds. In the next part, we will try to isolate the case of Zr and try to assess its role through the study of a ZrTe ion source layer, without copper.

5.5. Copper-free ion source layer

In this part, the role of zirconium in the forming will be evaluated through the study of a cell with a ZrTe ion source layer on alumina. The obtained stack will be studied before and after forming by standard XPS, HAXPES and ToF-SIMS, in order to observe the applied voltage effect on the bonding environments and the diffusions of species.

5.5.1. Samples

The studied stack is composed of Ta 200nm/Al_2O_3 5nm/ZrTe 15nm/TaN 5nm and is deposited on a 200mm silicon substrate. The Ta and TaN electrodes were deposited with the same parameters than in 3.3. The Al_2O_3 was deposited by RF-sputtering of an Al_2O_3 target, with an Ar flow of 40sccm and a power density of 2.5W/cm^2. Then, ion source layer and top electrode were deposited through a shadow mask in order to realize the devices. The ZrTe layer was deposited by co-sputtering of Zr and Te targets. For this purpose, an Ar flow of 40sccm was used and pulverizations were achieved at 0.7W/cm^2 and 0.9V/cm^2 for tellurium and zirconium, respectively. The ZrTe layer was also deposited alone on a 200mm silicon wafer in order to be studied by RBS and XPS.

Finally, the memory stack was studied before and after forming by HAXPES and ToF-SIMS. For this purpose two devices were used. One is called OFF, which is at pristine state, and the other one is called ON and is formed thanks to a ramp voltage from 0 to 3.5V and a compliance current of 50mA.

First HAXPES measurements were performed at Spring8 synchrotron. Then, a second study with new samples but with the same stack was performed at ESRF synchrotron. The parameters used for both HAXPES are described in 2.2.2(ii). As ESRF HAXPES has a lower binding energy resolution than Spring8, leading to more noisy results. However, similar shifts are observed with both synchrotrons. As Spring8 and ESRF results present the same behaviors, here we are going to present only the Spring8 results. The measurement spot was centered on and out of the top electrode and Al*1s* region was extracted in order to observe the impact of the ion source layer on the dielectric. Finally after HAXPES, the ToF-SIMS analyses were performed, on both Spring8 and ESRF samples. For this purpose a sputter gun with 500eV Cs^+ was used, with an analysis gun with Bi^{3+} ions at 25keV and a detection of positive ions in MCs^+ mode. Here only ToF-SIMS spectra of the zirconium, tellurium and tantalum are presented as their behaviors have been observed in both Spring8 and ESRF samples, which confirm the observations made. The aluminum, nitrogen and oxygen were also measured but the ToF-SIMS results of Spring8 and ESRF samples do not show the same behaviors, for this purpose we prefer to not take them into account.

5.5.2. Characterization of the ZrTe as-deposited layer

20nm ZrTe film was deposited on silicon substrate and compositions were extracted by RBS. The obtained results are summarized in Table 7. It is possible to see that in the ZrTe layer there is 60.5 atomic% of tellurium and 39.5 atomic% of zirconium, thus a Te/Zr ratio of 1.5. Therefore this ZrTe layer is tellurium-rich.

	Te (atomic%)	**Zr (atomic%)**	**Te/Zr**
Deposited ZrTe	60.5	39.5	1.5

Table 7: RBS results for the ZrTe layer

Then, in Figure 75 the XPS results are displayed with the Te$3d_{5/2}$ region in a) and the Zr$3d$ region in b). The Te$3d_{5/2}$ region shows four contributions, which are easily identified thanks to the Te and TeO_2 reference samples already studied by XPS in 5.2.4 and the $Cu_{60}Te_{40}Zr$ sample studied in 5.4.2.4 Te metal is detected with a clear peak at 573.1eV. Then, TeO_x at 575.0eV and TeO_2 at 576.4eV are also identified. A last weak contribution is situated at 571.5eV and remains unclear. As it is situated at a lower binding energy and as only Zr, O and Te are present in the stack, we think that this contribution could correspond to Zr-Te bonds. However, its position is different from the 570.8eV identified as Zr-Te in the $Cu_{60}Te_{40}Zr$ sample and its intensity is very low. In the Zr$3d$ region only one contribution is observed with a peak at 181.8eV for Zr$3d_{5/2}$ and 184.2eV for Zr$3d_{3/2}$ (this is confirmed by the literature which gives the doublet separation ΔZr$3d$=2.4eV [19]). As discuss for the $Cu_{60}Te_{40}Zr$ sample, this doublet could correspond to Zr^{+3} oxide.

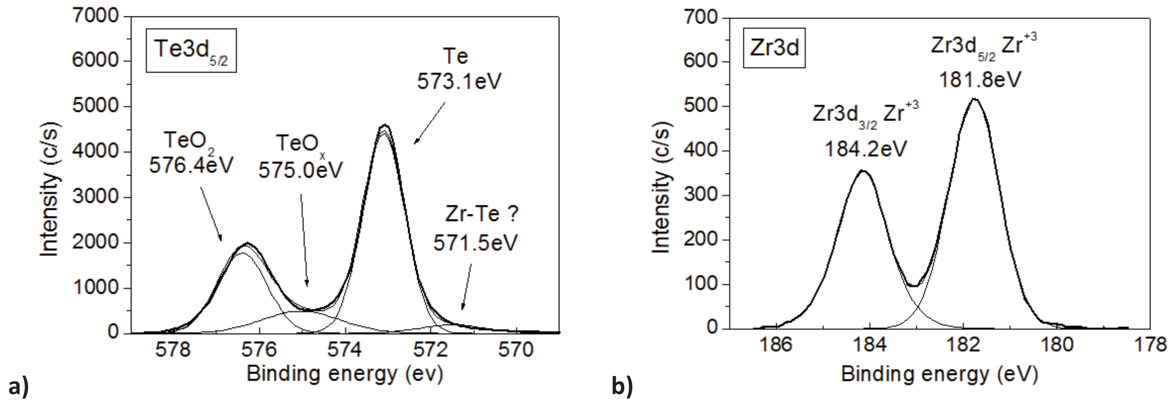

Figure 75: XPS results for a) Te$3d_{5/2}$ region and b) Zr$3d$ region

5.5.3. Electrical results

The current-voltage curve obtained during the ramp voltage is displayed in Figure 76. The voltage was increased from 0 to 3.5V. Until 1V the current increases, followed by a small current variation. After the current increase until around 3.4V where a sudden rise of current is observed. It corresponds to the filament formation and then the current attains the compliance at 50mA. Compared to $Cu_{60}Te_{40}Ge$ or even $Cu_{60}Te_{40}Zr$, one notices the high forming voltage recorded with this copper free ion source layer. It appears that copper helps to reduce the required voltage to form the cell, which seems to be a common pattern with copper alloyed ion source layers.

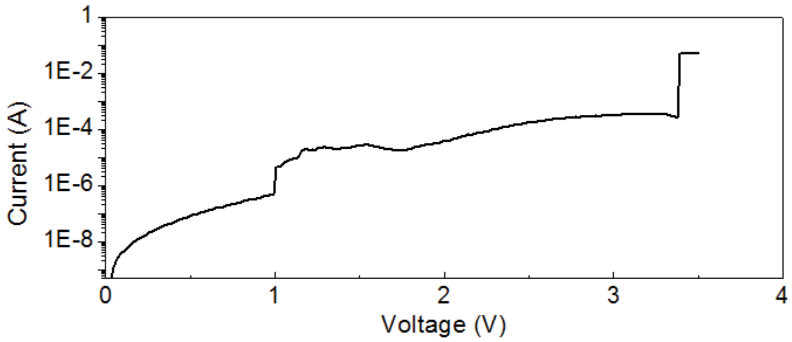

Figure 76: I-V curve obtained during the forming of the ON sample

5.5.4. In depth analysis of the cell with HAXPES

HAXPES Al*1s* spectra at OFF state are taken in two points on the sample, described in Figure 77: One in the device (called “OFF In”) and another one out of the device (called “OFF Out”). The results are presented in Figure 78. In a) the comparison between the Al*1s* in the device at OFF state and out of the device is presented and in b) the OFF and ON spectra are compared.

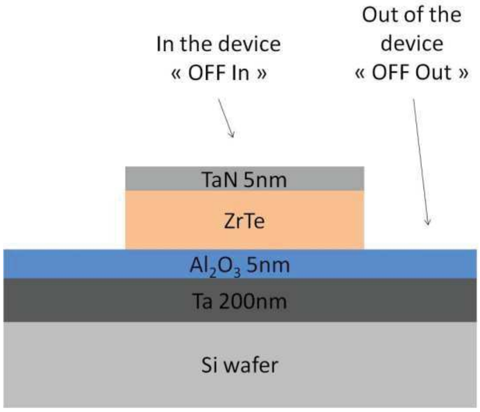

Figure 77: OFF In and OFF Out description

In Figure 78 a) for the OFF out spectrum two contributions are observed. The main contribution is positioned at 1562.3eV and is identified as Al_2O_3 thanks to the literature. Indeed in literature the Al*1s* metallic Al is identified at only 1559.8eV [22]. Moreover, the chemical shift between Al and Al_2O_3 is known to be 3.0eV [23] for Al*1s*, thus giving an Al_2O_3 positioned at 1562.8eV, which is quite close to our peak value. The second contribution, which has a very small intensity compared to the Al_2O_3, is positioned at 1560.8eV, thus it is situated between the Al_2O_3 contribution and a theoretical metallic Al contribution. For this purpose, we supposed that this contribution is sub-oxidized aluminum oxide, called here AlO_x.

Compared to the “OFF out” spectrum, the “OFF in” spectrum shows a clear peak shifted toward the lower binding energies. Indeed in the “OFF in” spectrum the contribution of Al_2O_3 intensity has decreased whereas the contribution AlO_x intensity has increased. This corresponds to the reduction of Al_2O_3, which is due to the deposition of the ion source layer and confirms the scavenger effect of the zirconium (see 5.4.4).

In b) the “OFF in” spectrum and the ON spectrum are presented. The contributions are the same as observed previously: Al_2O_3 and AlO_x. However, the ON sample spectrum is weakly shifted, toward lower binding energies. In the fit this corresponds to an increase of the AlO_x intensity. Thus a small reduction of the dielectric is observed after the forming.

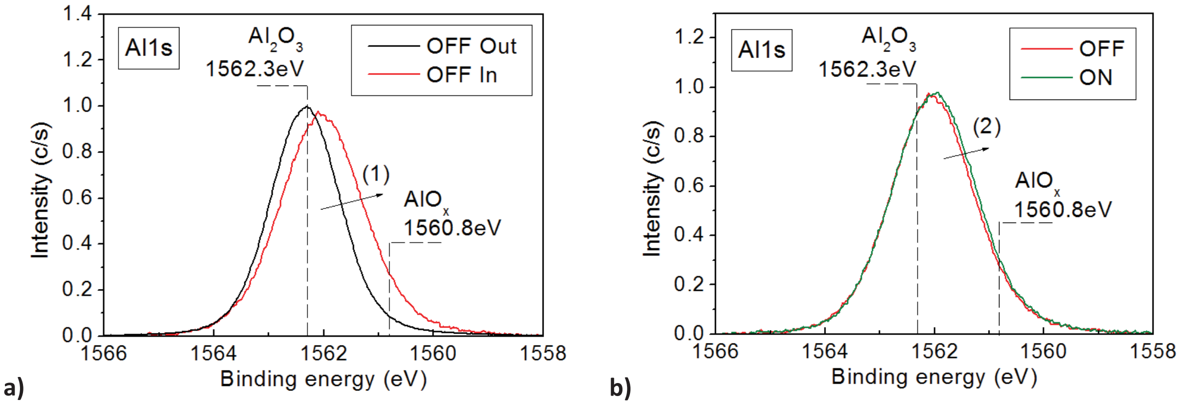

Figure 78: HAXPES Al*1s* results with in a) "OFF Out" and "OFF In" spectra and in b) the OFF and ON spectra

In Figure 79, Zr*3p*$_{3/2}$ spectra are presented at OFF and ON state. Two contributions are observed. The first at 330.0eV is identified as Zr [24], the second, positioned at 332.2eV, could correspond to zirconium oxide. In literature the different oxidation states contributions are identified in Zr*3d*$_{5/2}$ region with a zirconium oxide sample, giving chemical shifts presented in Table 8 [20]. Thus, their positions in Zr*3p*$_{3/2}$ are calculated in Table 8 from the experimental position of metallic Zr, 330.0eV. From these calculated positions we are able to identify the second contribution at 332.2eV in the spectrum as Zr^{+2}. However, Zr^{+1} contribution does not appear in the fit. This is partly due to the noticeable width of the envelope, where many contributions could be convoluted. Thus the contribution is called ZrO_x. Presence of oxidized zirconium may correspond to reduced alumina as seen in Figure 78, but large part of this oxygen may also come from the surface via atmospheric oxygen diffusion through the thin 5nm TaN top electrode. Additionally, we will see in Figure 81 that the Te*3p*$_{3/2}$ region presents Zr-Te bonds, thus it means that the large envelope in the Zr*3p*$_{3/2}$ spectrum may also contain a Zr-Te peak.

	Zr^{+1}	Zr^{+2}	Zr^{+3}	Zr^{+4}
Chemical shifts (eV) from [20]	1.1	2	3	4.1
Calculated Zr*3p*$_{3/2}$ position (eV)	331.1	332	333	334.1

Table 8: Calculated HAXPES position for the different zirconium oxidation states

Between OFF and ON state a small increase of the ZrO_x contribution intensity, at high binding energy, is observed. Moreover, it is not clear if Zr-Te bonds are present or not, therefore this increase could correspond to an oxidation of zirconium or to an increase of Zr-Te bonds number. This point will be discussed later with the study of the Te*3p*$_{3/2}$ region.

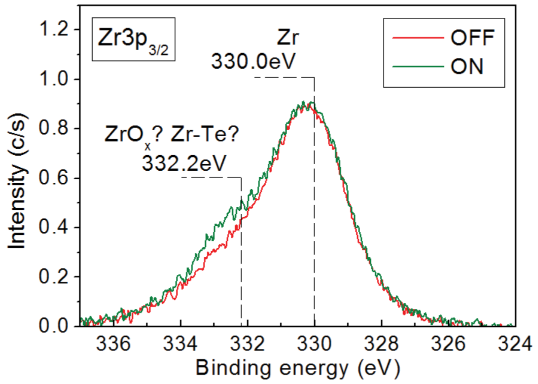

Figure 79: HAXPES OFF and ON Zr$3p_{3/2}$ spectra

In Figure 80 the ToF-SIMS results of zirconium are presented at OFF and ON state. First, it is possible to see that zirconium has strongly diffused in Al_2O_3 already at OFF state. Then, when comparing OFF and ON states, very slight shift seems to be present (see arrows (1) and (2)) and could imply a diffusion of Zr toward the bottom electrode. However, such assertion should be taken with precaution as the observed effects are very tiny. This shift of zirconium content toward the bottom electrode is small but also observed elsewhere on the other set of samples prepared for ESRF analysis and not shown here.

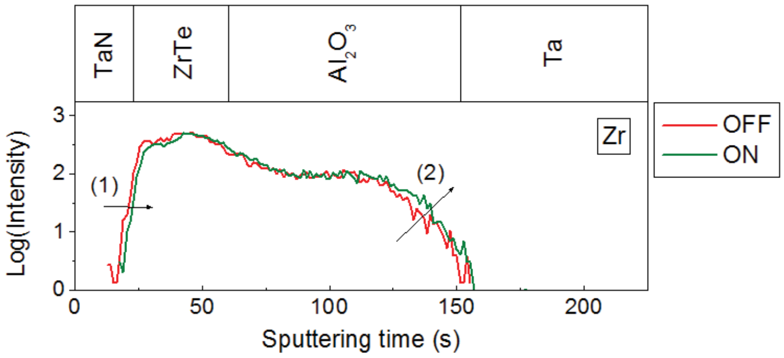

Figure 80: Zirconium ToF-SIMS profiles at OFF and ON states

The Te$3p_{3/2}$ spectra are presented in Figure 81, with the detail of the fit presented with the OFF spectrum in a) and the OFF/ON comparison in b). To ease the fit of the Te$3p_{3/2}$, which is very complex, a metallic Te peak is first fixed at 819.8eV, as reported in the literature [25]. Then, to complete the fit, three other contributions must be added. The first one is positioned at 822.7eV. As the chemical shift between Te and TeO_2 is 3.3eV (calculated from Te$3d$ XPS reference spectrum in 5.2.4), it means that the TeO_2 peak must appears 823.1eV. Therefore, our peak seems to correspond to sub-oxide TeO_x as its binding energy is between Te and TeO_2. The second peak at 818.4eV can be identified thanks to the Te$3d_{5/2}$ XPS spectrum presented in 5.5.2. Indeed, the calculated chemical shift between Zr-Te and Te is 1.6eV. Here the peak is positioned at 818.4eV, thus giving a chemical shift of 1.4eV. As the chemical shifts are very close and as no other bonds are expected, it seems realistic to say that the second peak corresponds to Zr-Te bonds. Finally, a third peak must be added at 815.4eV. Currently we have not succeeded in identifying this contribution, nevertheless it is required to complete the fit.

In b) the comparison between OFF and ON state shows overlapped spectra. It means that no chemical change appears for the tellurium after the forming. Therefore, it indicates that the increase of intensity observed in the Zr$3p_{3/2}$ spectra corresponds to an increase of ZrO_x.

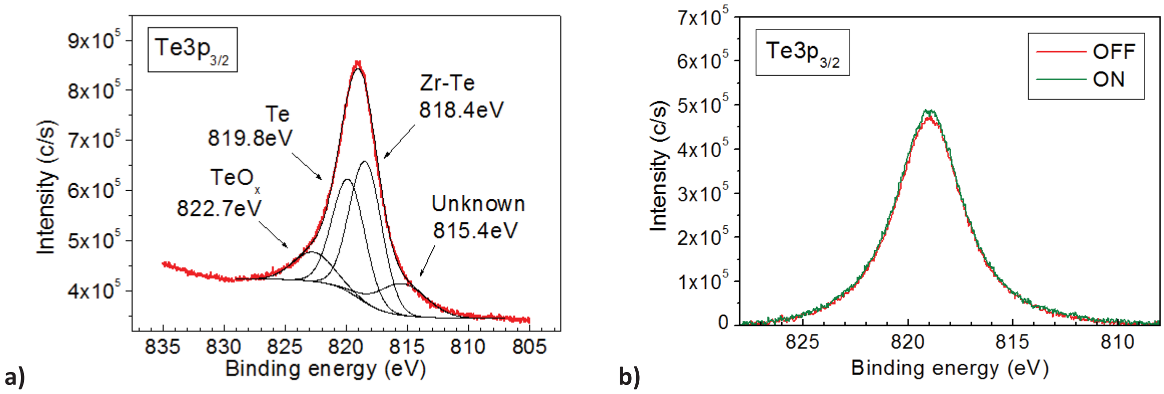

Figure 81: Te$3p_{3/2}$ HAXPES results with in a) the fit presented with the OFF spectrum and in b) the OFF and ON spectra

In Figure 82 the ToF-SIMS profiles of Te at OFF and ON states are presented. Already at OFF state the tellurium appears to be spread in the Al_2O_3. The ON state profile presents an increase of intensity compared to the OFF state profile at around 100s (see arrow 1). Therefore, it seems that the tellurium has diffused in the Al_2O_3 toward the bottom electrode after the forming.

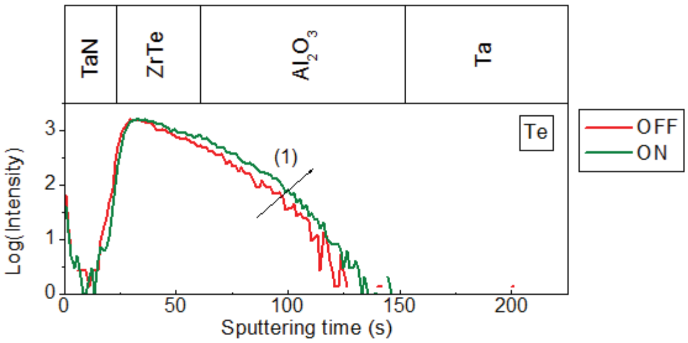

Figure 82: ToF-SIMS profiles of tellurium for OFF and ON samples

5.5.5. Discussion

HAXPES analyses prior forming show that as-deposited zirconium on alumina leads directly to the partial reduction of alumina, as expected from reaction (16). This process induces sub-stoichiometric AlO_x, prompt to act for cell switching. At that point, one must recall that zirconium was sputtered at ambient temperature and no annealing was achieved after deposition. Therefore, this could explain why alumina is not totally reduced here. Also, we see by XPS that Te is nearly not oxidized thanks to the passivation effect against oxygen induced by Zr addition.

Then, in ON state, ToF-SIMS results show that the positions of Zr and Te seem to have changed, with diffusion from the top electrode toward the bottom electrode. However, if the movement of tellurium is clear, in the case of zirconium it is much more difficult to conclude. In HAXPES spectra we observe a slight oxygen reduction of AlO_x induced by the applied potential, together with an increase of ZrO_x contribution. This could correspond to oxygen movement from Al_2O_3 toward the ZrTe after forming, which maybe form a path of vacancies in the dielectric. Thus, such oxygen movement could correspond to an OXRAM-like behavior, with an oxygen vacancies path. However oxygen ToF-SIMS results are not clear enough to confirm this diffusion. Thus it could also correspond to the oxidation of diffused zirconium in the alumina observed by ToF-SIMS.

In literature one paper reports the study of a memory stack with a ZrTe ion source layer [26]. The authors suppose that during forming the oxygen from the dielectric layer diffuses in ionic form to the ion source layer where it oxidizes the zirconium (see Figure 83). Therefore the Zr-Te bonds are broken, enabling the diffusion of tellurium toward the bottom electrode and the formation of a tellurium conductive path. It confirms that in our work the HAXPES results, showing an oxidation of zirconium together with a reduction of alumina, correspond to the diffusion of oxygen toward the top electrode.

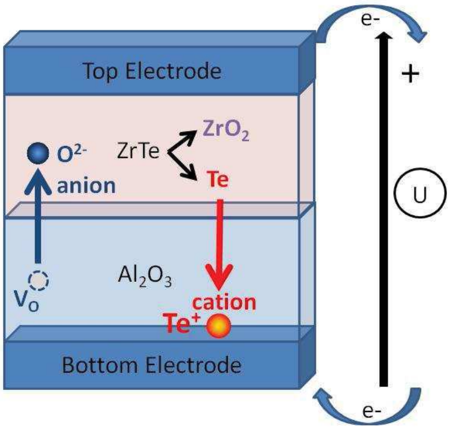

Figure 83: Schematic description of the mechanisms in ZrTe/Al_2O_3 memories according to [26]

In all cases the role of zirconium in this stack is quite clear: it induces a high level of vacancies, forming a dielectric prompt to form an electrical path. Stated differently, through its high oxygen reactivity, zirconium produces a fragile balance of oxygen in the stack, prompt to be drift by an external control such as the applied potential.

The role of tellurium is a bit more subtle. We achieved some ab-initio calculation to estimate the formation enthalpy of ZrO_2 when ZrTe is in contact with Al_2O_3. Figure 84 shows the results for different stabilized phases of the Zr-Te system. It is clear that the formation of zirconium oxide is less favorable when increasing the tellurium content in the alloy. In other words, according to ab-initio calculations tellurium reduces the chemical activity of zirconium toward oxygen.

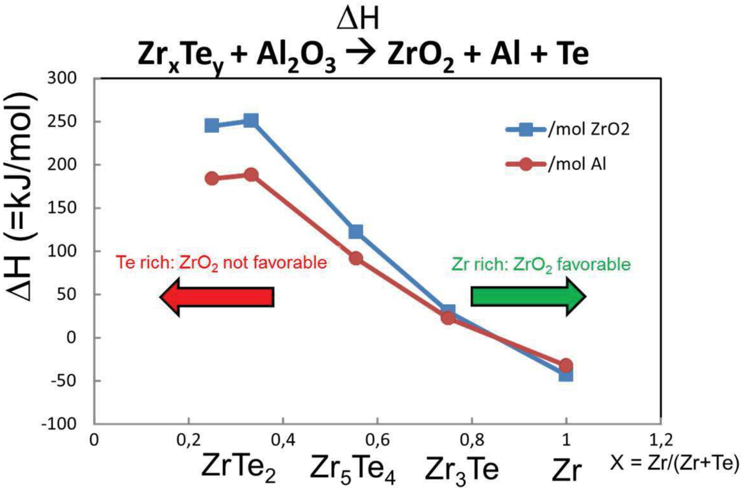

Figure 84: Ab-initio calculated ZrO_2 formation enthalpy versus the Zr content in ZrTe alloy

Therefore, by alloying the right amount of tellurium in the ion source layer it is possible to modulate the reactivity of zirconium toward alumina which in turn leads to an acceptable amount vacancies to induce cell cycling. Stated differently, the oxygen affinity of the ZrTe layer can be adjusted. This is a very powerful method to destabilize a system and reach the right balance.

5.5.6. Conclusions on ZrTe as ion source layer

In this part the impact of a ZrTe ion source layer on the forming is studied. The aim is to have a better understanding of the tellurium and zirconium behaviors during the forming. For this purpose a memory stack with Al_2O_3 as dielectric and ZrTe as ion source layer is studied before and after forming. The stack in-depth analysis shows the direct reduction of Al_2O_3 after ZrTe deposition. This induces a sufficiently high level of vacancies prompt to form a conducting path. The main role of zirconium is to pump oxygen in the Al_2O_3 while the role of tellurium is to modulate the affinity toward oxygen of the ZrTe layer. Tellurium seems also to diffuse toward the bottom electrode, maybe through oxygen vacancies, but its activity on the cell cycling remains unclear.

5.6. Conclusions

In this chapter the impact of the ion source layer on the forming has been studied through the development of new ion source layers. In a first part the influence of the CuTe alloy composition is studied with the comparison of memory stacks containing $Cu_{60}Te_{40}$ + Ge and $CuTe_2Ge$ ion source layer. Then, the impact of an oxygen scavenger metal, inserted in the ion source layer, is studied with a $Cu_{60}Te_{40}Zr$ ion source layer. Finally, the tellurium and zirconium roles in the memory are studied with a ZrTe ion source layer.

The $Cu_{60}Te_{40}$+Ge/Ta_2O_5 memory behaves as a CBRAM, with copper presence in the dielectric. The main role of tellurium is to dissolve diffused copper in the Ta_2O_5 toward the ion source layer which in turns resets the cell. Additionally, the role of germanium is to amorphize the CuTe layer and to protect the film against oxidation.

Then, we studied the substitution of germanium by zirconium in the ion source layer in order to evaluate the influence of strong oxygen scavenger on the forming. First, the analyses shows that the zirconium promotes the amorphization of CuTe and protects the ion source layer against oxidation as observed with germanium. Then, $Cu_{60}Te_{40}$+Zr memories were tested with Ta_2O_5 dielectric and the absence of reset indicates a strong reactivity of zirconium on this dielectric, leading to a short-circuited insulator. To confirm this assumption we replaced the dielectric by Al_2O_3, which is expected to be less reactive than Ta_2O_5 toward zirconium, and we showed that it was possible to cycle the cell.

Finally, we studied copper free ZrTe ion source layer on alumina. The stack in-depth analysis shows the direct reduction of Al_2O_3 after ZrTe deposition. This induces a sufficiently high level of vacancies to easily form a conductive path. We concluded that the main role of zirconium is to pump oxygen in the dielectric, enabling a set, while the role of tellurium is to modulate the affinity toward oxygen of the ZrTe layer. Therefore, the right ZrTe composition enables us to destabilize the system and reach the oxygen balance required to enable a cycling memory.

In summary, we can observe the following same behaviors: when copper is alloyed in the ion source layer the forming voltage is always lower, probably due to the diffusion of copper in the insulator. Then germanium has no electrical role, it only promotes the amorphization of the CuTe alloy and protects the film against oxidation. The zirconium has a similar role in the ion source layer, however it seems to diffuse when applying the potential. Its electrical role is currently not clear. Nevertheless, its chemical role is to reduce the dielectric after deposition in order to create enough oxygen vacancies to enable the switching. Then, the role of tellurium lies on two levels: first it induces the dissolution of the copper filament in the ion source layer during the reset and second it modulates the affinity of zirconium toward oxygen.

A next step could be to study the robustness of the stacks, in particularly the maximum numbers of cycles, the retention properties and the R_{ON}/R_{OFF} variability, which was not the present aim of this work.

5.7. Bibliography

[1] L. Goux, K. Opsomer, R. Degraeve, R. Müller, C. Detavernier, D. J. Wouters, M. Jurczak, L. Altimime and J. A. Kittl, "Influence of the Cu-Te composition and microstructure on the resistive switching of Cu-Te/Al_2O_3/Si cells", Applied Physics Letters, vol. 99, no. 5, p. 053502, 2011.

[2] L. Goux, K. Opsomer, R. Schuitema, R. Degraeve, R. Müller, C. Detavernier, D. J. Wouters, M. Jurczak, L. Altimime, J. A. Kittl, "Self-Limited Filament Formation and Low-Power Resistive Switching in Cu_xTe_{1-x}/Al_2O_3/Si CBRAM Cell", in 2011 3rd IEEE International Memory Workshop (IMW), pp. 1–4, 2011.

[3] J. Yu, B. Liu, T. Zhang, Z. Song, S. Feng, and B. Chen, "Effects of Ge doping on the properties of Sb_2Te_3 phase-change thin films", Applied Surface Science, vol. 253, no. 14, pp. 6125–6129, 2007.

[4] L. van Pieterson, M. H. R. Lankhorst, M. van Schijndel, A. E. T. Kuiper, and J. H. J. Roosen, "Phase-change recording materials with a growth-dominated crystallization mechanism: A materials overview", Journal of Applied Physics, vol. 97, no. 8, p. 083520, 2005.

[5] M. K. Bahl, R. L. Watson, and K. J. Irgolic, "X-ray photoemission studies of tellurium and some of its compounds", The Journal of Chemical Physics, vol. 66, no. 12, p. 5526, 1977.

[6] R. B. Shalvoy, G. B. Fisher, and P. J. Stiles, "Bond ionicity and structural stability of some average-valence-five materials studied by x-ray photoemission", Physical Review B, vol. 15, no. 4, p. 1680, 1977.

[7] F. M. Capece, V. Di Castro, C. Furlani, G. Mattogno, C. Fragale, M. Gargano, and M. Rossi, "'Copper chromite' catalysts: XPS structure elucidation and correlation with catalytic activity", Journal of Electron Spectroscopy and Related Phenomena, vol. 27, pp. 119–128, 1982.

[8] G. Hollinger, P. Kumurdjian, J. M. Mackowski, P. Pertosa, L. Porte, and Tran Minh Duc, "ESCA Study of molecular $GeS_{3-x}Te_xAs_2$ glasses", Journal of Electron Spectroscopy and Related Phenomena, vol. 5, p. 237, 1974.

[9] W. Devulder, K. Opsomer, G. Rampelberg, B. De Schutter, K. Devloo-Casier, M. Jurczak, L. Goux, and C. Detavernier, "Improved thermal stability and retention properties of Cu–Te based CBRAM by Ge alloying", J. Mater. Chem. C, vol. 3, no. 48, pp. 12469–12476, 2015.

[10] J. L. Plawsky, W. N. Gill, and R. S. Achanta, "Modeling time-dependent dielectric breakdown with and without barriers", Journal of Micro/Nanolithography, MEMS, and MOEMS, vol. 9, no. 4, pp. 041104–041104, 2010.

[11] R. Gonella, "Key reliability issues for copper integration in damascene architecture", Microelectronic engineering, vol. 55, no. 1, pp. 245–255, 2001.

[12] F. Chen, O. Bravo, K. Chanda, P. McLaughlin, T. Sullivan, J. Gill, J. Lloyd, R. Kontra, and J. Aitken, "A comprehensive study of low-k SiCOH TDDB phenomena and its reliability lifetime model development", in 2006 44th IEEE International Reliability Physics Symposium Proceedings, pp. 46–53, 2006.

[13] A. L. Salaün, A. Mantoux, E. Blanquet, and E. Djurado, "ESD and ALD Depositions of Ta_2O_5 Thin Films Investigated as Barriers to Copper Diffusion for Advanced Metallization", Journal of The Electrochemical Society, vol. 156, no. 5, p. H311, 2009.

[14] P. Alén, M. Vehkamäki, M. Ritala, and M. Leskelä, "Diffusion Barrier Properties of Atomic Layer Deposited Ultrathin Ta_2O_5 and TiO_2 Films", Journal of The Electrochemical Society, vol. 153, no. 4, p. G304, 2006.

[15] A. Lintanf-Salaün, A. Mantoux, E. Djurado, and E. Blanquet, "Atomic layer deposition of tantalum oxide thin films for their use as diffusion barriers in microelectronic devices", Microelectronic Engineering, vol. 87, no. 3, pp. 373–378, 2010.

[16] D.-Y. Cho, S. Tappertzhofen, R. Waser, and I. Valov, "Bond nature of active metal ions in SiO_2-based electrochemical metallization memory cells", Nanoscale, vol. 5, no. 5, p. 1781, 2013.

[17] T. Tsuruoka, K. Terabe, T. Hasegawa, I. Valov, R. Waser, and M. Aono, "Effects of Moisture on the Switching Characteristics of Oxide-Based, Gapless-Type Atomic Switches", Advanced Functional Materials, vol. 22, no. 1, pp. 70–77, 2012.

[18] H. Ghoumari-Bouanani, G. Brun, B. Liautard, J. Tedenac, "Equilibres de phases dans le système tellurure de cuivre, tellurure de bismuth", Mater. Res. Bull., 28, 901, 1993.

[19] D. Majumdar and D. Chatterjee, "X-ray photoelectron spectroscopic studies on yttria, zirconia, and yttria-stabilized zirconia", Journal of Applied Physics, vol. 70, no. 2, p. 988, 1991.

[20] I. Bespalov, M. Datler, S. Buhr, W. Drachsel, G. Rupprechter, and Y. Suchorski, "Initial stages of oxide formation on the Zr surface at low oxygen pressure: An in situ FIM and XPS study", Ultramicroscopy, vol. 159, pp. 147–151, 2015.

[21] J. Robertson, "High dielectric constant gate oxides for metal oxide Si transistors", Reports on Progress in Physics, vol. 69, no. 2, pp. 327–396, 2006

[22] K. Yates and R. H. West, "Monochromatized Ag Lα X-rays as a source for higher energy XPS", Surface and interface analysis, vol. 5, no. 4, pp. 133–138, 1983.

[23] T. A. Carlson, W. B. Dress, and G. L. Nyberg, "Study of K-LL auger processes for light elements above Z= 10", Physica Scripta, vol. 16, no. 5–6, p. 211, 1977.

[24] T. A. Sasaki and Y. Baba, "Chemical-state studies of Zr and Nb surfaces exposed to hydrogen ions", Physical Review B, vol. 31, no. 2, p. 791, 1985.

[25]P. R. Sarode, K. J. Rao, M. S. Hegde, and C. N. R. Rao, “Study of $As_2(Se, Te)_3$ glasses by X-ray absorption and photoelectron spectroscopy”, Journal of Physics C: Solid State Physics, vol. 12, no. 19, p. 4119, 1979.

[26]J. R. Jameson and D. Kamalanathan, “Subquantum conductive-bridge memory”, Applied Physics Letters, vol. 108, no. 5, p. 053505, 2016.

Chapter 6: Conclusions

Currently, Flash memory is the common technology for non-volatile memory in electronic devices. However, Flash memories approach their physical limits of downscaling and it is no longer possible to increase the memory integration density. Several solutions are studied. Among them, we studied the resistive memories ReRAM, based on the resistivity change of a dielectric. Hence, ReRAM are the subject of this thesis, especially the Conductive Bridge Random Access Memory (CBRAM) based on the formation and dissolution of a metallic conductive filament and the Oxygen-based Random Access Memories (OXRAM), based on oxygen vacancies filament.

ReRAM switching mechanisms are complex and currently not totally understood. The main phenomena seem to rely on electrochemical effects, with redox reactions and diffusion of ions under electrical field, resulting in the formation of a conductive path. But it is also possible to find several electronic explanations, such as space-charge-limited conduction, charge trapping, etc… These mechanisms occur in both CBRAM and OXRAM. These two types of ReRAM are so similar that it is also possible to find a hybrid CBRAM/OXRAM memory, with conductive metallic filament (CBRAM) and oxygen vacancies filament (OXRAM). This behavior highlights the importance of oxygen in the forming. Indeed, the main mechanisms in CBRAM are considered to be based on electrochemistry, where the oxidation of copper in the ion source layer requires a counter reaction at the bottom electrode and oxygen participates to this counter-reaction. Also, generally in ReRAM an electro-forming, thus a first filament formation at higher voltage than the other sets, is required. This step is currently few studied probably due to its transient nature, however the comprehension of this phenomenon is mandatory if one wants to understand the set/reset states of the memory and try to solve remaining issues of ReRAM such as retention, endurance and variability.

Therefore, the comprehension of the forming mechanisms was the first aim of this thesis. For this purpose, after studying the state of the art of CBRAM forming mechanisms, a Ta 200nm/TiN 5nm/Ta_2O_5 10nm/$CuTe_2Ge$ 20nm/TaN 50nm CBRAM reference stack was chosen in the first chapter according to literature and internal knowledges. Then, this stack was deposited and analyzed by ToF-SIMS and HAXPES before and after forming in order to study the chemical species diffusions induced by the forming. In the next chapters, the reference stack was modified in order to determine the impact of layers on the forming as summarized in Figure 85. In chapter 4, we studied the oxygen behavior, and more precisely the impact of the metal-oxygen bond strength on the forming. The dielectric was first reduced thanks to the insertion of a thin oxygen scavenger such as pure titanium between the ion source layer and the electrolyte. Then, Ta_2O_5 was replaced by a dielectric with a lower Gibbs free energy which induces stronger oxygen-metal bonds in the dielectric. Finally, in chapter 5, to understand the role of each chemical element embedded in the ion source layer, the alloy was modified step by step. In particular, the impact of $Cu_xTe_yGe_z$ composition was studied together with the substitution of germanium by zirconium (another oxygen scavenger) and finally the full substitution of the $Cu_xTe_yGe_z$ by a Zr_xTe_y alloy.

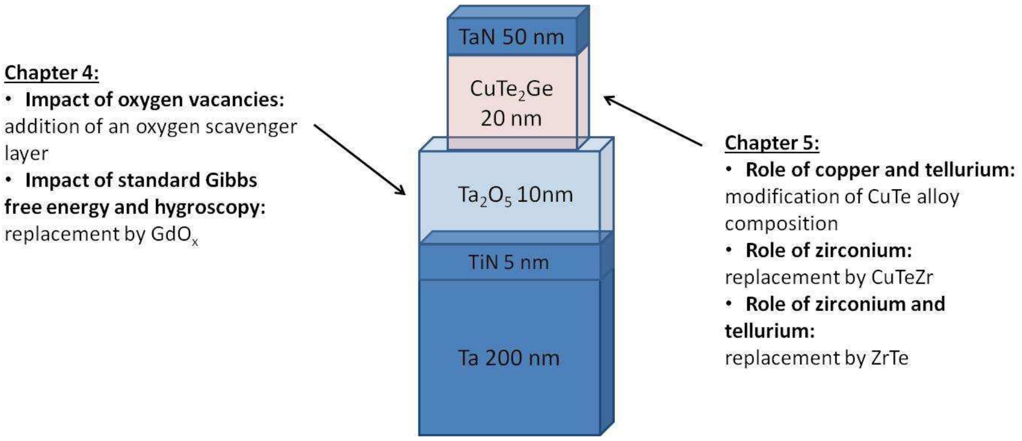

Figure 85: Reference memory stack and resume of the studies conduct in chapters 4 and 5

The chapter 3 results conduct us to suspect an OXRAM behavior in the reference stack. Two explanations were proposed to the presence of an OXRAM forming in a CBRAM memory stack: in first a dielectric breakdown voltage lower than the voltage required to form a metallic filament and in second too high barrier properties against copper diffusion of the dielectric, which prevent copper from diffusing under electrical field. These results show that dielectric properties seem to have an important impact on the type of forming obtained.

The impact of these dielectric properties was studied in more detail in the next chapter, together with the role of oxygen. Analyses show that during the forming, oxygen acts as a counter-charge. Indeed, the electrochemical oxidation reaction of copper at the anode implies a reduction reaction at the cathode with a counter diffusion of negative charges from the cathode to the anode. Here, this reaction and counter diffusion is driven by the oxygen. This oxygen can come from the bottom electrode (partially oxidized during the deposition of the dielectric), which induces a pure CBRAM behavior, or it can come from the dielectric where it forms oxygen vacancies, inducing a hybrid memory behavior.

We conclude that it is possible to promote an OXRAM, CBRAM or hybrid CBRAM/OXRAM memory behavior, by monitoring the quantity of oxygen vacancies present in the dielectric. Properties of the dielectric toward oxygen, such as its metal-oxygen bond strength, can also promote a behavior among others. By using a dielectric with weak oxygen-metal bonds and high barrier properties against copper, an OXRAM behavior can be favored even if the ion source layer contains copper. If this dielectric has oxygen vacancies, which favored the diffusion of copper ions, a hybrid memory can be obtained. Finally, if the dielectric has strong oxygen-metal bonds the CBRAM behavior is promoted.

The roles of copper, tellurium and germanium or zirconium in the forming mechanisms were studied in the last chapter. It appeared that copper could decrease the electro-forming voltage. A suspected explanation is the presence of copper in the dielectric before any application of the electrical ramp. Thus, to reduce the forming voltage, implantation of copper during the dielectric deposition could be a solution. We could also think that using a pure copper ion source layer is a good solution too; however, such memories cannot be erased. Indeed, enabling the reset is the main role of tellurium, which promotes the dissolution of copper back into the ion source layer when reversing the potential. Therefore, a CuTe alloy is required to have a cycling memory and, considering only the forming, a composition such as $Cu_{60}Te_{40}$ is preferred as a copper-rich alloy decreases the electro-forming voltage.

However, we must keep in mind that variability, retention and endurance are probably also impacted by the CuTe alloy composition, thus further studies should be performed to choose the best composition regarding all these electrical parameters.

Moreover, the CuTe alloy must also contain germanium or zirconium. Indeed, the CuTe alloy is rough and unstable in temperature: it is not compatible with integration. But the germanium can enable this integration as it amorphizes the CuTe alloy and protects it against oxidation. Zirconium has the same role. However, contrary to the germanium which seems to be inert regarding the other layers and the electro-forming, the zirconium reacts with the dielectric, forming oxygen vacancies which in turn eases the forming. However, zirconium has a strong activity toward oxygen and could easily reduce the dielectric resulting in a layer with a very low breakdown voltage. Therefore, when writing the memory, an irreversible breakdown can occur before reaching the voltage required to form a conductive path. A solution could be the use of a dielectric with stronger metal-oxygen bonds such as Al_2O_3. Following this path toward improving the memory properties, we observed that tellurium was able to modulate the zirconium reactivity toward oxygen, which was particularly unexpected and gives a powerful solution to modulate the memory properties. Finally, the zirconium may also have diffused after forming. However, the ToF-SIMS profiles of zirconium were not clear and further analyses must be performed to confirm its eventual diffusion.

To summarize, mechanisms which take place during the electro-forming strongly depend on the dielectric and the ion source layer properties, such as breakdown voltage, oxygen affinity, diffusion properties,… In particular, as sketched in Figure 86, we have observed that oxygen has an important role on the forming, most probably due to its capacity to act as a counter charge in the electrochemical mechanisms. Moreover, we saw that a memory behavior, such as CBRAM, OXRAM or hybrid CBRAM/OXRAM, can be promoted among the others by choosing the right dielectric oxide. According to its standard Gibbs free energy (in other words the strength of its oxygen-metal bonds), its hygroscopicity, its barrier properties against copper diffusion and the eventual presence of defects, such as oxygen vacancies, a CBRAM, OXRAM or hybrid forming can be favored. We also saw that copper diffuses in an ionic form during the forming, which enables the formation of a metallic conductive filament and switch the memory. However, copper must be alloyed with tellurium to enable its re-dissolution in the ion source layer when reversing the potential and thus reset the memory. Then, germanium must be added in the CuTe alloy in order to amorphize it, which allows the integration of the layer. Moreover, germanium protects the alloy from oxidation and does not act during the forming. Instead of germanium, zirconium can be used to protect the CuTe alloy from oxidation and for amorphization, however it also reduces the dielectric and thus can ease the forming or even deteriorate the dielectric properties. As tellurium modulates the zirconium reactivity toward the oxide, the ZrTe composition must be chosen carefully to obtain stable cycles.

- **Role of oxygen:**
    - Act as a counter-charge
- **Impact of dielectric properties on forming:**
    - Weak M-O bonds and good copper diffusion barrier properties
      → Promotes OXRAM behavior
    - Addition of oxygen vacancies in the dielectric
      → Promotes hybrid behavior
    - Strong M-O bonds
      → Promotes CBRAM behavior

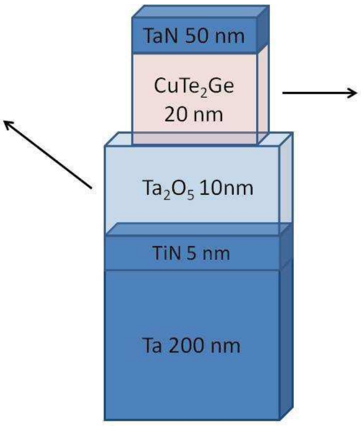

- **Role of copper:**
    - Can diffuse under electrical field and form a conductive filament
    - Reduce the forming voltage
- **Role of tellurium (with copper):**
    - Enable the reset
- **Role of germanium:**
    - Amorphize the CuTe alloy
    - Protect CuTe from oxidation
- **Role of zirconium:**
    - Create oxygen vacancies in the dielectric which ease the electroforming
- **Role of tellurium (with zirconium):**
    - Modulate the impact of zirconium on dielectric

Figure 86: Reference stack and summary of the behaviors observed during the thesis

Finally, this thesis brings answers on the electro-forming mechanisms and explains the role of some elements presents in the stack, however, several points have not been elucidated. Among them the role of zirconium during the forming was not completely resolved. Zirconium diffusion toward the bottom electrode during forming has been suspected, but ToF-SIMS results were not clear as the shift observed was very small. Thus, it was not possible to conclude on the zirconium diffusion and the possibility that it can form a conductive filament. Further analyses may resolve this issue.

Summary

This thesis focuses on the understanding of forming mechanisms in oxide-based conductive bridge memories (CBRAM), based on metallic oxides. For this purpose, we compared the memory stack to an electrochemical cell at nanometer scale and consider that the main mechanisms occurring in the memory rely on electrochemical effects. We started our studies from a reference couple Cu_xTe_y/Oxide, analyzed by HAXPES and ToF-SIMS before and after electro-forming, in order to observe the diffusions and the modifications of the chemical environment occurring during forming. Then, the ion source layer based on Cu_xTe_y alloy and the dielectric (Ta_2O_5, GdO_x or Al_2O_3) were sequentially modified and results of their analyses were compared to the reference stack, in order to understand the role of each layer and chemical elements present in the memory stack.

We evidenced that the properties of the dielectric, such as the strength of its oxygen-metal bonds, its hygroscopicity or the eventual presence of defects such as oxygen vacancies, can promote a given memory behavior from OXRAM to CBRAM or hybrid OXRAM/CBRAM behavior. Moreover, when copper diffuses during the forming, an oxygen counter diffusion also takes place in the dielectric. Also, the presence of tellurium in the ion source layer is required to reset the memory as it enables the dissolution of the copper filament in the ion source layer. We also show that germanium amorphizes the $Cu_xTe_yGe_z$ alloy, thus enables its integration, and protects it from oxidation. Moreover, it is possible to substitute germanium by zirconium resulting in the dielectric reduction, which eases the forming.

Résumé

Cette thèse porte sur la compréhension des mécanismes de forming dans les mémoires à pont conducteur (CBRAM) à base d'oxydes métalliques. Pour cela nous avons admis que l'empilement mémoire est une cellule électrochimique à l'échelle du nanomètre et considéré que les principaux mécanismes de forming sont basés sur des effets électrochimiques. Nous avons débuté nos études à partir d'un couple de référence Cu_xTe_y/Oxyde, analysé par HAXPES et ToF-SIMS avant et après l'electro-forming, dans le but d'observer les diffusions et les modifications de l'environnement chimique durant le forming. Ensuite, la couche fournissant les ions, basée sur un alliage Cu_xTe_y, ainsi que le diélectrique (Ta_2O_5, GdO_x, or Al_2O_3) ont été modifiés étape par étape. Les résultats de leurs analyses ont été comparés avec ceux de l'empilement de référence dans le but de comprendre le rôle de chaque couche et des éléments présents dans l'empilement.

Nous avons vu que les propriétés du diélectrique, telles que la force des liaisons métal-oxygène, l'hygroscopicité, ou l'éventuelle présence de défauts comme les lacunes d'oxygène, peuvent favoriser un comportement mémoire plutôt OXRAM, CBRAM ou hybride OXRAM/CBRAM. De plus, quand le cuivre diffuse durant le forming, une contre diffusion d'oxygène apparaît également dans le diélectrique. Ensuite, la présence de tellure dans la couche fournissant les ions est nécessaire pour permettre l'effacement de la mémoire, car il permet la re-dissolution du filament de cuivre dans la couche fournissant les ions. Nous avons également vu que le germanium amorphise l'alliage de $Cu_xTe_yGe_z$ et donc permet son intégration tout en le protégeant de l'oxydation. De plus, il est possible de remplacer le germanium par du zirconium, réduisant ainsi le diélectrique, ce qui facilite le forming.